eXPRESS Polymer Letters Vol.3, No.9 (2009) 533
Available online at www.expresspolymlett.com
DOI: 10.3144/expresspolymlett.2009.66

Editorial corner – a personal view
Electrical properties of polymer matrix composites: current impact and future trends

G. C. Psarras[*]

Department of Materials Science, University of Patras, Patras 26504, Hellas (Greece)

It is more than 30 years since polymer matrix composites became an important class of engineering materials. The enormous growth of composite technology was based on their superior mechanical performance, light weight, and cost effectiveness. During all these years thorough studies were focused on manufacturing, thermal and mechanical behaviour initially of micro- and recently of nanocomposites. The electrical performance of these systems came into play with a significant delay. Although this delay can be considered as a historical perspective of materials science, the importance of electrical properties is remarkable. Materials can be classified to conductors and dielectrics (insulators and semiconductors) through their conductivity. Our civilization is based on this property, or in other words is based on materials which easily permit the charge carriers migration or to others which prohibit it. It is difficult to imagine personal and professional life without the safe and convenient distribution of electric power.

Since polymer matrix composites are basically electrical insulators, their primary applications result from this property and combine flexibility, ease processing, light weight, shock resistance and environmental stability. Sequentially, the development of conductive systems and moreover the ability to tailor electrical performance by switching from insulating to conductive behaviour opened new fields for technological applications, such as electromagnetic interference shielding, static dissipative plastics, conductive coatings or adhesives and memory switchers. The evolution of polymer nanocomposites started a new round of challenges and possibilities. Electrical behaviour is now governed by a small amount of the nanofiller, while the systems performance is improved. Forthcoming technological changes comprise ‘printing’ circuits in nanoelectronics, transmission lines and energy storing devices. The so called ‘all polymer cable’ consisted by a single polymer system, able to transmit signals and transport power and at the same time protect and insulate the caring line, as well as ‘structural batteries’ where nanoinclusions can act as energy storing devices are not far away. Last but not least, studies on the electrical properties of polymer nanocomposites accumulate valuable knowledge for their structure-properties relationships and related phenomena in nanoscale, opening new opportunities for high-tech applications.

Prof. Dr. Georgios C. Psarras
Member of International Advisory Board

---

[*] Corresponding author, e-mail: G.C.Psarras@upatras.gr

eXPRESS Polymer Letters Vol.3, No.9 (2009) 534–541
Available online at www.expresspolymlett.com
DOI: 10.3144/expresspolymlett.2009.67

Effect of cure cycle on curing process and hardness for epoxy resin

J. Zhang, Y. C. Xu, P. Huang[*]

State Key Laboratory of Materials-Oriented Chemical Engineering, College of Chemistry and Chemical engineering, Nanjing University of Technology, Nanjing - 210009, China

Received 10 April 2009; accepted in revised form 4 June 2009

Abstract. A 3-dimensional finite element model is developed to simulate and analyze the temperature and degree of cure field of epoxy casting part during cure process. The present model based on general finite element software ABAQUS is verified by literature example and experimental data. The numerical results show good agreement with literature example and measured data, and are even more accurate than the simulation of literature. After modeling successfully, the influence of temperature cure cycle ramps have on the temperature and degree of cure gradient is investigated. Moreover, the effect of non-uniform temperature and degree of cure field within epoxy casting part on hardness is demonstrated. The present model provides an accurate and novel method that allows further insight into the process of cure for epoxy resin.

Keywords: *thermosetting resins, epoxy resin, temperature field, degree of cure field, hardness*

1. Introduction

From their discovery by Pierre Castan in 1938 to nowadays, epoxy resins kept on attracting the interests of the industry and academia community. This is because they maintain an excellent balance between various properties such as adhesion properties, electrical insulation properties, humidity resistance, heat resistance, and mechanical properties [1–5].

Determination of cure cycle is one of the important factors for successful fabrication of thick epoxy product with dependable quality and at low cost. The first concern is a non-linear increase in internal temperature induced by the exothermic chemical reaction of epoxy, resulting in temperature overshoot. The second concern relates to the complex temperature and degree of cure gradients that develop during the curing process. Non-uniform curing can lead to incomplete cure or resin degradation and entrapped volatiles or voids, which may ultimately cause a reduction in the overall quality and in service performance of the finished component. Therefore, numerical simulation was attempted to predict temperature rise during cure and the cure simulation was applied to suggest an optimal cure cycle for specific epoxy structures. Although few works focused on the cure simulation of epoxy, there have been many numerical models on the curing of thick thermosetting matrix composites, which can be applied to epoxy either.

Loos and Springer [6] developed a one-dimensional model to simulate the curing process of a flat-plate by solving the governing equation using finite difference method. Lee and coworkers [7–9] studied modeling for cure simulation of thick composite cylinders. They established one-dimensional cure model using the finite difference method. Bogetti and Gillespie [10] also used finite difference method to develop a two-dimensional cure simulation analysis of thick thermosetting compos-

---

[*]Corresponding author, e-mail: phuang@njut.edu.cn

ites. They compared their simulation result with measured data and predicted the temperature and degree of cure distributions within an arbitrary cross-sectional geometry. White and Hahn [11, 12] proposed an optimal temperature cycle that can reduce residual stress during cure of composite structures. Ciriscioli *et al.* [13] developed an algorithm that can minimize void and residual stress inside the composite structure. They measured the temperature, ionic conductivity and compaction in thick graphite/epoxy laminates, and the data were compared to the results calculated by the Loos-Springer CURE model. Twardowski *et al.* [14] compared the experimental temperature profiles of a thick part to the results calculated by a one-dimensional simulation, from which the effect of initial degree of cure was investigated. Hojjati and Hoa [15] established model based on dimensionless parameters for cure of thermosetting composites and predicted the temperature and degree of cure fields of a thick composite. White and Kim [16] proposed the stage cure technique for fabricating thick composites and investigated the effect of stage cure on the mode I interlaminar fracture toughness and shear strength. Yi *et al.* [17] conducted the finite element simulation by assuming thermal properties as a function of temperature and degree of cure. Kim and Lee [18] developed an autoclave cure cycle with cooling and reheating steps for thick thermosetting composite laminates using finite difference analysis. They indicated that the developed cure cycle was effective for reducing temperature overshoot. Blest *et al.* [19] developed a model including resin flow, heat transfer, and the cure of multiplayer thermosetting composite laminates during an autoclave processing, which was validated by comparing the numerical results with the experimental data. Park and Lee [20] developed a two-dimensional cure simulation by finite element method. They calculated through-the-thickness temperature distributions of arbitrary shape composite structures including the mandrel. Oh and Lee [21] studied the cure cycle for glass/epoxy composite laminate by 3-dimensional finite element model based on commercial finite element software ANSYS. An optimized cure cycle with the cooling and reheating steps was developed by minimizing the objective function to reduce the temperature overshoot in the composite. Park *et al.* [22] introduced a three-dimensional finite element model that can be used for cure simulation of composite structures with arbitrary geometry under non-uniform autoclave temperature distribution. Guo *et al.* [23] developed a cure model for thermosetting matrix laminates also based on ANSYS, and proved the conventional cure cycles recommended by prepreg manufacturers for thin laminates should be modified to reduce out-of-plane temperature gradient. Yan [24] developed a two-dimensional finite element model to simulate and analyze the mechanisms pertaining to resin flow, heat transfer, and consolidation of laminates during autoclave processing. Numerical examples, including a comparison of the numerical results with one-dimensional and two-dimensional analytical solutions, were given to validate the finite element formulation. Yan [25] conducted two-dimensional cure simulation of thick thermosetting composites by using a weighted residual method. Numerical examples proved that heat transfer anisotropy has an important effect on the temperature field.

In most of the previous researches, the temperature and degree of cure fields were simulated using one or two dimensional finite difference analysis. Only a few literatures studied the temperature and degree of cure fields by finite element analysis. Although several special-purpose numerical softwares have been developed to study the curing process, few analyses made by general-purpose numerical software [21, 23] were published. Because general-purpose finite element software has well developed pre- and post-processors, researchers can be released from the tedious programming work, and devote their most efforts to the explanation and employment of the simulation results. In the previous studies [5, 21, 23], general finite element software ANSYS were used for predicting curing of resin matrix composites and also for casting resins. But large amount of code was still needed, and programmed by APDL (ANSYS parametric design language). Compared with ANSYS, finite element analytic software ABAQUS has original advantage in dealing with non-linear coupled problems. ABAQUS subroutines in FORTRAN provide a convenient and flexible way for defining degree of cure, cure kinetic equation, and heat outflow process. Moreover, the decoupling of heat conduction equation and cure kinetics equation can be accomplished by ABAQUS automatically. The objective of this study is to gain a fundamental understanding of the cure process unique to thick epoxy casting product. Three-dimensional transient heat transfer finite element model during cure cycle for a thick epoxy cylinder part is established by ABAQUS with its subroutines. The simulation of the cure process accounts for thermal and chemical interactions during cure process. The effect of temperature cycle on the hardness of epoxy is also discussed.

2. Heat conduction analysis and FEM equations

The heat conduction process of resin materials curing is a transient thermal transfer process with nonlinear internal heat generation source, which is from the exothermic enthalpy of resin curing process. According to Fourier's heat conduction equation and energy conservation law, the mathematical model was established as Equation (1):

$$\rho_r V_r H_r \frac{\mathrm{d}\alpha}{\mathrm{d}t} + k_{xx}\frac{\partial^2 T}{\partial x^2} + k_{yy}\frac{\partial^2 T}{\partial y^2} + k_{zz}\frac{\partial^2 T}{\partial z^2} = \\ = \rho C_p \frac{\partial T}{\partial t} \tag{1}$$

where k_{xx}, k_{yy}, k_{zz} are heat transfer coefficients of x, y and z directions, respectively; ρ and C_p are the density and the specific heat of composite material; ρ_r, V_r, α, $\mathrm{d}\alpha/\mathrm{d}t$ are the density, volume fraction, degree of cure, curing rate of resin; H_r is the exothermic enthalpy from resin curing process. The rate of cure could be expressed by the function of degree of cure and time, the formula of which is given through the study of resin curing kinetics (Equation (2)):

$$\frac{\mathrm{d}\alpha}{\mathrm{d}t} = f(\alpha, t) \tag{2}$$

The FEM equations of Equation (1) are well documented and the reader is referred to the text by the Park [20] in this regard. Newton-Raphson iteration with quadratic convergence is employed to solve nonlinear problems in this paper. Using 3-D 8 nodes element DC3D8 in ABAQUS, the degree of freedom of nodes are temperature and degree of cure. The heat outflow process of resin is defined by ABAQUS subroutine HETVAL; degree of cure is defined by ABAQUS subroutine USDFLD; the convection boundary condition is defined by ABAQUS subroutine FILM; temperature boundary condition is defined by ABAQUS subroutine DISP.

3. Experimental

3.1. Materials and sample preparation

The resin used in this paper was obtained by mixing diglycidyl ether of bisphenol-A(DGEBA)-based epoxy (E-51 and E-20 from Wuxi resin factory, the epoxy equivalent of which is 196 and 500 respectively) and cure agent DAMI (long chain flexible aromatic amine, amine equivalent is 517, developed by advanced polymer materials institute, Nanjing University of Technology). The mass ratio of E-51/E-20/DAMI is 1:1:0.922. The mixture was prepared at 130°C with continuous stirring for 2 minutes, and then poured into the cylindrical glass-mould of 12 cm diameter.

3.2. Temperature and mechanical property measurements

The cylindrical glass-mould with the resin sample was put in an oven heated by air with preset temperature profile. The temperature profiles at various locations within the epoxy casting part were measured by thermocouple, and recorded by computer. The hardness values of samples were tested by Shore D-type hardness instrument.

4. Results and discussion

4.1. Literature example model verification

Employing the data from literature [10] for validation, [0/90] glass/polyester laminate is studied and the material property is listed in Table 1. The composite curing kinetic equation was given as Equation (3):

$$\frac{\mathrm{d}\alpha}{\mathrm{d}t} = A\exp\left(-\frac{\Delta E}{RT}\right)\alpha^m (1-\alpha)^n \tag{3}$$

The values of parameters of above equation are listed in Table 2, where A is pre-exponential coefficient, ΔE is activation energy, R is universal gas

Table 1. Thermal properties of glass/polyester composite

ρ [kg·m^{-3}]	C_p [J·kg^{-1}·K^{-1}]	k_{xx} [W·m^{-1}·K^{-1}]	k_{yy}=k_{zz} [W·m^{-1}·K^{-1}]
1890	1260	0.4326	0.2163

Table 2. Cure kinetics parameters for glass/polyester composite

A [min^{-1}]	$3.7\cdot10^{22}$
ΔE [J·mol^{-1}]	$1.674\cdot10^{5}$
m	0.524
n	1.476
R [kJ·kg^{-1}·mol^{-1}·K^{-1}]	8.31434
H_r [J·kg^{-1}]	77 500

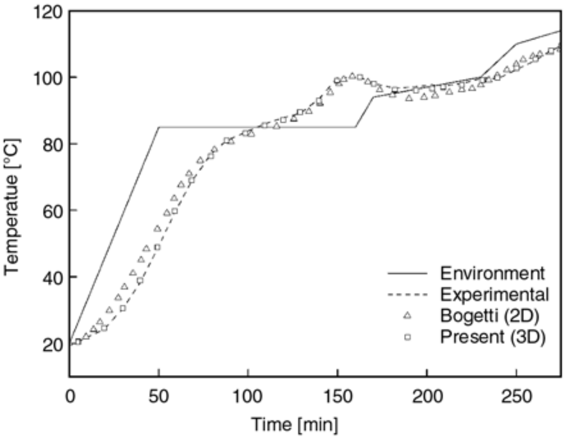

Figure 1. Temperature profiles at the center point of 2.54 cm thickness laminate

constant, T is absolute temperature, m and n are exponents, and H_r is the total heat of reaction.

The dimension of the composite laminate in the example is 15.24×15.24×2.54 cm. The heat convection coefficients h on the top and bottom surfaces are 37.636 and 54.075 W·m^{-2}·K^{-1}, respectively. In addition, insulated boundary conditions were employed on the sides to isolate through the thickness effects. Figure 1 gives the comparison of temperature between calculation results and experimental results from the literature, located in the center of the laminate, from which the validation of the model in this paper is verified. It can be also concluded from Figure 1 that the results from the model in this paper is closer to experimental data than the calculation results from the literature [10].

4.2. Experimental example model verification

The established model for laminate composite is applied to epoxy resin, after that was verified by literature example. The cure kinetic model of the epoxy resin system described in paragraph 3.1 was obtained conducting isothermal scanning tests by Netzsch DSC204 F1. The reaction rate expression for the epoxy resin was given as Equation (4). Figure 2 shows comparison between the heat flow rate measured during the isothermal scanning and those calculated by the cure kinetic model of Equation (4). The developed cure kinetic model agreed well with the experimental results. The thermal properties and cure kinetic parameters of the epoxy resin are presented in Table 3 and Table 4 respectively (Equation (4)).

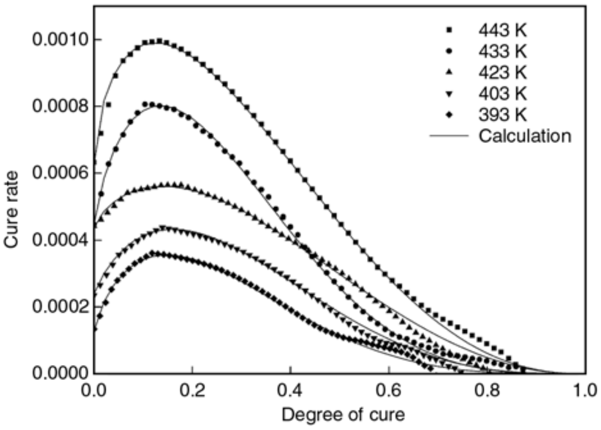

Figure 2. Cure rate versus degree of cure for epoxy

Table 3. Thermal properties of epoxy

ρ [kg·m^{-3}]	C_p [J·kg^{-1}·K^{-1}]	$k_{xx}=k_{yy}=k_{zz}$ [W·m^{-1}·K^{-1}]
1225	967	0.191

Table 4. Cure kinetics parameters for epoxy

A_1 [min^{-1}]	1246.2
A_2 [min^{-1}]	49.26
E_1 [J·mol^{-1}]	38 330
E_2 [J·mol^{-1}]	20 000
m	0.786
n	3.207
R [kJ·kg^{-1}·mol^{-1}·K^{-1}]	8.31434
H_r [J·kg^{-1}]	277 000

$$\frac{d\alpha}{dt} = (k_1 + k_2\alpha^m)(1-\alpha)^n \tag{4}$$

where m and n are exponents, k_1 and k_2 and defined by the Arrhenius rate expressions (Equation (5)):

$$k_1 = A_1 \exp\left(-\frac{\Delta E_1}{RT}\right) \qquad k_2 = A_2 \exp\left(-\frac{\Delta E_2}{RT}\right) \tag{5}$$

where A_1 and A_2 are pre-exponential coefficients, R is universal gas constant, ΔE_1 and ΔE_2 are activation energies, T is absolute temperature. Because the glass mould is very thin, it was assumed that the

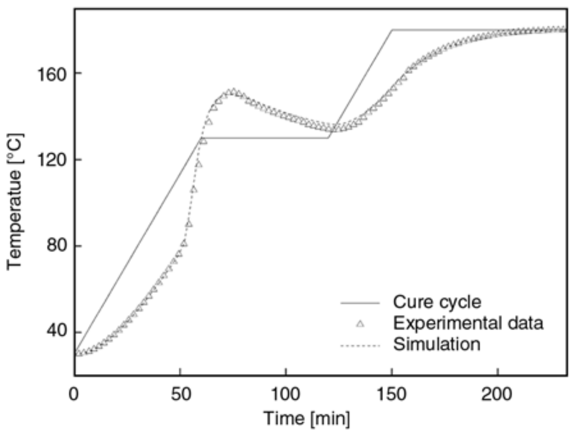

Figure 3. Temperature profile of epoxy cylinder part

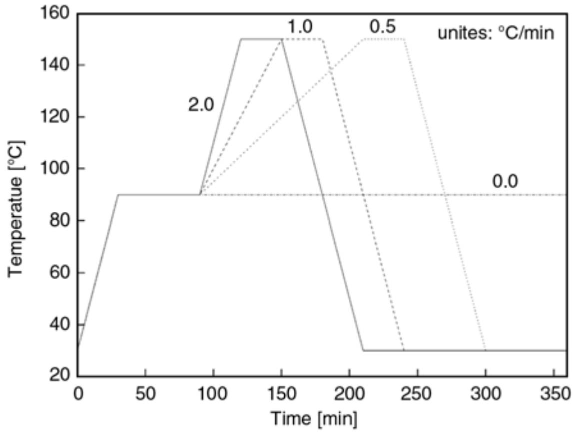

Figure 4. Temperature cure cycle ramps

resin part contacted with exterior environment directly. The epoxy cylinder part with 12 cm diameter and 1.2 cm height was subjected to cure cycle temperature history indicated in Figure 3 with specified $h = 5\ \mathrm{W \cdot m^{-2} \cdot K^{-1}}$. Figure 3 illustrates the comparison of temperature between calculation results and experimental results of the epoxy concerned, located in the center of the cylinder part, from which the validation of the model is verified.

4.3. Cure cycle temperature ramp effects

The cure cycle temperature ramp can strongly influence the temperature and degree of cure gradients that develop during the cure. The effect of the temperature cure cycle ramp on the degree of cure gradients is examined in an epoxy part described above exposed to various cure cycle temperature ramps. The epoxy part with specified temperature and convective boundary conditions ($h = 5\ \mathrm{W \cdot m^{-2} \cdot K^{-1}}$) on all the surfaces is used here respectively. The temperature cure cycle is illustrated in Figure 4. Predicted values of the degree of cure at the center point (point A in Figure 7) minus the degree of cure at the surface point (point F in Figure 7) of the part ($\alpha_c – \alpha_s$) with temperature and convective boundary conditions, are plotted in Figure 5 and Figure 6 as a function of cycle time for the various temperature ramps investigated, respectively.

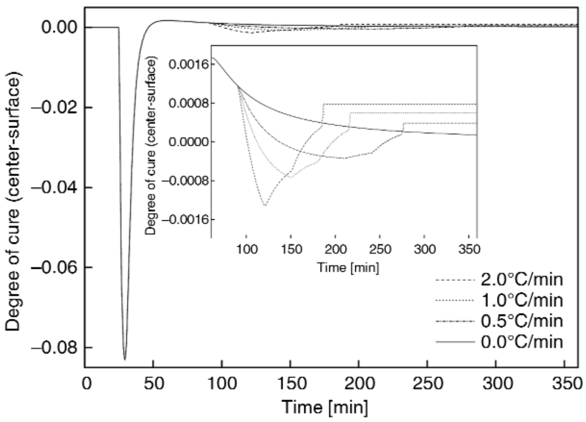

Figure 5. Effect of the temperature ramp on non-uniform curing in epoxy part with temperature boundary condition

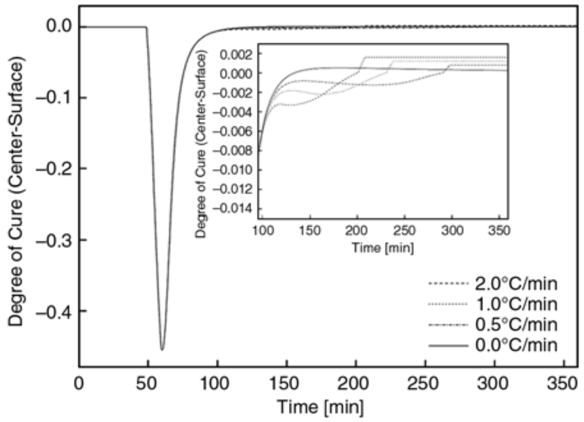

Figure 6. Effect of the temperature ramp on non-uniform curing in epoxy part with convective boundary condition

Both Figure 5 and Figure 6 show a negative peak and the absolute peak value in Figure 6 exceeded in Figure 5. This could be due to that heat transfer by diffusion is low, the surface cure reaction took place earlier than center point, and the heat transfer with temperature boundary condition is more rapid than with convective boundary condition. It is also concluded that with the temperature ramp increasing, the final value of ($\alpha_c – \alpha_s$) rise. Figure 5 and Figure 6 were locally amplified when the curves deviated from each other. It indicated that the value of ($\alpha_c – \alpha_s$) steadily increased from negative value to positive value for convective boundary condition. While for the temperature boundary condition, the value of (α_c–α_s) decreased from positive value to negative value, and then increased to positive value again. Otherwise, with the temperature ramp increasing, the absolute negative peak value rise. Consequently, the surface temperature initiates the cure reaction. The exothermic reaction accelerates the cure and as a result creates non-uniform degree of cure field interior the part. Non-uniform curing potentially entraps voids and volatile byproducts of the cure reaction and enhances warpage and residual stress development. It can be concluded that, the temperature ramp can significantly influence the mechanical properties of epoxy plate.

4.4. Effects on hardness

Normal mechanical testing can not be conducted in single point of epoxy part, while hardness can reflect tensile strength and Young modulus. Therefore, Shore hardness is used here to evaluate the mechanical property of single point of epoxy part. The tested positions are showed in Figure 7, and the hardness of which (average value of 5 times test) is listed in Table 5. Samples for measurement are the epoxy casting part described above cured at the temperature cycle illustrated in Figure 8, with convective boundary conditions ($h = 5\ \mathrm{W{\cdot}m^{-2}{\cdot}K^{-1}}$) on all the surfaces. It was assumed that epoxy resin with higher degree of cure could have higher hardness, but the data listed in Table 5 does not obey this simple rule. Consequently, the mechanical property is not only related to the degree of cure but to the thermal history during cure process. Figure 8 illustrates the thermal history for each point. Without considering the postcure process, the value of temperature peak decreased for point A to point F, while point D has the highest Shore hardness. Released heat resulting from exothermic curing reaction is slow to dissipate by conduction inside epoxy part and may potentially raise local temperature to levels risking material degradation or carbonization, which leads to the decline of hardness. On the other hand, because of the non-uniform temperature field interior epoxy part there is relatively low local temperature inside the epoxy part. When local temperature is excessive low, epoxy resin can not cure completely. Low crosslink density decreases the hardness either. It is essential for epoxy resin casting part that designs a proper temperature cycle neither causes temperature overshoot nor resulting in incomplete cure.

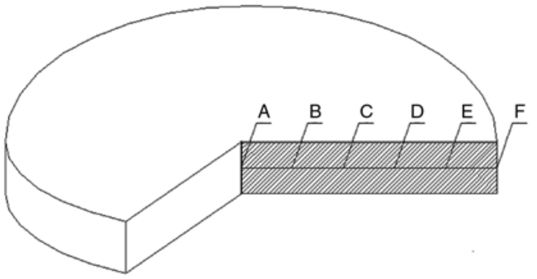

Figure 7. Hardness measurement points of epoxy part

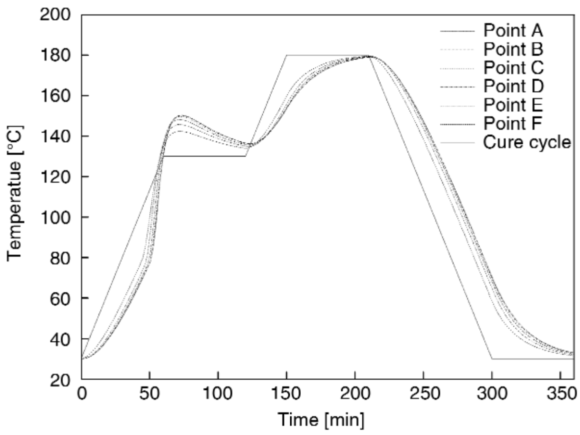

Figure 8. Temperature profiles of epoxy part

5. Conclusions

In this paper, a 3-dimensional finite element model based on general finite element software ABAQUS was developed to study the temperature and degree of cure distribution in epoxy casting part during cure process. The present model is validated by example from literature and experimental data. The predicted results show good agreement with literature example and measured data, and are even more accurate than the simulation of literature. By applying present model, the influence of temperature cure cycle ramps have on the temperature and

Table 5. Final degree of cure and hardness of epoxy part

Position	Point A	Point B	Point C	Point D	Point E	Point F
Final degree of cure [10^{-3}]	926.115	926.104	926.091	926.040	925.874	925.346
Shore hardness	76	76	82	90	80	74

degree of cure gradient is investigated. Moreover, the effect of non-uniform temperature and degree of cure field within epoxy casting part on hardness is demonstrated. The non-linear internal heat source and heat transfer process causes non-uniform temperature and degree of cure field internal epoxy part. By comparing the calculated temperature profile and degree of cure with Shore hardness of a series of internal locations, it indicates that hardness depends not only on the degree of cure but also on the thermal history during cure process. This work, therefore, represents an accurate and novel method that allows further insight into the process of cure for epoxy resin, which can improve mechanical property and in-service performance of the finished component by reducing warpage and residual stress during the cure process.

References

[1] Perrin F-X., Nguyen T. M. H., Vernet J-L.: Kinetic analysis of isothermal and nonisothermal epoxy-amine cures by model-free isoconversional methods. Macromolecular Chemistry and Physics, **208**, 718–729 (2007).
DOI: 10.1002/macp.200600614

[2] Duan J. K., Kim C. N., Jiang P. K.: On-line monitoring of cycloaliphatic epoxy/acrylate interpenetrating polymer networks formation and characterization of their mechanical properties. Journal of Polymer Research, **16**, 45–54 (2009).
DOI: 10.1007/s10965-008-9201-7

[3] Jordan J. L., Foley J. R., Siviour C. R.: Mechanical properties of Epon 826/DEA epoxy. Mechanics of Time-Dependent Materials, **12**, 249–272 (2008).
DOI: 10.1007/s11043-008-9061-x

[4] Jones I. K., Zhou Y. X., Jeelani S., Mabry J. M.: Effect of polyhedral-oligomeric-sil-sesquioxanes on thermal and mechanical behavior of SC-15 epoxy. Express Polymer Letters, **2**, 494–501 (2008).
DOI: 10.3144/expresspolymlett.2008.59

[5] Kaindl A., Rockelein R., Grindling J., Gehrig M.: Simulation of the curing process upon epoxy-resin casting ofelectrical apparaturses-a flexible way to do this. in ‘Electrical Insulating Materials, Proceedings of 1998 International Symposium on 27–30 Sept’ 277–280 (1998).
DOI: 10.1109/ISEIM.1998.741739

[6] Loos A. C., Springer G. S.: Curing of epoxy matrix composites. Journal of Composite Materials, **17**, 135–169 (1982).
DOI: 10.1177/002199838301700204

[7] Lee S-Y., Springer G. S.: Filament winding cylinders I. Process model. Journal of Composite Materials, **24**, 1270–1298 (1990).
DOI: 10.1177/002199839002401202

[8] Calius E. P., Lee S-Y., Springer G. S.: Filament winding cylinders II. Validation of the process model. Journal of Composite Materials, **24**, 1299–1343 (1990).
DOI: 10.1177/002199839002401203

[9] Lee S-Y., Springer G. S.: Filament winding cylinders III. Selection of process variables. Journal of Composite Materials, **24**, 1344–1366 (1990).
DOI: 10.1177/002199839002401204

[10] Bogetti T. A., Gillespie Jr J. W.: Two-dimensional cure simulation of thick thermosetting composites. Journal of Composite Materials, **25**, 239–273 (1991).

[11] White S. R., Hahn H. T.: Process modeling of composites materials: Residual stress development during cure. Part I. Model formulation. Journal of Composite Materials, **26,** 2402–2422 (1992).
DOI: 10.1177/002199839202601604

[12] White S. R., Hahn H. T.: Process modeling of composites materials: Residual stress development during cure. Part II. Experimental validation. Journal of Composite Materials, **26**, 2423–2453 (1992).
DOI: 10.1177/002199839202601605

[13] Ciriscioli P. R., Wang Q., Springer G. S.: Autoclave curing – Comparisons of model and test results. Journal of Composite Materials, **26**, 90–102 (1992).
DOI: 10.1177/002199839202600106

[14] Twardowski T. E., Lin S. E., Geil P. H.: Curing in thick composite laminates: Experiment and simulation. Journal of Composite Materials, **27**, 216–250 (1993).
DOI: 10.1177/002199839302700301

[15] Hojjati M., Hoa S. V. Curing simulation of thick thermosetting composites. Composites Manufacturing, **5**, 159–169 (1994).
DOI: 10.1016/0956-7143(94)90025-6

[16] White S. R., Kim Y. K.: Staged curing of composite materials. Composites Part A: Applied Science and Manufacturing, **27**, 219–227 (1996).
DOI: 10.1016/1359-835X(95)00023-U

[17] Yi S., Hilton H. H., Ahmad M. F.: A Finite element approach for cure simulation of thermosetting matrix composite. Computers and Structures, **64**, 383–388 (1997).
DOI: 10.1016/S0045-7949(96)00156-3

[18] Kim J. S., Lee D. G.: Development of an autoclave cure cycle with cooling and reheating steps for thick thermoset composite laminates. Journal of Composite Materials, **31**, 2264–2282 (1997).
DOI: 10.1177/002199839703102203

[19] Blest D. C., Duffy B. R., McKee S., Zulkifle A. K.: Curing simulation of thermoset composites. Composites Part A: Applied Science and manufacturing, **30**, 1289–1309 (1999).
DOI: 10.1016/S1359-835X(99)00032-9

[20] Park H. C., Lee S. W.: Cure simulation of thick composite structures using the finite element method. Journal of Composite Materials, **35**, 188–201 (2001).
DOI: 10.1177/002199801772662217

[21] Oh J. H., Lee D. G.: Cure cycle for thick glass/epoxy composite laminates. Journal of Composite Materials, **36**, 19–45 (2002).
DOI: 10.1177/0021998302036001300

[22] Park H. C., Goo N. S., Min K. J., Yoon K. J.: Three-dimensional cure simulation of composite structures by the finite element method. Composite Structures, **62**, 51–57 (2003).
DOI: 10.1016/S0263-8223(03)00083-7

[23] Guo Z-S., Du S. Y., Zhang B. M.: Temperature field of thick thermoset composite laminates during cure process. Composites Science and Technology, **65**, 517–523 (2005).
DOI: 10.1016/j.compscitech.2004.07.015

[24] Yan X.: Finite element modeling of curing of epoxy matrix composites. Journal of Applied Polymer Science, **103**, 2310–2319 (2007).
DOI: 10.1002/app.24337

[25] Yan X. Q.: Finite element simulation of cure of thick composite: Formulation and validation verification. Journal of Reinforced Plastics and Composites, **27**, 339–355 (2008).
DOI: 10.1177/0731684407083007

eXPRESS Polymer Letters Vol.3, No.9 (2009) 542–552
Available online at www.expresspolymlett.com
DOI: 10.3144/expresspolymlett.2009.68

The effect of zinc oxide nanoparticle morphology on activity in crosslinking of carboxylated nitrile elastomer

*M. Przybyszewska**, *M. Zaborski*

Institute of Polymer and Dye Technology, Technical University of Lodz, Stefanowskiego 12/16, Lodz 90-924, Poland

Received 27 April 2009; accepted in revised form 9 June 2009

Abstract. The aim of this work was to study the activity of several nanosized zinc oxides in the crosslinking of carboxylated nitrile elastomer (XNBR). In this article, we discuss the effect of zinc oxide nanoparticles with respect to their specific surface area, particle size and morphology (spheres, whiskers, and snowflakes) on the crosslinking density and mechanical properties of vulcanisates.

The morphology of nanoparticles considerably influences the activity of zinc oxide towards carboxylated nitrile rubber. As a crosslinking agent, zinc oxide with snowflake particles seems to be the most active. The application of nanosized zinc oxide allows the amount of ZnO to be reduced by almost 40%, as compared to vulcanisates containing microsized particles. Moreover, vulcanisates crosslinked with zinc oxide nanoparticles exhibit thermoplastic properties that enable this material to be recycled, which is very important from an ecological point of view.

Keywords: *nanocomposites, rubber, mechanical properties, zinc oxide, carboxylated nitrile elastomer*

1. Introduction

Carboxylated nitrile rubber (XNBR) can be crosslinked by sulphur with accelerators; however, the most relevant method is the application of bivalent metal oxides, especially zinc oxide (ZnO) [1, 2]. The crosslinking of elastomer occurs via the reaction of its carboxylic groups with zinc oxide, resulting in the formation of carboxylic salts, considered to be ionic crosslinks. In contrast to the covalent crosslinks formed during conventional vulcanisation with sulphur/accelerator systems or peroxides, ionic crosslinks are multifunctional and labile [3]. Carboxylic salts group together, forming clusters or multiplets [4]. According to Ibarra and Alzorriz [2], multiplets consist of six to eight dipole ions associated to form larger multiplets, which disperse in the elastomer matrix without forming a separate phase. These multiplets have a considerable impact on the glass transition temperature of the elastomer and its sensitivity to water. Clusters are considered as ionic aggregates, in separate ion-pair-rich regions, immersed in an elastomer matrix [1]. The presence of ionic clusters is responsible for the improved physical properties of ionic elastomers, even without filler addition, as compared to those conventionally crosslinked with sulphur and accelerators [5, 6]. The proportion of ionic crosslinks present in the form of multiplets or clusters in the elastomer network depends on the nature and structure of the elastomer macromolecule as well as the chemical nature and concentration of the carboxylic salt groups [2, 7]. According to Eisenberg and King [8], clusters are formed by the association of multiplets. This association is caused by electrostatic interactions between multiplets and is impaired by the retractive elastic forces of the backbone chains. The restricted elastomer chain mobility in the proximity of ionic clusters results in the

---

*Corresponding author, e-mail: magdalena.przybyszewska@p.lodz.pl formation of a hard phase. The presence of a hard phase in ionic elastomers or ionomers has been confirmed by measurements of dynamic mechanical properties, demonstrating the occurrence of a biphasic transition in XNBR/zinc oxide composites [9, 10]. Apart from the low glass transition temperature of elastomers, there is a high transition temperature due to the formation of a hard phase arising from the ionic clusters. Mandal *et al.* [5] confirmed the relationship between the high temperature transition and the presence of ionic aggregates in elastomer networks. Treatment of crosslinked samples with ammonia vapour caused the disappearance of the high temperature transition in the dynamic mechanical spectra. Ammonia acts as a plasticiser for the ionic aggregates, forming coordinating bonds with zinc ions of carboxylic salts or solvating the carboxylic ions. As a result, the ionic clusters are resolved, and the vulcanisate mechanical properties deteriorate.

Zinc oxide is a very effective and commonly used crosslinking agent for carboxylated elastomers [5, 10–13]. It can be used to produce vulcanisates with high tensile strength, tear resistance, hardness and hysteresis. The improved mechanical properties of ionic elastomers mainly result from their high ability for stress relaxation, due to elastomer chain slippage on the ionic cluster surface and reformation of ionic bonds upon external deformation of the sample. Moreover, ionic elastomers possess a thermoplastic character and can be processed in a molten state as a thermoplastic polymer [14]. However, there are some disadvantages to zinc-oxide-crosslinked carboxylic elastomers. The most important are the scorchiness, poor flex properties and high compression set [13]. In order to prevent scorchiness, carboxylated nitrile elastomers are crosslinked with zinc peroxide [2] or zinc peroxide/zinc oxide systems [13]. The vulcanisation of XNBR with zinc peroxide mainly leads to the formation of ionic crosslinks; covalent links are also formed between elastomer chains due to the peroxide action. However, higher vulcanisation times are required to achieve vulcanisates with a tensile strength and crosslink density comparable to that of vulcanisates crosslinked with zinc oxide [2]. In the case of XNBR vulcanisation with zinc peroxide/zinc oxide systems, the curing is the sum of at least three processes: a very fast formation of ionic crosslinks due to the initial zinc oxide present, peroxide crosslinking that leads to the formation of covalent links (peroxide action) and ionic crosslinking due to the production of zinc oxide from peroxide decomposition. The last process, which decays with vulcanisation time, is most likely related to the formation of ionic species [13]. The achieved vulcanisation times are considerably higher, as compared to those of XNBR crosslinking with zinc oxide. Therefore, apart from the scorch problems, zinc oxide is still commonly used as a crosslinking agent of carboxylated nitrile rubbers.

Taking into account the fact that, during the crosslinking process, zinc oxide reacts with carboxylic groups of elastomer, which leads to the formation of carboxylic salts (ionic crosslinks), the most important parameters influencing zinc oxide activity are its specific surface area, particle size and morphology. These parameters determine the size of the interphase between the crosslinking agent and elastomer chains.

The influence of zinc oxide particle size on the curing of carboxylated rubbers was reported by Hamed and Hua [15]. However, there are still some important aspects, which should be clarified. The effect of zinc oxide particle morphology on the crosslinking process and vulcanisate properties has not yet been reported.

In this work, we applied zinc oxides with different specific surface areas, particle sizes and morphologies (spheres, whiskers, snowflakes) as crosslinking agents of carboxylated nitrile elastomer, in order to determine the relationship between zinc oxide characteristics and activity in the crosslinking process.

2. Experimental section

2.1. Materials

Carboxylated nitrile elastomer XNBR (Krynac X7.50) containing 27 wt% acrylonitrile and 6.7 wt% carboxylic groups was obtained from Bayer C.O. The Mooney viscosity was (ML1+4 (100°C):47). Zinc oxides with different specific surface areas, particle sizes and morphologies were applied as crosslinking agents. Didodecyldimethylammonium bromide (DDAB, Fluka) was used to improve the dispersion of the zinc oxide particles in the elastomer matrix.

The physical characteristics of the zinc oxides applied are given in Table 1.

Table 1. Characteristics of zinc oxides

Symbol	Specific surface area [m²/g]	Particle morphology	Producer
ZnO 10	10.00	spheres and rods	Sigma-Aldrich
ZnO 15	15–25	whiskers	Sigma-Aldrich
ZnO 24	24.43	snowflakes	Institute of High Pressure Physics, Polish Academy of Science
ZnO 40	40.86	spheres	Institute of High Pressure Physics, Polish Academy of Science
ZnO 42	42.50	spheres	Qinetiq Nanomaterials Limited
ZnO 50	50.00	spheres	Nanostructured & Amorphous Materials, Inc.

2.2. Zinc oxide specific surface area

The specific surface area of zinc oxide was measured using low-temperature nitrogen adsorption (78 K) method with Sorptomatic 1900 (Fisons Instruments) apparatus. The specific surface area was determined with BET method based on the first section of nitrogen adsorption isotherm for $P/P_0 = 0.05–0.35$. Before the measurement zinc oxide was vacuum out-gassed in the temperature 373 K for 24 h.

2.3. Zinc oxide aggregate size

The size of the zinc oxide aggregates was determined using a Zetasizer Nano Series S90 (Malvern Instruments) apparatus. The size of the zinc oxide particles in water suspensions was measured based on the DLS (Dynamic Light Scattering) method. The concentration of the suspensions was 0.05 g/l.

2.4. Preparation and characterisation of rubber compounds

Rubber compounds with the formulation given in Table 2 were prepared using a laboratory two-roll mill. The samples were cured at 160°C until they developed a 90% increase in torque, measured by an oscillating disc rheometer.

The crosslink density (ν_T) of the vulcanisates was determined by equilibrium swelling in toluene, based on the Flory-Rehner equation [16]. The Huggins parameter of the elastomer-solvent interaction χ was calculated from Equation (1) [12]:

$$\chi = 0.487 + 0.228V_r \qquad (1)$$

Table 2. Composition of the XNBR-based rubber compounds [phr]

XNBR	100	100	100	100
ZnO	3	5	6	8
DDAB	1	1	1	1

where V_r is the volume fraction of elastomer in the swollen gel. In order to determine the content of ionic crosslinks in the elastomer network, samples were swollen in toluene in a dessicator with saturated ammonia vapour (25% aqueous solution). The content of ionic crosslinks ($\Delta\nu$) was calculated from Equation (2):

$$\Delta\nu = \frac{\nu_T - \nu_A}{\nu_T}\cdot 100\% \qquad (2)$$

where ν_A is the crosslink density determined for samples treated with ammonia vapour using the Huggins elastomer-solvent interaction parameter described by Equation (3) [17]:

$$\chi = 0.483 + 0.320V_r \qquad (3)$$

The tensile properties of the vulcanisates were determined according to ISO-37, with a ZWICK 1435 universal machine.

2.5. Dynamic-mechanical analysis

Dynamic-mechanical measurements were carried out in the tension mode using a DMTA V visco-analyser (Rheometric Scientific). Measurements of the dynamic moduli were performed over the temperature range (–100–150°C) with a heating rate of 2°C/min, at a frequency of 1 Hz and a strain amplitude of 0.02%. The temperature of the elastomer glass transition was determined based on the maximum of $\tan\delta = f(T)$, where $\tan\delta$ is the loss factor and T is the measurement temperature.

2.6. Shrinkability measurements

In order to measure the shrinkability of the XNBR vulcanisates, the samples were stretched at ambient temperature until reaching an elongation of 300% at the time 48 h; they were then stabilised in the stretched form at (–7°C) for 8 h. Finally, the stretched samples were allowed to shrink at 70°C for 48 h. The lengthwise shrinkage was calculated according to Equation (4) [18]:

$$S_h[\%] = \frac{L_{str} - L_{shr}}{L_{str}} \cdot 100 \qquad (4)$$

where S_h is the percentage of shrinkability, L_{str} is the length of the sample after stretching, and L_{shr} is the length of the shrunk sample.

2.7. Scanning Electron Microscopy (SEM)

The morphology of the zinc oxide particles and their dispersion in the elastomer matrix were estimated using Scanning Electron Microscopy with a LEO 1530 SEM microscope. The XNBR vulcanisates were broken down in liquid nitrogen, and the fracture surfaces of the vulcanisate were examined. Prior to the measurements, the samples were coated with carbon.

3. Results and discussion

3.1. Zinc oxide particle size and morphology

The particle size of zinc oxide is a main parameter that has a great influence on the ZnO activity. A reduction in particle size results in an increase in the zinc oxide specific surface area, providing better contact between the crosslinking agent particles and the elastomer chains. Moreover, the morphology of the ZnO particles determines the size of the interphase between zinc oxide and the elastomer. The sizes of the zinc oxide aggregates are presented in Table 3. Figure 1 shows the distribution of particle sizes as a function of particle number.

The morphologies of the zinc oxide particles or aggregates are presented in Figure 2a–2f.

Agglomerates of microsized zinc oxide (Figure 2a) used commercially in XNBR crosslinking consisted of primary particles with a wide size distribution from several hundreds of nanometres to several micrometres. The ZnO 10 particles revealed a variety of morphologies and irregular shapes (deformed spherical particles, elongated rods and blocks with sharp edges). The microsized ZnO agglomerates were broken down upon ultrasonic treatment. The aggregate size distribution determined in water dispersion ranged from 1.9–2.7 µm, with the main aggregate fraction at 2.1 µm (46%).

Table 3. Zinc oxide aggregate size

Zinc oxide	Aggregate size [nm]	Size of the aggregate main fraction [nm]	Number [%]
ZnO 10	1886–2671	2118	46
ZnO 15	185–664	371	26
ZnO 24	147–262	185	35
ZnO 40	92–131	116	38
ZnO 42	185–295	234	36
ZnO 50	130–208	165	36

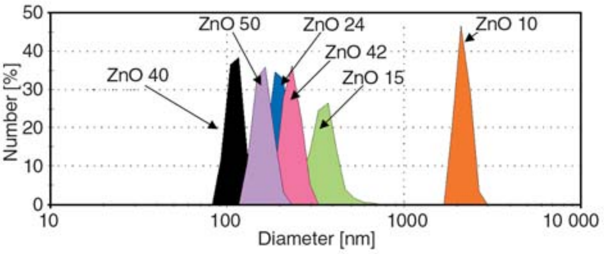

Figure 1. Zinc oxide particle size distribution by number

The ZnO 15 particles were elongated whiskers with a length of 100–300 nm and a diameter below 100 nm (Figure 2b). The aggregate size, as determined in water, was within the range of 185–664 nm, with the size of the main number fraction being 371 nm (26%). However, in the case of elongated particles, the orientation of the whiskers in the field of laser radiation influenced the obtained data. Therefore, it could be supposed that the measured particle size was a combination of whisker diameter and length.

Interesting morphological structures were observed in the case of ZnO 24 (Figure 2c). Zinc oxide aggregates revealed a shape of snowflakes or three-dimensional flowers consisting of several wires and plates growing from a single core. The primary particles with a size of about 200 nm formed microsized aggregates. In water dispersion, the size of the zinc oxide aggregates was reduced upon ultrasonic treatment to 185 nm (35%) (Table 3).

Zinc oxides with specific surface areas of 40.86, 42.5 and 50 m^2/g were found to be spherical with a size of about 100 nm, which agglomerated, forming clusters 10–20 µm in size (Figure 2d–2f). Upon ultrasonic treatment, the ZnO agglomerates were reduced in the water dispersion to aggregates with sizes ranging from 92–131 nm (ZnO 40), 185–295 nm (ZnO 42) and 130–208 nm (ZnO 50) (Table 3).

Elastomers have a hydrophobic nature; therefore, the size of the zinc oxide particles was measured in a liquid hydrophobic medium-paraffin oil, which was chosen as the model for an elastomer matrix (Table 4). The aim of this study was to estimate the

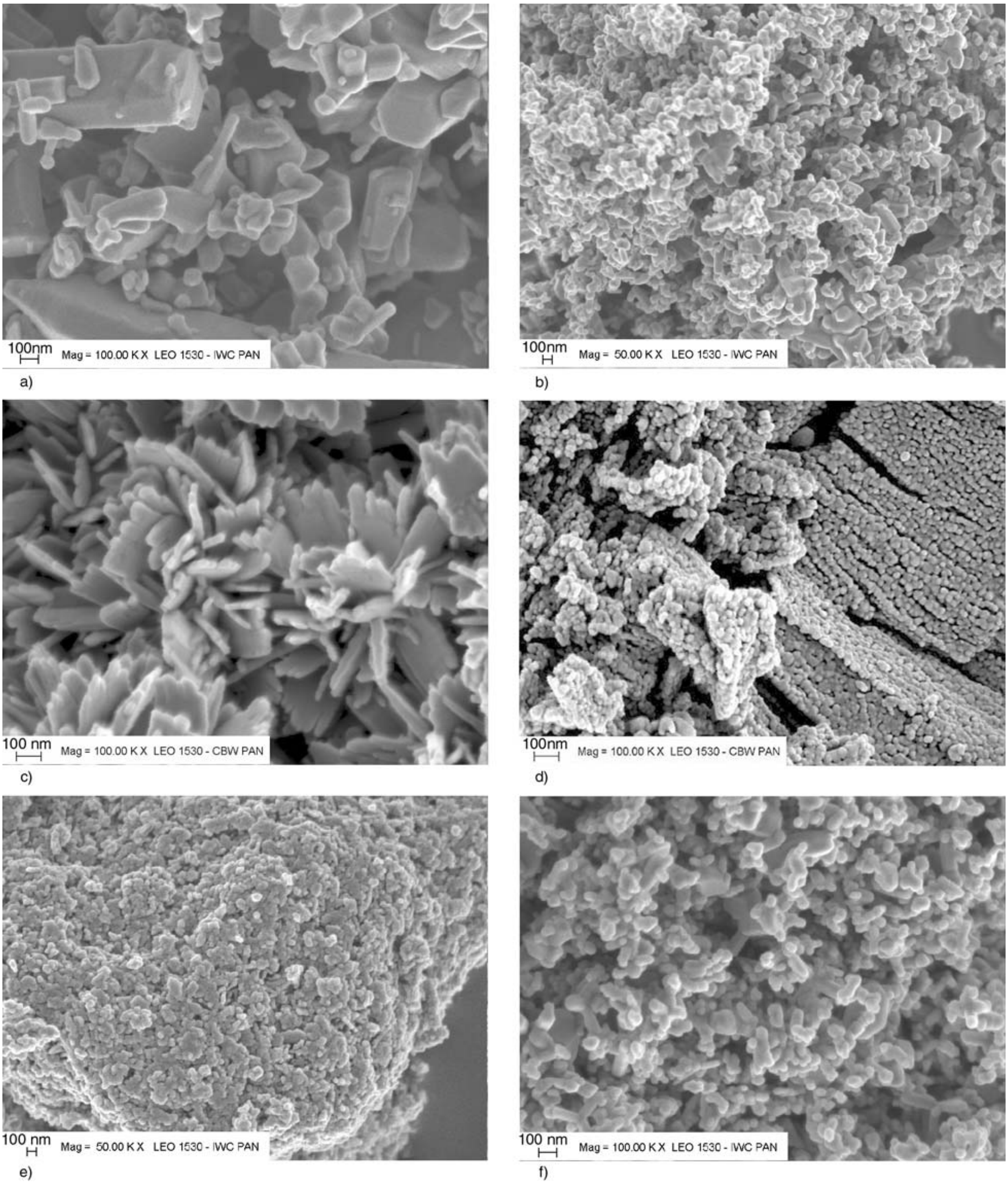

Figure 2. SEM images of zinc oxides: a) ZnO 10, b) ZnO 15, c) ZnO 24, d) ZnO 40, e) ZnO 42, f) ZnO 50

Table 4. Zinc oxide agglomerate size in paraffin oil

Zinc oxide	Agglomerate size [μm]
ZnO 10	10.0
ZnO 15	7.9
ZnO 24	7.9
ZnO 40	1.3
ZnO 42	9.3
ZnO 50	5.4

tendency of zinc oxide particles to agglomerate in elastomer. Unfortunately, zinc oxide particles exhibited a high ability for aggregation or agglomeration in paraffin oil. Primary particles formed microsized clusters with sizes ranging from 1.3 μm (ZnO 40) to 10 μm (ZnO 10).

3.2. Dispersion of zinc oxide particles in elastomer matrix

Assuming that zinc oxide particles diffuse through the elastomer matrix and react with carboxylic groups of elastomer chains, forming ionic crosslinks, the dispersion of ZnO particles in elastomer has a great importance as far as the activity of zinc oxides and their influence on vulcanisate properties are concerned. The dispersion of nanoparticles in the elastomer was estimated based on the SEM images of vulcanisate surfaces (Figure 3a–3f).

The zinc oxide particles were poorly dispersed in the elastomer matrix and, therefore, were not homogeneously distributed (Figure 3a). They created microsized agglomerates with complex structures.

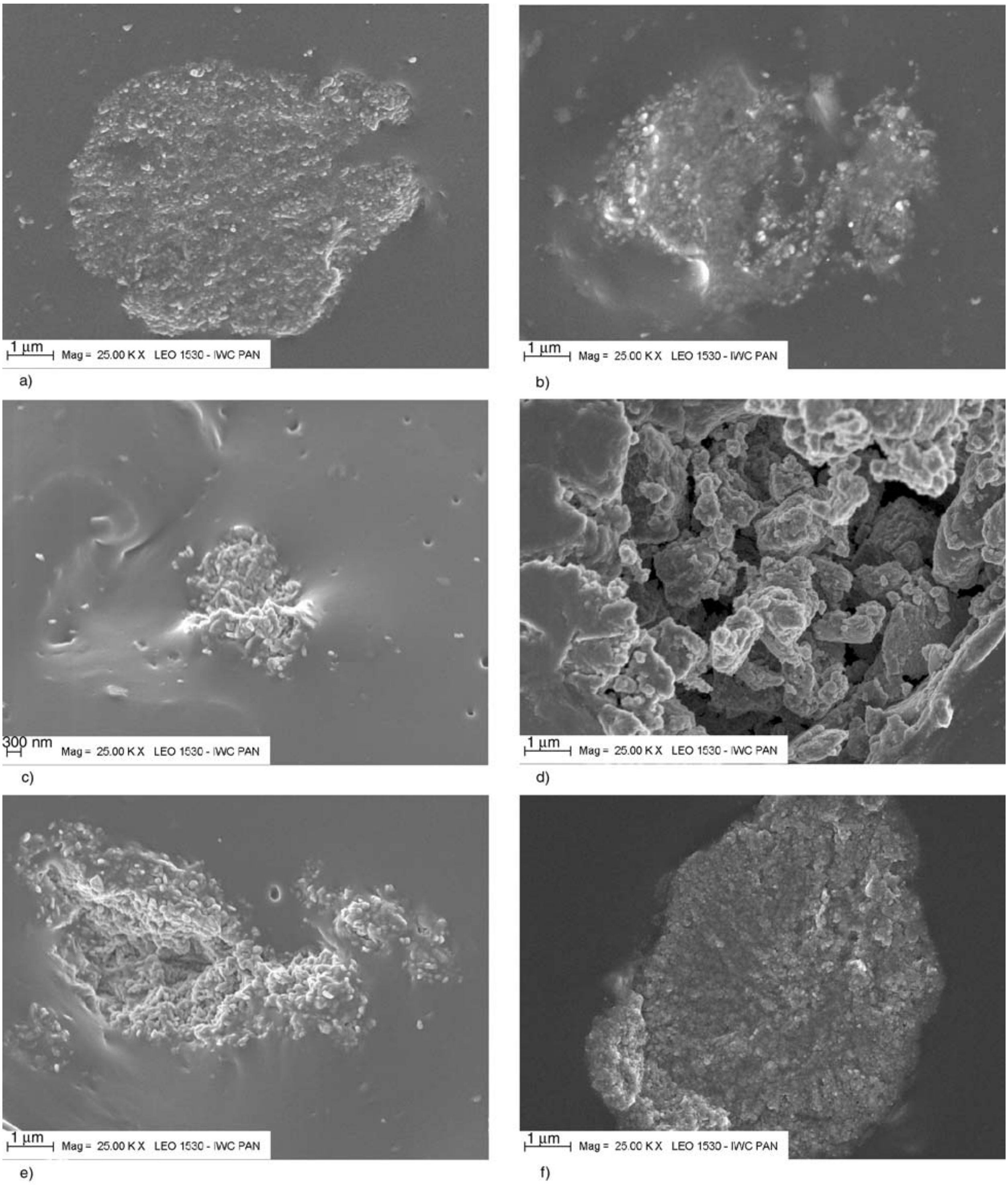

Figure 3. SEM images of XNBR vulcanisates with: a) ZnO 10, b) ZnO 15, c) ZnO 24, d) ZnO 40, e) ZnO 42, f) ZnO 50

The whisker particles of ZnO 15 (Figure 3b) created agglomerates several micrometres in size, which were surrounded by an elastomer film and were tightly bound to the elastomer matrix. It could be supposed that the wetting of ZnO 15 clusters with elastomer resulted in the good mechanical properties of the XNBR vulcanisates, despite the poor dispersion of the whiskers.

The ZnO 24 snowflake particles exhibited the weakest tendency to agglomerate. They created clusters about 3 μm in size (Figure 3c). The optimal dispersion of ZnO 24 in elastomer should lead to its high activity in the crosslinking process.

The spherical zinc oxide particles (ZnO 40, ZnO 42 and ZnO 50) were distributed very heterogeneously in the carboxylated nitrile rubber. The primary nanoparticles formed microsized agglomerates with irregular shapes, which displayed poor adhesion to the elastomer (Figure 3d–3f). Specifically, hollow structures were created by the ZnO 40 nanoparticles (Figure 3d). The strong tendency of ZnO nanoparticles to agglomerate arises from their high surface energy. The differences in the dispersed states of ZnO 40, ZnO 42 and ZnO 50 spherical nanoparticles in the elastomer resulted from different dispersive components of their surface energy and ability to undergo specific interactions. The influence of these parameters on the compatibility between zinc oxide particles and elastomer was thoroughly discussed [19]. The presence of impurities on ZnO 40 surface is probably the reason for its poor interfacial interaction with rubber. ZnO 40 was achieved by calcination of zinc oxalate, which was precipitated from hydrous solution of ammonium oxalate. Therefore, it contains some residues of hydroxyl groups, that remained after reaction. Moreover, the lowest content of crystalline phase (88%) compared to other zinc oxides (95–98%) as well as the presence of defects (oxygen vacancies) in the crystalline structure of ZnO 40 affect its activity towards XNBR elastomer.

3.3. Mechanical properties and crosslink density of vulcanisates

The influence of zinc oxide particle size and morphology on the activity in crosslinking of carboxylated nitrile elastomer was estimated based on the tensile properties and crosslink density of the vulcanisates. The results are given in Table 5 and Figure 4.

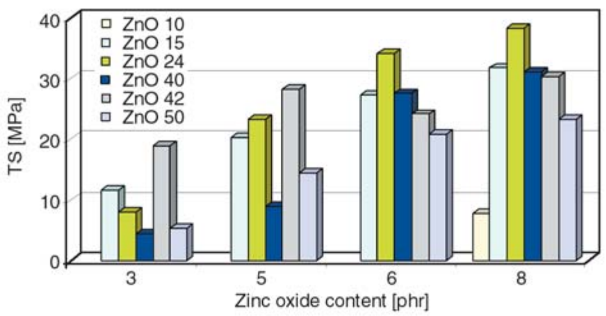

Figure 4. Tensile strength of XNBR vulcanisates

From the data presented in Figure 4, it follows that the application of zinc oxide nanoparticles considerably increased the tensile strength of the vulcanisates, as compared to those produced using conventional microsized ZnO 10. The tensile strength of the vulcanisates increased with the amount of zinc oxide in the composite. Moreover, the stress at a relative elongation of 300% increased, and the elongation at break decreased, due to an increase in the vulcanisate crosslink density (Table 5). The increment in vulcanisate tensile strength with the amount of zinc oxide arises from the increase in ionic crosslink content in the elastomer network ($\Delta\nu$). The presence of strong and multifunctional labile ionic clusters, which are able to move on the surface of the solid zinc oxide particles, resulted in the high ability of vulcanisates for stress relaxation, and as a consequence, an improvement in mechanical strength was achieved. Moreover, the considerable chain slippage and reformation of bonds in the elastomer network upon external stress contributed to the increase in vulcanisate tensile strength.

It could be supposed that the activity of zinc oxides in the crosslinking process will rise with the specific surface area. The presented results prove that the morphology of zinc oxide particles affects the vulcanisate crosslink density and mechanical properties more strongly than the specific surface area. The highest tensile strength (about 40 MPa) was achieved with a vulcanisate containing zinc oxide with three-dimensional snowflake particles (ZnO 24) (Figure 4). Moreover, the highest crosslink density and ionic crosslink content in the elastomer network (70%) were achieved for vulcanisates crosslinked with ZnO 24. Most likely, the high activity of this zinc oxide arises from a better contact between the surface of the crosslinking

Table 5. Mechanical properties and crosslink density of XNBR vulcanisates

Zinc oxide	ZnO content [phr]	SE300 [MPa]	EB [%]	$\nu_T \cdot 10^6$ [mol/cm^3]	$\Delta\nu$ [%]
ZnO 10 (microsized)	8	3.6	426	24.1	29
ZnO 15 (whisker particles)	3	1.8	802	12.2	29
	5	2.4	740	14.1	27
	6	2.9	717	15.2	24
	8	3.2	709	20.9	42
ZnO 24 (snowflake particles)	3	1.6	871	27.0	45
	5	3.2	652	48.3	63
	6	4.8	617	62.9	70
	8	7.0	586	64.6	68
ZnO 40 (spherical particles)	3	1.6	705	8.9	28
	5	2.5	554	23.5	15
	6	3.3	580	29.1	17
	8	3.3	582	31.0	19
ZnO 42 (spherical particles)	3	2.5	579	17.1	16
	5	4.1	518	19.2	13
	6	4.8	576	23.6	11
	8	5.3	514	28.7	21
ZnO 50 (spherical particles)	3	1.2	861	20.0	49
	5	2.1	682	28.1	54
	6	2.9	620	30.6	67
	8	3.0	631	37.0	64

SE300 – stress at 300% relative elongation; TS – tensile strength; EB – elongation at break; ν_T – vulcanisate crosslink density; $\Delta\nu$ – content of ionic crosslinks in elastomer network

agent particles and the elastomer chains (especially elastomer carboxylic groups), as compared to other zinc oxides. The specific shape and complex structure of ZnO 24 aggregates cause an increase in the size of the interphase between the elastomer and the snowflake particles, as compared to the spheres. Moreover, ZnO 24 nanoparticles exhibited the best dispersion in the elastomer matrix, which also contributed to the higher tensile strength and crosslink density in these vulcanisates, especially containing the high amount of ZnO (6; 8 phr). High tensile strength was also observed for the vulcanisates containing zinc oxide with whisker particles (ZnO 15).

Among the zinc oxides with spherical particles, the highest tensile strength was observed for vulcanisates with ZnO 42, especially with the small amount of zinc oxide (3; 5 phr). The weaker activity of the other zinc oxides was probably due to the poor dispersion of the particles in the elastomer matrix. Large and expanded agglomerates could act as critical sites, which may generate microcracks and initiate breaking of the sample under external stress. Moreover, the agglomeration of zinc oxide particles caused the surface area to decrease, followed by a decrease in the size of the interphase between the zinc oxide and the rubber chains. ZnO 40 was observed to be less efficient as a crosslinking agent of carboxylated nitrile rubber, mainly due to the presence of hollow, large agglomerates with poor adhesion to the elastomer. Weak dispersion of ZnO 50 nanoparticles (Figure 3e) was also a reason for deterioration of vulcanisates tensile strength, despite the high content of ionic crosslinks.

It should be noticed that not only the size and morphology of ZnO nanoparticles or their tendency for agglomeration affect zinc oxide activity in elastomer crosslinking. The surface properties of ZnO and its ability to specific interactions, which were reported in our previous work [19], must be taken into account. Considering the zinc oxide acceptor-donor properties and the ability to undergo specific interactions, it was concluded that ZnO 15 and ZnO 24, which had strong interactions with donor solvents as well as ZnO 50, which strongly interacted with acetonitrile, are most prone to interactions with elastomers containing donor functional groups (e.g. nitrile groups –C≡N). From physicochemical point of view, these oxides reveal the highest activity towards carboxylated acrylonitrile-butadiene elastomer. As a consequence, vulcanisates with high content of ionic crosslinks were achieved.

In previous work, we proved that it is possible to reduce the amount of zinc ions in acrylonitrile-butadiene rubber [20]. It should be noted that the application of zinc oxide nanoparticles allowed the amount of ZnO to be reduced in XNBR compounds, without a detrimental effect on the vulcanisate properties. The highest reduction in the zinc oxide amount is possible in the case of ZnO 42, since the vulcanisates crosslinked with 3 phr of this oxide exhibited a tensile strength twice as great as that of vulcanisates produced with microsized zinc oxide, which is used commercially in crosslinking process. This is very important from an ecological point of view, because the European Union requires that the amount of zinc oxide be reduced as much as possible.

3.4. Dynamic-mechanical properties of vulcanisates

A dynamic-mechanical analysis was performed to confirm the existence of ionic clusters in the elastomer network. The loss factor tanδ, as a function of temperature, for the vulcanisates with microsized zinc oxide ZnO 10 and with zinc oxide ZnO 42 with spherical nanoparticles is presented as an example in Figure 5. The values of glass transition temperature T_g are given in Table 6.

The existence of two transitions can be observed. The first transition is the glass transition of the elastomer at low temperatures, with a maximum that represents T_g. The determined glass transition temperature for the vulcanisate with ZnO 10 was (–4.5°C), whereas for vulcanisates with zinc oxide nanoparticles Tg values were within the range from (–4.9°C) to (–5.5°C). Therefore, it can be concluded that the zinc oxide particle size and morphology did not affect the elastomer T_g value considerably. The presence of additional maxima in the tanδ plot at the temperatures 6°C (ZnO 10) and 17°C (ZnO 42) was probably due to the existence of differently immobilised elastomer phases on the ZnO particle surfaces.

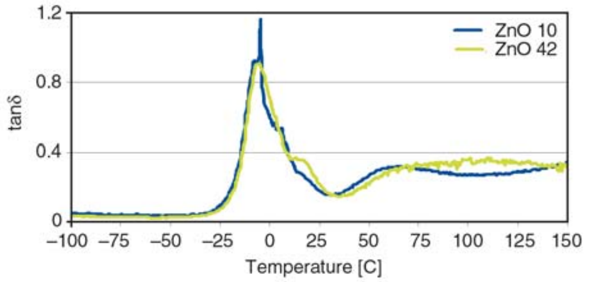

Figure 5. Tanδ versus temperature for XNBR vulcanisates containing zinc oxide

Table 6. Glass transition temperature of XNBR vulcanisates

Vulcanisate	T_g [°C]
XNBR/ZnO 10	–4.5
XNBR/ZnO 15	–5.1
XNBR/ZnO 24	–4.9
XNBR/ZnO 40	–5.5
XNBR/ZnO 42	–5.3
XNBR/ZnO 50	–5.1

The second transition is the ionic transition, occurring at high temperatures (50–100°C), resulting from the occurrence of a hard phase arising from ionic associations-ionic clusters or aggregates. Similar transitions were observed for all XNBR vulcanizates. This confirms the existence of a biphasic structure in the XNBR-ZnO system.

In the case of the vulcanisate containing ZnO 42, the considerable decrease in the tanδ versus temperature maximum resulted from higher interactions between ZnO 42 and the elastomer, which prevented the rubber chains from a free relaxation at the glass transition temperature.

3.5. Shrinkability of XNBR vulcanisates

Heat-shrinkable polymers are widely used in packaging and in the cable industry; therefore, the shrinkability of XNBR vulcanisates crosslinked with zinc oxide is very important from a technological point of view. According to Mishra *et al.* [18], the shrinkage of polymer occurs due to an internal rearrangement of the structural elements within the stretched sample. The shrinkage driving force originates from oriented polymer chains of crystalline and amorphous phase. In the case of polyolefin/elastomer blends, the crosslinked elastomeric phase causes an enhancement in the blend shrinkability upon heating. It is believed that crosslinked points in the elastomer network serve as memory points, enhancing the heat shrinkability [21].

The examined samples were stretched above the glass transition temperature T_g until reaching an elongation of 300%; they were then stabilised in the stretched form at (–7°C) and shrunk above the ionic transition temperature at 70°C. The heat shrinkability values of the XNBR samples containing 8 phr of zinc oxide are presented in Table 7.

Vulcanisates of carboxylated nitrile elastomer crosslinked with zinc oxides exhibited heat shrink-

Table 7. Shrinkability of XNBR vulcanisates

Vulcanisate	L_{str} [cm]	L_{shr} [cm]	S_h [%]
XNBR/ZnO 10	11.2	3.9	65
XNBR/ZnO 15	11.2	3.5	69
XNBR/ZnO 24	11.2	2.7	76
XNBR/ZnO 40	11.2	3.5	69
XNBR/ZnO 42	11.2	2.7	76
XNBR/ZnO 50	11.2	2.6	77

ability. The highest shrinkage upon heating (76 and 77%) was achieved for vulcanisates containing ZnO 24 snowflake nanoparticles and spherical particles of ZnO 42 and ZnO 50. The lower shrinkability of the vulcanisates with the other zinc oxides (ZnO 10, ZnO 15 and ZnO 40) resulted from a lower crosslink density and ionic crosslink content in the elastomer network. Since the crosslinked points in the elastomer network serve as shape memory sites, a higher crosslink density improves the shrinkability of the vulcanisate. The stretched XNBR samples were shrunk upon heating above the temperature of the ionic transition, due to the occurrence of ionic multiplets in the elastomer network, which are multifunctional and labile crosslinks. Therefore, it can be concluded that the decomposition or rearrangement of the ionic clusters is one of the causes of heat shrinkability in XNBR vulcanisates containing zinc oxide.

4. Conclusions

Zinc oxides with different particle sizes and morphologies were used as crosslinking agents of carboxylated nitrile elastomer.

We conclude that the application of zinc oxide nanoparticles allowed for the realisation of vulcanisates with considerably better mechanical properties and higher crosslink density, as compared to vulcanisates crosslinked with microsized zinc oxide, which is used commercially as a crosslinking agent. Vulcanisates containing the same amount of zinc oxide nanoparticles exhibited a tensile strength about four times greater than that of vulcanisates with microsized particles. Moreover, 3 phr of nanosized ZnO 15, ZnO 24 or ZnO 42 is sufficient to obtain composites with comparable or even better tensile strengths, as compared to vulcanisates containing 8 phr of industrially used microsized ZnO. Therefore, the application of nanosized zinc oxide allows the amount of zinc oxide to be reduced by almost 40%. This is a very important ecological goal, since zinc oxide is classified as toxic to aquatic species, and the European Union requires that the amount of zinc oxide in rubber compounds be reduced. Moreover, it should be noted that vulcanisates of carboxylated nitrile elastomer crosslinked with zinc oxide reveal heat shrinkability.

The morphology of zinc oxide particles mainly affects the activity in the crosslinking process. Particle size or zinc oxide specific surface area does not seem to have a considerable influence on the crosslinking agent efficiency. The highest activity was observed for zinc oxide with a specific surface area of 24.43 m^2/g and three-dimensional snowflake particles (ZnO 24). The specific shape and complex structure of ZnO 24 aggregates, consisting of wires or plates growing from a single core, provide an increase in the size of the interphase between the elastomer carboxylic groups and the snowflake particles. As a result, vulcanisates with higher crosslink density and ionic crosslink content are achieved. These vulcanisates exhibit the best mechanical properties (TS about 40 MPa), mainly due to the high content of ionic clusters, which are multifunctional and labile crosslinks and can rearrange upon external stress, leading to stress relaxation. Moreover, ZnO 24 nanoparticles have the lowest ability for agglomeration in the elastomer matrix and create the smallest agglomerates, which concentrate the stresses during sample deformation to a smaller degree, as compared to the large agglomerates formed by other zinc oxides.

Acknowledgements

The authors wish to acknowledge the Polish Ministry of Science and Higher Education for supporting this research.

References

[1] Ibarra L., Rodriguez A., Mora I.: Ionic nanocomposites based on XNBR-OMg filled with layered nanoclays. European Polymer Journal, **43**, 753–761 (2007).
DOI: 10.1016/j.eurpolymj.2006.12.007

[2] Ibarra L., Alzorriz M.: Vulcanization of carboxylated nitrile rubber (XNBR) by zinc peroxide. Polymer International, **48**, 580–586 (1999).
DOI: 10.1002/(SICI)1097-0126(199907)48:7<580::AID-PI186>3.0.CO;2-4

[3] Dunn J. R.: Carboxylated rubber. in 'Handbook of Elastomers' (eds.: Bowmick A. K., Stephens H. L.) Marcel Dekker, New York, 561–590 (2001).

[4] Eisenberg A.: Clustering of ions in organic polymers. A theoretical approach. Macromolecules, **3**, 147–154 (1970).
DOI: 10.1021/ma60014a006

[5] Mandal U. K., Tripathy D. K., De S. K.: Dynamic mechanical spectroscopic studies on plasticization of an ionic elastomer based on carboxylated nitrile rubber by ammonia. Polymer, **37**, 5739–5742 (1996).
DOI: 10.1016/S0032-3861(96)00545-9

[6] Przybyszewska M., Zaborski M.: Nanoparticle zinc oxide applied for crosslinking of butadiene rubbers. in '8th European Symposium on Polymer Blends and Eurofillers. Bruges, Belgium' 116 (2005).

[7] MacKnight W. J.: Available ionomers. in 'Structure and properties of ionomers' (eds.: Pireni M., Eisenberg A.) NATO ASI Series C Mathematical and Physical Sciences, Vol. **198**, 1–10 (1986).

[8] Eisenberg A., King M.: Ion containing polymers. Academic Press, New York (1997).

[9] Mandal U. K., Tripathy D. K., De S. K.: Effect of silica filler on dynamic mechanical properties of ionic elastomer based on carboxylated nitrile rubber. Journal of Applied Polymer Science, **55**, 1185–1191 (2003).
DOI: 10.1002/app.1995.070550805

[10] Mandal U. K., Tripathy D. K., De S. K.: Effect of carbon black fillers on dynamic mechanical properties of ionic elastomer based on carboxylated nitrile rubber. Plastics, Rubber and Composites Processing and Application, **24**, 19–25 (1995).

[11] Fritzsche J., Das A., Jurk R., Stöckelhuber K. W., Heinrich G., Klüppel M.: Relaxation dynamics of carboxylated nitrile rubber filled with organomodified nanoclay. Express Polymer Letters, **2**, 373–381 (2008).
DOI: 10.3144/expresspolymlett.2008.44

[12] Zaborski M., Kosmalska A.: Silica modified by use of organosilanes as a filler for carboxylated butadiene-acrylonitrile rubber. Kautschuk Gummi Kunststoffe, **58,** 354–357 (2005).

[13] Ibarra L., Marcos-Fernandez A., Alzorriz M.: Mechanistic approach to the curing of carboxylated nitrile rubber (XNBR) by zinc peroxide/zinc oxide. Polymer, **43**, 1649–1655 (2002).
DOI: 10.1016/S0032-3861(01)00734-0

[14] Chatterjee K., Naskar K.: Development of thermoplastic elastomers based on maleated ethylene propylene rubber (m-EPM) and polypropylene (PP) by dynamic vulcanization. Express Polymer Letters, **1**, 527–534 (2007).
DOI: 10.3144/expresspolymlett.2007.75

[15] Hamed G. R., Hua K-C.: Effect of ZnO particle size on the curing of carboxylated NBR and carboxylated SBR. Rubber Chemistry and Technology, **77**, 214–226 (2004).

[16] Flory P. J., Rehner J.: Statistical mechanics of cross-linked polymer networks. II. Swelling. Journal of Chemical Physics, **11**, 521–526 (1943).
DOI: 10.1063/1.1723792

[17] Przepiórkowska A., Chrońska K., Zaborski M.: Chrome-tanned leather shavings as a filler of butadiene-acrylonitrile rubber. Journal of Hazardous Materials, **141**, 252–257 (2007).
DOI: 10.1016/j.jhazmat.2006.06.136

[18] Mishra J. K., Raychowdhury S., Das C. K.: Effect of interchain crosslinking on the shrinkability of the blends consisting of grafted low-density polyethylene and carboxylated nitrile rubber. Materials Letters, **46**, 212–218 (2000).
DOI: 10.1016/S0167-577X(00)00172-5

[19] Przybyszewska M., Krzywania A., Zaborski M., Szynkowska M. I.: Surface properties of zinc oxide nanoparticles studied by inverse gas chromatography. Journal of Chromatography A, **1216**, 5284–5291 (2009).
DOI: 10.1016/j.chroma.2009.04.094

[20] Przybyszewska M., Zaborski M., Jakubowski B., Zawadiak J.: Zinc chelates as new activators for sulphur vulcanization of acrylonitrile-butadiene elastomer. Express Polymer Letters, **3**, 256–266 (2009).
DOI: 10.3144/expresspolymlett.2009.32

[21] Patra P. K., Das C. K.: Blends of polyolefins and chlorosulphonated polyethylene (CSM) with special reference to their shrinkability and flame retardancy. International Journal of Polymeric Materials, **35**, 103–118 (1997).
DOI: 10.1080/00914039708039757

eXPRESS Polymer Letters Vol.3, No.9 (2009) 553–559
Available online at www.expresspolymlett.com
DOI: 10.3144/expresspolymlett.2009.69

Chitosan-*g*-polyaniline: a creatine amidinohydrolase immobilization matrix for creatine biosensor

A. Tiwari[1*], *S. K. Shukla*[2]

[1]Division of Engineering Materials, National Physical Laboratory, Dr. K.S. Krishnan Marg, New Delhi-110 012, India (Present address: Department of Mechanical Engineering, University of Wisconsin-Milwaukee, Milwaukee, WI 53211, USA)
[2]Department of Polymer Science, Bhaskaracharya College of Applied Sciences, University of Delhi, New Delhi-110 075, India

Received 7 May 2009; accepted in revised form 13 June 2009

Abstract. A novel matrix composed of chitosan-graft-polyaniline (CHIT-*g*-PANI) was electrochemically prepared to investigate the immobilization of creatine amidinohydrolase (CAH). CAH enzyme was covalently immobilized with the CHIT-*g*-PANI matrix using glutaraldehyde as a linker. The resulting CAH/CHIT-*g*-PANI biomatrix was characterized with Fourier transform infrared spectroscopy (FTIR), atomic force microscopy (AFM), contact angle measurement and cyclic voltammetry (CV) taking CHIT-*g*-PANI as a reference. The influence of various parameters on CAH enzyme activity within the matrix was investigated including pH, temperature, and time. The Michaelis-Menten constant and apparent activities for the CAH enzyme were calculated to be 0.51 mM and 83.59 mg/cm^2, respectively; indicating CHIT-*g*-PANI matrix has a high affinity to immobilize CAH enzyme.

Keywords: *polymer synthesis, molecular engineering, chitosan-graft-polyaniline, creatine amidinohydrolase, immobilization matrix*

1. Introduction

Creatinine is an important clinical analyte for the diagnosis of renal and muscular dysfunction [1]. It is a dehydrogenated form of creatine (i.e., a metabolic byproduct of amino acid) that provides energy to muscles tissue. The normal clinical range of creatinine in the human blood is ranging from 44 to 106 µM; however, it can exceed up to 1000 µM during nephrons malfunction [2]. Therefore, precise monitoring of creatinine in the blood is compulsory during routine check up.

Most of the existing creatinine biosensors utilize creatine amidinohydrolase (CAH) as a sensing element [3–5]. Typically, CAH is a homodimer enzyme, which hydrolyzes creatinine into urea and sarcosine [6]. The concentration of creatinine is quantitatively measured by monitoring the librated hydrolyzed byproducts using a range of transducers such as amperometric, potentiometric, optical, etc. [7, 8]. However, these biosensors are offered only limited biosensor stability due to low functional stability of CAH enzyme within the matrix [9]. In practice, performance of enzyme based biosensors usually depends on the physicochemical properties of the electrode materials as well as process of the enzyme immobilization and also enzyme concentration on the electrode surface [10]. Although, various matrices are reported in the literature for the immobilization of CAH enzyme to use in creatinine biosensors, the method of immobilization and electrode matrices, both are considered promising factor during the determination of the operational and

---

[*]Corresponding author, e-mail: tiwari@uwm.edu

storage stability of the biosensors [11]. The low intrinsic stability of CAH enzyme has encouraged for applying biomaterials engineering to improving stability [12]. Specifically, this study investigates the feasibility of CHIT-*g*-PANI as potential CAH immobilization matrix.

Polyaniline (PANI) is a unique conducting polymer and its reversible conductivity can be controlled by the protonation of the imine sites or the oxidation of the main polymer chain [13]. However, traditional PANI does not have such enzyme loading capability as its chemically modified forms [14]. Meanwhile, Chitosan (CHIT) has become a widespread biopolymer owing to its remarkable chemical and biological characteristics. It is a hydrophilic material due to the presence of both amino and hydroxyl groups; however, CHIT is insoluble in water and aqueous basic media [15]. It was chosen as the orientation directing matrix because there are large quantities of amino and hydroxyl groups on the CHIT units, which have a strong binding ability to enzyme and DNA [14, 16]. Moreover, in acidic condition CHIT showed a cationic nature that may provide an electrostatic core environment to zwitterion molecules such as enzyme.

In the present work, we describe the fabrication of a novel matrix based on CHIT-*g*-PANI, covalent immobilization and stabilization conditions for the CAH enzyme. Further, Michaelis-Menten kinetic parameter and apparent activities for the CAH enzyme were calculated correspondingly using electrochemical and photometric techniques.

2. Experimental

2.1. Materials

Chitosan (CHIT, >85% deacetylated, M_w 1.86·10^5), aniline (99%), creatinine (anhydrous) and urease (Urs, from *Canavalia ensiformis*) were purchased from Sigma-Aldrich, USA. Creatine amidinohydrolase (CAH, from *Actinobacillus* sp., CRH-211) was taken from Toyobo Co., Ltd. and used without further purification. All supplementary chemicals were of analytical grades and solutions were prepared with nanopure water. Indium-tin-oxide (ITO) coated glass sheets (Balzers) with a resistance of 15 Ω/cm^2 were used as substrates for the deposition of electrodes.

2.2. Preparation of CHIT solution

CHIT solution was prepared by dissolving 2.0 g of CHIT flakes into 100 ml of 1.0% acetic acid and stirred for three hours at room temperature until completely dissolved. The CHIT solution was stored in a refrigerator when not in use.

2.3. Electrochemical synthesis of CHIT-*g*-PANI

Aniline (180 μl), and 2.0% CHIT solution (75 μl) was mixed with 10 ml of 0.5M HCl in an electrochemical cell and the mixture was ultrasonically agitated for about four hours. The CHIT-*g*-PANI was chronoamperometrically synthesized onto an ITO coated glass surface using a three-electrode assembly with ITO glass as working, platinum as counter, and Ag/AgCl as reference electrodes at a potential of 0.9 V and duration of 200 seconds. The resulting CHIT-*g*-PANI/ITO electrode was washed with deionized water followed by a phosphate buffer saline (PBS) solution of pH 7.0 in order to neutralize the electrode surface.

2.4. Immobilization of CAH enzyme

The CAH enzyme was covalently immobilized over the CHIT-*g*-PANI matrix using glutaraldehyde as a linker. Ten μl of 25% gluteraldehyde solution was spread over the CHIT-*g*-PANI/ITO

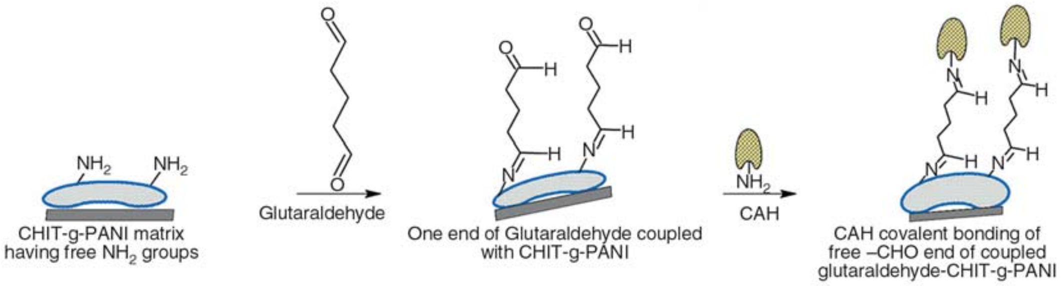

Figure 1. Covalent immobilization of the CAH on CHIT-*g*-PANI graft copolymer matrix using gluteraldehyde as a linker

electrode and kept for five hours at room temperature, then 10 µl CAH (350 units/µl) was spread on top of the electrode and dried (Figure 1). The resulting CAH/CHIT-*g*-PANI/ITO bioelectrode was thoroughly washed with PBS of pH 7.0 to rinse off any loosely bound CAH enzyme from the bioelectrode.

2.5. Characterization

CHIT-*g*-PANI and CAH/CHIT-*g*-PANI biomatrix were characterized using FTIR, AFM, contact angle, and CV measurements. FTIR spectra were recorded on a Perkin Elmer, Spectrum BX II spectrophotometer. The surface topology of the electrodes was studied using AFM (Veeco DICP2) under the tapping mode. Contact angles of the electrodes were measured with a video-based, automatic research grade contact angle measurement system, FDSC-OCA 20 using water as liquid phase.

Electrochemical measurements of the electrodes were carried out on a Potentiostat/Glavanostat (Princeton Applied Research, 273A) unit with three electrodes in a 50 mM phosphate buffer solution (pH 7.0, 0.9% NaCl) containing 5 mM $Fe(CN)_6^{3-/4-}$. The working electrode was either CHIT-*g*-PANI/ITO or CAH/CHIT-*g*-PANI/ITO. Platinum foil and Ag/AgCl were used as the counter and reference electrodes, respectively. All measurements were carried out at 25°C.

2.6. Photometric apparent enzyme activity measurement

Photometric study was performed using a Varian Cary 100 Bio UV-visible spectrophotometer. For photometric measurements, a CAH/CHIT-*g*-PANI/ITO bioelectrode was dipped in a 5 ml phosphate buffer solution (50 mM, pH 7.0), which contained 200 µl of Nessler's solution, 50 µl urease enzyme (50 mg/ml) and 1 ml of creatinine solution with varying concentrations. After 3 min of CAH/CHIT-*g*-PANI/ITO electrode incubation, the absorbance of the colored product (i.e., $NH_2Hg_2I_3$, a complex formed between the Nessler's reagent and ammonia produced by the enzymatic hydrolysis of creatinine) in the solution at λ_{max} 385 nm, was measured to monitor the CAH enzyme kinetics.

3. Results and discussion

3.1. Graft copolymerization, enzyme immobilization and characterization

In the electrochemical copolymerization synthesis, the aniline monomer initially became protonated with HCl and propagated to form an intermediate called PANI radical cation (Figure 2a) [17–19].

PANI radical cation simultaneously generated CHIT macro radicals (Figure 2b) by the abstraction of hydrogen from the –OH and $–NH_2$ groups of the CHIT macromolecules [15, 16].

The PANI cation radicals and CHIT macro radicals then copolymerized and yielded CHIT-*g*-PANI (Figure 2c).

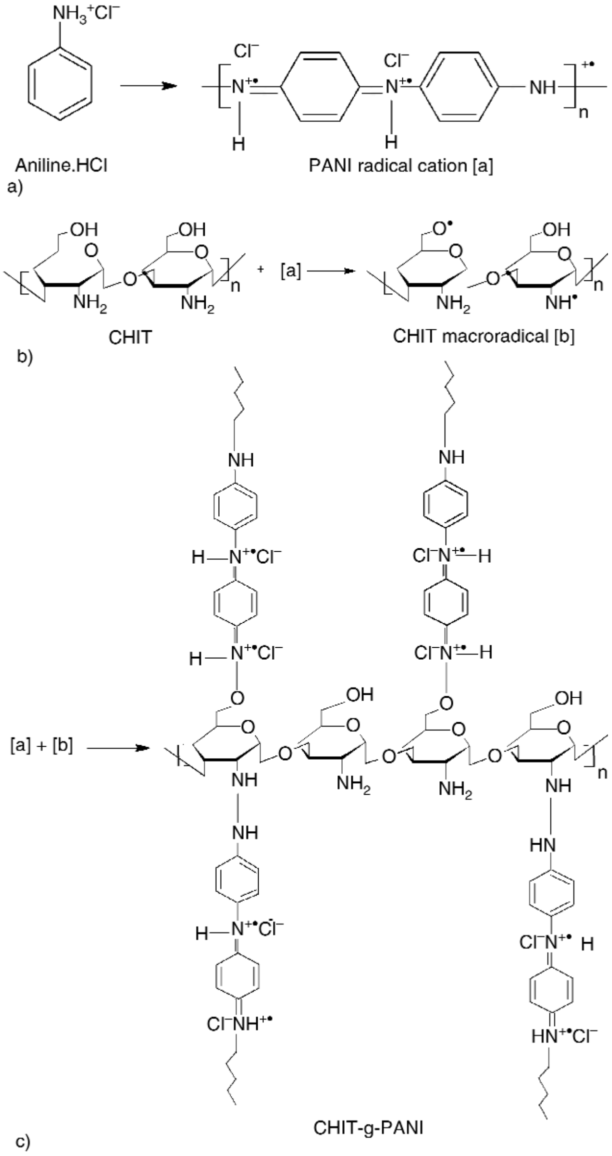

Figure 2. Electrochemical copolymerization synthesis. a) PANI radical cation, b) CHIT macro radical, c) CHIT-g-PANI

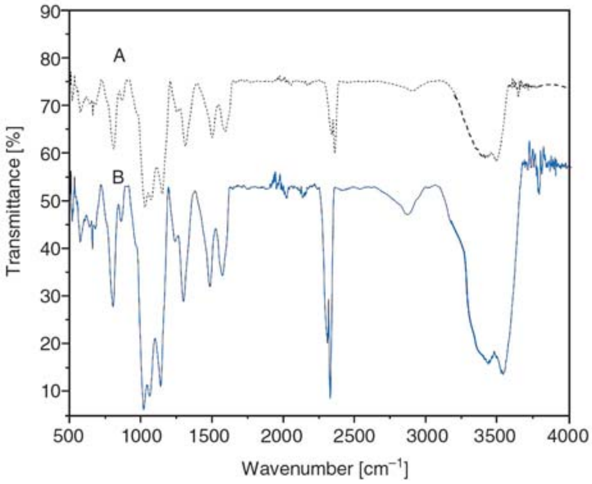

Figure 3. FTIR spectra of the (spectrum A) CHIT-*g*-PANI and (spectrum B) CAH/CHIT-*g*-PANI

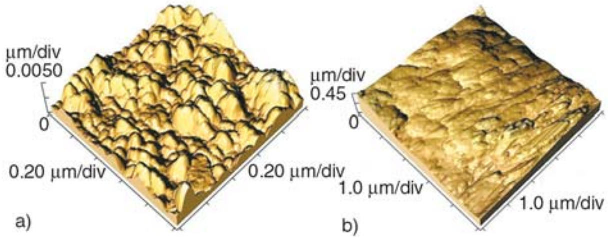

Figure 4. AFM images of the (a) CHIT-*g*-PANI and (b) CAH/CHIT-*g*-PANI

The FTIR spectrum of the CHIT-*g*-PANI/ITO electrode (Figure 3, spectrum A) illustrated the characteristic peaks of PANI, as well as CHIT [16]. The following key characteristic bands were observed: 1) 3150 to 3542 cm^{-1} (free O–H stretching and N–H stretching with hydrogen bonded secondary amino groups); 2) 3021 cm^{-1} (aromatic C–H stretching); 2926 and 2862 cm^{-1} (aliphatic C–H stretching); 3) 1632 cm^{-1} (C=O stretching of carbonyl group, typical saccharide absorption); 4) 1584 cm^{-1} (C=C stretching of quinoid rings); 5) 1483 cm^{-1} (C=C stretching vibration of benzenoid rings); and 6) 1245 cm^{-1} (C–N stretching). The absorption band of the N=Q=N bending vibration of protonated pure PANI was observed at 1236 cm^{-1}, but shifted to 1123 cm^{-1} in the CHIT-*g*-PANI copolymer due to the steric effect of CHIT [16].

Stable enzyme-substrate coupling was achieved with gluteraldehyde as a cross-linking agent [20]. One end of the gluteraldehyde is attached to the $–NH_2$ group of the CHIT-*g*-PANI/ITO electrode through a reaction between the –CHO end group of glutaraldehyde and the $–NH_2$ groups of terminal PANI and CHIT. The other end of the gluteraldehyde is attached to CAH through a reaction between the –CHO group of gluteraldehyde and $–NH_2$ group of CAH, which resulted in a CAH/CHIT-*g*-PANI/ITO bioelectrode (Figure 1). It may be possible that some of the glutaraldehyde attached within the free $–NH_2$ groups of the CHIT-*g*-PANI matrix but probability of cross linking between $–NH_2$ functionalized electrode to enzyme is quite common [20]. The FTIR spectrum of the CAH/CHIT-*g*-PANI/ITO electrode (Figure 3, spectrum B) showed phosphate vibration at 1224 cm^{-1} (accredited from phosphate backbone of immobilized cDNA) with the peaks broadening at 1) 3123 to 3564 cm^{-1} (addition of N–H stretching vibration); 2) 3022 to 2856 cm^{-1}; and 3) 1631 cm^{-1} to 1664 due to the attachment of CAH with the CHIT-*g*-PANI matrix. Hence, FTIR spectra confirmed the immobilization of CAH onto the CHIT-*g*-PANI/ITO electrode.

The surface morphology of the electrodes was observed with AFM and is shown in Figure 4. The CHIT-*g*-PANI/ITO electrodes exhibited a relatively rough surface topology in comparison to CAH/CHIT-*g*-PANI/ITO electrode, which may facilitate the immobilization of CAH onto the CHIT-*g*-PANI/ITO electrode. To study the relative surface hydrophilicity, the contact angles of CHIT-*g*-PANI/ITO and CAH/CHIT-*g*-PANI/ITO electrodes were measured [21] and were about 29±2° and 38±2°, respectively. The work of adhesion between the surface of the electrodes and the water droplet (W_a) can be calculated from the Young-Dupre Equation (1):

$$W_a = \gamma\,(1 + \cos\theta) \qquad (1)$$

where γ is the surface tension and θ is the contact angle. If the liquid is attracted to the solid surface (e.g., water on a strongly hydrophilic solid), the droplet will completely spread out on the solid surface and the contact angle will be close to 0°. According to this equation, the work of adhesion is higher at a lower contact angle. Since the contact angle increased after the CAH was immobilized on the surface of the CHIT-*g*-PANI/ITO electrode, this indicates that the CAH/CAH/CHIT-*g*-PANI/ITO electrode surface has a weaker affinity to the hydrophilic moiety than CHIT-*g*-PANI/ITO electrode surface.

3.2. Electrochemical measurement

Figure 5 shows the CVs of the electrochemical cells using either CHIT-*g*-PANI/ITO or CAH/CHIT-*g*-PANI/ITO electrode at a constant 50 mVs^{-1} scan rate in 50 mM phosphate buffer solution (pH 7.0, 0.9% NaCl) containing 5 mM $Fe(CN)_6^{3-/4-}$. The current of the electrochemical cell using the electrode CHIT-*g*-PANI/ITO ($7.69\cdot10^{-6}$ A) was about five times of that using the CAH/CHIT-*g*-PANI/ITO bioelectrode ($1.72\cdot10^{-6}$ A).

Thus, immobilizing CAH onto the bare electrode reduced the current. A decrease in current after the immobilization of CAH may be attributed to a slower redox behavior when compared with the bare CHIT-*g*-PANI/ITO electrode. The covalent binding of CAH on the CHIT-*g*-PANI/ITO electrode controls the moment of the supporting electrolytes [11]. Also, the non-conducting nature of the CAH molecules might have contributed to the decrease in current when using the CAH/CHIT-*g*-PANI/ITO electrode.

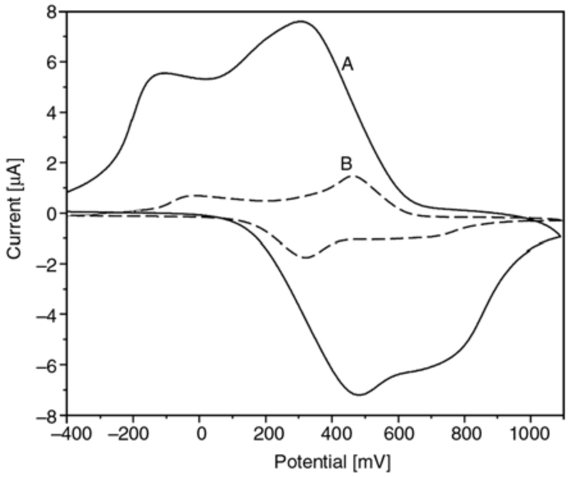

Figure 5. Cyclic voltammograms of the (A) CHIT-*g*-PANI/ITO and (B) CAH/CHIT-*g*-PANI electrodes in PBS (50 mM, pH 7.0, 0.9% NaCl, 5 mM $Fe(CN)_6^{3-/4-}$) at 50 mVs^{-1} scan rate

The affinity of CAH to the CHIT-*g*-PANI/ITO graft copolymer matrix was estimated using the Hanes plot [22]. The Michaelis-Menten kinetic parameter (K_m^{app}) was calculated to be 0.51 mM for the CAH/CHIT-*g*-PANI/ITO electrode. K_m^{app} usually depends on the electrode material as well as the enzyme immobilization process [23]. The K_m^{app} of the CAH/CHIT-*g*-PANI/ITO bioelectrode is much less than that of these previously reported biosensors (typically 2 to 7 mM). The small K_m^{app} value indicates a high affinity of CAH to the CHIT-*g*-PANI matrix over the electrode surface, which may be attributed to 1) the advantageous $-NH_2$ functionalized surface of the CHIT-*g*-PANI matrix for the enzyme immobilization that can favor conformational changes of the enzyme, and 2) the high positive electrostatic interaction, which can help to effectively immobilize CAH onto the CHIT-*g*-PANI/ITO electrode.

3.3. Photometric study

A photometric study was performed to calculate the apparent enzyme activity of the CAH enzyme. CAH catalyzes the hydrolysis of creatinine (II) to produce sarcosine (III) and urea (IV). In the presence of urease, urea further hydrolyzed into ammonia, which in turn reacts with the Nessler's reagent ($K_2\ Hg_2\ I_4$) to form a colored product, $NH_2Hg_2I_3$ (Figure 6). Through taking the absorbance of $NH_2Hg_2I_3$ at 385 nm, apparent enzyme activity of the CAH enzyme can be determined [24]. The apparent enzyme activity (${}^{enz}a_{app}$) was calculated using Equation (2):

$$ {}^{enz}a_{app} = \frac{AV}{\varepsilon ts} \qquad (2) $$

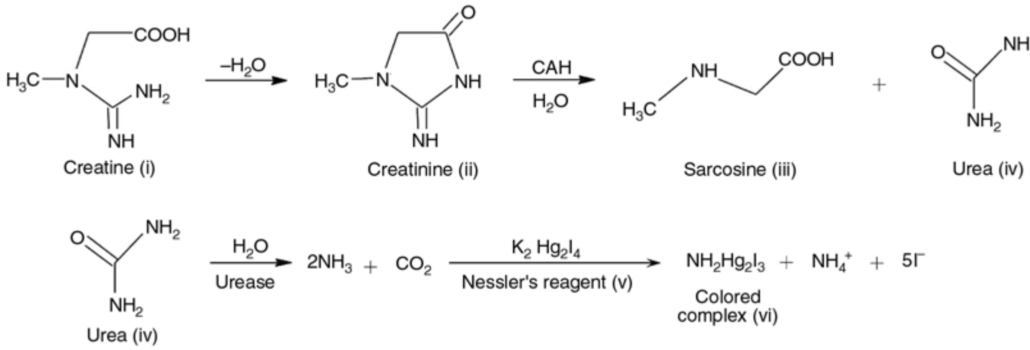

Figure 6. Production of photomerically active $NH_2Hg_2I_3$ as a sensing element resulting from the reaction of Nessler's reagent and librated NH_3 (i.e., obtained from enzymatic hydrolysis of creatinine)

where *A* is the difference in absorbance before and after incubation, *V* is the total volume of the solution, ε is the millimolar extinction coefficient, *t* is the reaction time and *s* is the surface area of the electrode. The apparent enzyme activity was calculated to be 83.59 mg/cm^2; indicating 83.59 mg of CAH was actively immobilized per unit area of CHIT-*g*-PANI matrix.

3.4. Effect of pH, temperature and time

The peak current varied with the value of pH in the range 6.0–8.0; the optimum current is obtained at pH 7.0. It suggests that optimum CAH enzyme activity is found at pH 7.0. The thermal stability of the CAH/CHIT-*g*-PANI/ITO bioelectrode was studied by measuring the current at different temperatures ranging from 25 to 45°C in the presence of creatinine 150 µM and a phosphate buffer (50 mM, pH 7.0). It was observed that the reaction rate increased with the temperature up to 32°C and the optimum temperature range was between 30–32°C due to the increased kinetic energy of the reacting molecules. The storage stability of the CAH/CHIT-*g*-PANI/ITO electrode was amperometrically measured and a similar current response was found after it was stored for ~300 days at 4°C. Hence, the CAH/CHIT-*g*-PANI/ITO bioelectrode exhibited an excellent operational and storage stability.

4. Conclusions

Creatine amidinohydrolase was covalently immobilized onto the CHIT-*g*-PANI graft copolymer matrix. The relatively low Michaelis-Menten constant of 0.51 mM indicates that the CHIT-*g*-PANI matrix had a high affinity for the CAH enzyme. The enzyme holding capacity of graft copolymer matrix was determined to be 83.59 mg/cm^2 and was affected by pH, temperature, and time. Present efforts aim to use CAH/CHIT-*g*-PANI/ITO bioelectrodes with a good shelf life to fabricate an efficient creatinine biosensor that can detect creatinine from the blood and urine.

Acknowledgements

The authors are thankful to the Department of Science and Technology, Govt. of India for generous financial support and to the Director, National Physical Laboratory, New Delhi, India for providing infrastructure facilities to carry out this work.

References

[1] Burtis C. A., Ashwood E. R.: Tietz textbook of clinical chemistry. Saunders, Philadelphia (1986).
[2] Sena S. F., Syed D., McComb R. B.: Effect of high creatine content on the Kodak single-slide method for creatinine. Clinical Chemistry, **34**, 594–595 (1988).
[3] Tsuchida T., Yoda K.: Multi-enzyme membrane electrodes for determination of creatinine and creatine in serum. Clinical Chemistry, **29**, 51–55 (1983).
[4] Winquist F., Lundstrom I.: Determination of creatinine by an ammonia-sensitive semiconductor structure and immobilized enzymes. Analytical Chemistry, **58**, 145–148 (1986). DOI: 10.1021/ac00292a035
[5] Yamato H., Ohwa M., Wernet W.: A polypyrrole/three-enzyme electrode for creatinine detection. Analytical Chemistry, **67**, 2776–2780 (1995). DOI: 10.1021/ac00113a009
[6] Koncki R.: Recent developments in potentiometric biosensors for biomedical analysis. Analytica Chimica Acta, **599**, 7–15 (2007). DOI: 10.1016/j.aca.2007.08.003
[7] Koncki R., Walcerz I., Ruckruh F., Glab S.: Bienzymatic potentiometric electrodes for creatine and L-arginine determination. Analytica Chimica Acta, **333**, 215–222 (1996). DOI: 10.1016/0003-2670(96)00266-8
[8] Kubo I., Karube I., Suzuki S.: Amperometric determination of creatinine with a biosensor based on immobilized creatininase and nitrifying bacteria. Analytica Chimica Acta, **151**, 371–376 (1983). DOI: 10.1016/S0003-2670(00)80098-7
[9] Schumann J., Möllering H., Jaenicke R.: Intrinsic stability and extrinsic stabilization of creatinase from *Pseudomonas putida*. Biological Chemistry Hoppev-Seyler, **374**, 427–434 (1993).
[10] Schumann J., Böhm G., Jaenicke R., Schumacher G., Rudolph R.: Stabilization of creatinase from *Pseudomonas putida* by random mutagenesis. Protein Science, **2**, 1612–1620 (1993). DOI: 10.1002/pro.5560021007
[11] Tiwari A., Gong S.: Electrochemical study of chitosan-SiO$_2$-MWNT composite electrodes for the fabrication of cholesterol biosensors. Electroanalysis, **20**, 2119–2126 (2008). DOI: 10.1002/elan.200804296

[12] Berberich J. A., Yang L. W., Bahar I., Russell A. J.: A stable three enzyme creatinine biosensor. 2. Analysis of the impact of silver ions on creatine amidinohydrolase. Acta Biomaterialia, **1**, 183–191 (2005). DOI: 10.1016/j.actbio.2004.11.007

[13] Tiwari A.: Gum arabic-graft-polyaniline: An electrically active redox biomaterial for sensor applications. Journal of Macromolecular Science Part A: Pure and Applied Chemistry, **44**, 735–745 (2007). DOI: 10.1080/10601320701353116

[14] Tiwari A., Gong S.: Electrochemical detection of a breast cancer susceptible gene using cDNA immobilized chitosan-co-polyaniline electrode. Talanta, **77**, 1217–1222 (2009). DOI: 10.1016/j.talanta.2008.08.029

[15] Tiwari A., Gong S.: Electrochemical synthesis of chitosan-co-polyaniline/$WO_3 \cdot nH_2O$ composite electrode for amperometric detection of NO_2 gas. Electroanalysis, **20**, 1775–1781 (2008). DOI: 10.1002/elan.200804237

[16] Tiwari A., Singh V.: Synthesis and characterization of electrical conducting chitosan-graft-polyaniline. Express Polymer Letters, **1**, 308–317 (2007). DOI: 10.3144/expresspolymlett.2007.44

[17] Tiwari A., Sen V., Dhakate S. R., Mishra A. P., Singh V.: Synthesis, characterization and hoping transport properties of HCl doped conducting biopolymer-*co*-polyaniline zwitterion hybrids. Polymers for Advanced Technology, **19**, 909–914 (2008). DOI: 10.1002/pat.1058

[18] Tiwari A., Singh V.: Microwave-induced synthesis of electrical conducting gum acacia-*graft*-polyaniline. Carbohydrate Polymers, **74**, 427–434 (2008). DOI: 10.1016/j.carbpol.2008.03.015

[19] Tiwari A.: Synthesis and characterization of pH switching electrical conducting biopolymer hybrids for sensor applications. Journal of Polymer Research, **15**, 337–342, (2008). DOI: 10.1007/s10965-008-9176-4

[20] Solanki P. R., Kausik A. K., Ahamad A. A., Tiwari A., Malhotra B. D.: Multi-walled carbon nanotubes/sol-gel derived silica/chitosan nanobiocomposite for total cholesterol sensor. Sensors and Actuators B: Chemical, **137**, 727–735 (2009). DOI: 10.1016/j.snb.2008.12.044

[21] Abbasian A., Ghaffarian S. R., Mohammadi N., Fallahi D.: The contact angle of thin-uncured epoxy films: Thickness effect. Colloids and Surfaces A: Physicochemical and Engineering Aspects, **236**, 133–140 (2004). DOI: 10.1016/j.colsurfa.2004.01.028

[22] Wilson K., Walker J. M.: Principles, techniques of practical biochemistry. Cambridge University Press, New York (2000).

[23] Kouassi G. K., Irudayaraj J., McCarty G.: Examination of cholesterol oxidase attachment to magnetic nanoparticles. Journal of Nanobiotechnology, **3**, 1–9 (2005). DOI: 10.1186/1477-3155-3-1

[24] Rajesh, Bisht V., Takashima W., Kaneto K.: An amperometric urea biosensor based on covalent immobilization of urease onto an electrochemically prepared copolymer poly (*N*-3-aminopropyl pyrrole-co-pyrrole) film. Biomaterials, **26**, 3683–3690 (2005). DOI: 10.1016/j.biomaterials.2004.09.024

eXPRESS Polymer Letters Vol.3, No.9 (2009) 560–568
Available online at www.expresspolymlett.com
DOI: 10.3144/expresspolymlett.2009.70

An experimental study on mechanical properties of GFRP braid-pultruded composite rods

M. S. Ahmadi[1], *M. S. Johari*[1*], *M. Sadighi*[2], *M. Esfandeh*[3]

[1]Textile Engineering Department, Amirkabir University of Technology, Tehran, Iran
[2]Mechanical Engineering Department, Amirkabir University of Technology, Tehran, Iran
[3]Composites Group, Iran Polymer & Petrochemical Institute, Tehran, Iran

Received 19 April 2009; accepted in revised form 15 June 2009

Abstract. In this work, a conventional textile braiding machine was modified and added to a pultrusion line in order to produce glass fiber reinforced composite rods by braiding-pultrusion technique. Braid-pultruded (BP) rods were produced with three braid roving linear densities and also with three different braid angles. To study the influence of overbraiding on mechanical properties of pultruded rods, unidirectional (UD) rods, without braided fabric, were produced, as well. All rod types were subjected to tensile, bending and torsion tests. The experimental results showed that BP rods have considerably higher shear modulus, but lower tensile modulus and flexural rigidity than those of UD pultruded rods, when fiber volume fraction is kept constant. Moreover, rods produced with higher braid roving linear densities had better torsional, but lower tensile and flexural properties. The highest shear modulus was observed in BP rods with braid angle of 45°.

Keywords: *polymer composites, mechanical properties, braiding, pultrusion, rod*

1. Introduction

Braiding has traditionally been used for producing textile structures such as shoelaces and ropes. However, in recent years, fiber reinforced composites and medical implants have become interesting application areas for braiding. As a technique for manufacturing preforms for composite structures, braiding has been attracting a great deal of attention. Composite structures reinforced with braided fabrics have a number of advantages over other competing structures such as woven and filament wound composites, as follows. Braided composites have superior toughness and fatigue strength in comparison to filament wound composites. In filament wound composites, cracks propagate readily along the fibers while points of interlacement in braided composites act as crack arresters [1, 2]. Woven fabrics have orthogonal interlacement while the braids can be constructed over a wide range of angles, from 10 to 85°. An additional set of axial yarns can be introduced to the braiding process to produce triaxial braids; triaxial braids are more stable and exhibit nearly isotropic properties [1, 3, 4]. Braids can be produced either as seamless tubes or flat fabrics with a continuous selvedge. Composites produced with the braided fabrics exhibit superior strength and crack resistance in comparison to broadcloth composites, due to fiber continuity [1].

Braided composites have good shear and torsional strength and stiffness. They also offer increased transverse moduli, transverse strength, damage tolerance, dimensional stability and near net shape manufacturing capabilities [5–9].

Braiding can also be integrated with the pultrusion process, which is a well-known method for manu-

---

[*]Corresponding author, e-mail: mjohari@aut.ac.ir

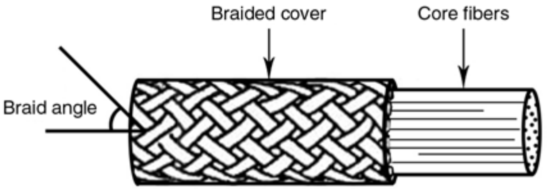

Figure 1. Structure of a BP rod

facturing composite parts in a continuous way. A number of researchers worked on various aspects of braiding-pultrusion process and recommended it as a new low-cost and efficient fabrication technique [10–16].

A simple product of the braiding-pultrusion technique is a braid-pultruded (BP) cylindrical rod which is comprised of a braided cover and a core of unidirectional fibers (Figure 1). Some of the applications and unique features of this kind of rods were investigated in various works [13, 17–19]. However, there are a few works investigating mechanical properties of BP rods. Saito *et al.* [20] and Hamada *et al.* [21] investigated the properties of BP rods under crush test and showed that these rods had superior properties in comparison to the unidirectional rods in terms of energy absorption capabilities. They came to the conclusion that when BP rods are subjected to compressive loads, the braided layer protects the unidirectional core fibers against axial splitting and consequently makes the structure absorb more energy before failure. Hiermer *et al.* [22] investigated the torsional failure behaviour of cylindrical carbon/epoxy implant rods, which were structurally similar to BP rods. They manufactured the specimens in a manual multi-stage process, in which, first the cylindrical rods were produced from carbon/epoxy plates by means of cutting and grinding, then over-wound with a layer of braided fabric. They showed that the torsional properties of the rods with braided fabric were much better than those without braided fabric. Nevertheless, as in some applications known for BP rods, such as rebars or medical implants, they can be subjected to different types of loading, like tension, torsion and bending [19, 22], a comprehensive study on their mechanical behavior under such loading types seems to be of great importance.

Therefore, the aim of this paper is to compare tensile, torsional and flexural properties of GFRP (glass fiber reinforced polymer) braid-pultruded rods to those of their UD counterparts and also to study the effect of some parameters such as braid angle and braid yarn linear density on mechanical properties of BP rods.

2. Development of a braiding-pultrusion line

The combination of braiding and pultrusion processes has been also named pull-braiding, braided-pultrusion and braidtrusion in different works. For setting up the braiding-pultrusion production line in the current work, a conventional textile braiding machine was modified at Textile Engineering Department of Amirkabir University of Technology and added to a pultrusion production line at Iran Polymer & Petrochemical Institute. A schematic of braiding-pultrusion production arrangement used in the present work is shown in Figure 2. Roving strands are unwound from the bobbins held in the creel and pass through an alignment card. The card prevents twisting of the rovings together and at the same time prepares the core part of the braid-pultruded structure which is unidirectional. Once all the fibers are aligned, they are passed through a resin bath. To make sure the fibers

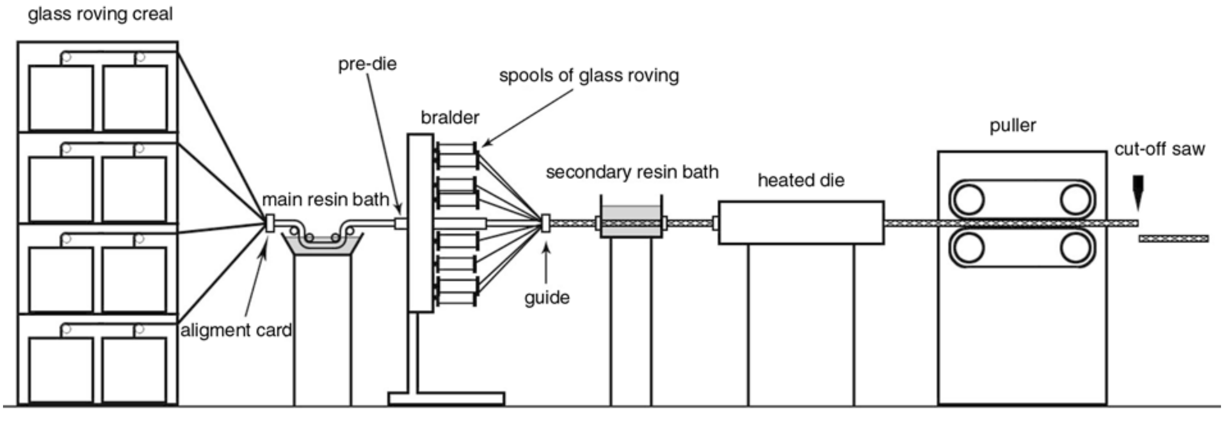

Figure 2. Arrangement of the braiding-pultrusion process used in the present work

are fully wetted, the strands are passed through a series of rollers, which flatten and spread out the individual roving. The resin used is normally of good and rapid impregnation properties with long gel-time and short curing time. Following the resin bath, the unidirectional fibers are over-braided using the braiding machine.

To be combined with the pultrusion line, in this work, a traditional textile braider was changed from vertical to horizontal configuration and equipped with specially designed spools suitable for winding glass roving. Braid angle, which is the angle between braid yarns and axis of the braid structure and is one of the most important structural parameters affecting mechanical properties of braids (Figure 1), is calculated from Equation (1) [1]:

$$\alpha = \tan^{-1}\left(\frac{\omega \cdot R}{v}\right) \qquad (1)$$

where α denotes braid angle, ω average angular velocity of spools around the braider center point, R the core material radius and v take-up speed of the braid.

Changing the braid angle in braiding machines is usually performed by changing the take-up speed. However, in the combination of braiding and pultrusion processes, as all production stages, i.e. resin impregnating, braiding and curing are carried out continuously, any change in take-up rate leads to change in curing time. Hence, in the present work, to change the braid angle, angular velocity of spools around the center of the braider was changed. For this purpose, the braider was equipped with a frequency controlled motor for the spools drive. As a result, all rod types could be produced with the same curing speed, and it was also possible to easily change the braid angle during the process. Moreover, a pre-die was embedded in the center of the braider. The pre-die bundles the unidirectional core fibers together and gives them a circular cross section before being dressed by the braided cover.

Wetting the braid yarns with resin can be done in several ways. Using a resin curtain and injecting resin by a resin pump are among them which can be found in various works [13, 15, 19, 20, 23]. In this work, a secondary resin bath was designed and installed after the braider in order to ensure a perfect wetting of braid yarns, though the excess resin of core fibers in some types with relatively low cover/core fiber weight ratio was almost enough to wet out the braid fibers as they wrapped around them under tension.

After the secondary resin bath, the structure is guided into the heated die at one end and exiting at the other as a cured structural component. The die was 500 mm in length, 6 mm in diameter, and with curing temperature of 120°C. The pulling station is located at the end of the braiding-pultrusion line. A set of padded clamps grip the cross-section and horizontally pull the rod. For the current work, pultrusion was carried out with the speed of 100 mm/min. The final process in the braided pultrusion technique is the cut-off that is done by the cut-off saw located immediately after the pulling station.

3. Material and manufacture of rods

The glass fiber roving used for manufacturing the rods was supplied by CPIC Inc. with the designation ER-469L. The matrix material was unsaturated isophthalic polyester resin with the designation 751129 by Bushehr Chemical Industries Co. Benzoyl peroxide (BPO) supplied by Merck Chemical Co. was used as curing initiator at 3 phr. Release agent of PAT-654/M by CRC Co. was also used in resin formulation at 1 phr. Fiber and resin properties are listed in Table 1.

In this study, rods with diameter of 6±0.1 mm were produced by braiding-pultrusion method. For all rod types, braiding process was carried out using 8 spools of glass roving and with the diamond pattern (1/1 repeat).

For investigating the effect of braid roving linear density, three types of rods were produced using three linear densities of roving; 300, 600 and 900 tex as braided cover roving. The braid angle was kept 45° in these types. To study the influence of braid angle on the mechanical properties, rods with two other braid angles, i.e. 30 and 55° were also produced. Moreover, unidirectional rods were pultruded without using braid fibers to investigate the effect of overbraiding.

Table 1. Fiber and resin properties

Material specification	Tensile strength [MPa]	Tensile modulus [GPa]	Density [g/cm^3]
Glass fiber, ER-469L	1700	73	2.5
Unsaturated Isophthalic Polyester resin, 751129	55	4	1.1

Table 2. Specifications of manufactured rods

Rod type	Linear density of braid roving [tex]	Linear density of core fibers [tex]	Braid angle [°]	Fiber volume fraction [%]	Cover/core fiber weight ratio [%]
300-45	(300×8)	(2400×18) + 1500	45	63.1	7.7
600-45	(600×8)	(2400×17) + 300	45	63.5	13.7
900-45	(900×8)	(2400×15) + 1800	45	63.4	26.9
900-30	(900×8)	(2400×16) + 1200	30	63.1	21.5
900-55	(900×8)	(2400×14)	55	61.4	40.8
UD	–	(2400×20)	–	60.6	0.0

All rods were produced with almost the same fiber volume fraction. Therefore, it was necessary to use the same amount of fibers in the unit length of each rod. Since the amount of fibers in the braided cover changes when braid angle and/or braid yarn linear density change, the total weight of fibers in the unit length of each rod was kept the same by changing the amount of core fibers. After manufacturing the rods, some specimens were prepared for burn-off test in order to measure the actual value of fiber volume fraction. Burn-off test was conducted at 600°C for 90 minutes. Cover/core fiber weight ratio was also measured on the specimens after burn-off test by separating braided cover from core and weighing them. The specifications of manufactured rods are listed in Table 2.

The produced rods had good surface quality and accurate dimensions. The results of torsion and bending tests showed there was a good bond between braided cover and unidirectional core. Figure 3 shows some of the manufactured rods (a), and a specimen after burn-off test (b).

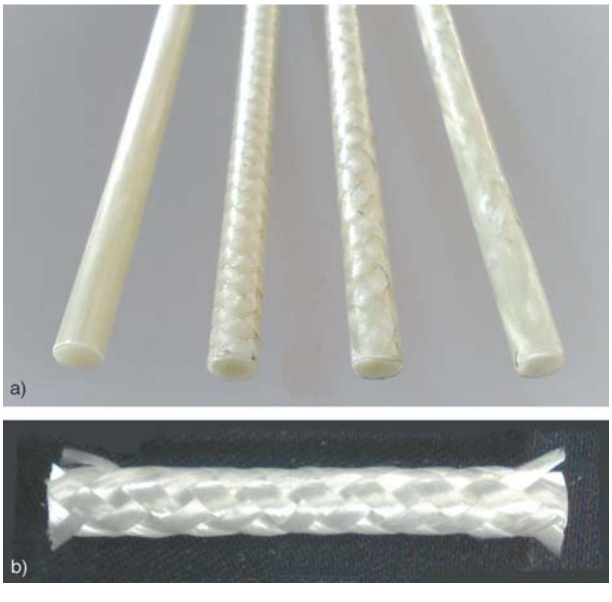

Figure 3. (a) Some manufactured rods and (b) a specimen after burn-off test

4. Test equipment and procedure

4.1. Torsion test

For preparation of torsion test specimens, rods were cut into pieces of 120 mm length. All pieces were embedded at the two ends in specially designed steel pipes with epoxy resin. Inner diameter of steel pipes was designed to be 6.2 mm in order to make sure the rods are aligned in the center of both pipes. To ensure that the rods will not twist in the pipes under torsional load, one steel pin was used at each end (Figure 4). Four specimens were prepared from each type for torsion test.

The specimens were tested by torsion tester machine STS-50, which was developed by Santam Engineering Design Co. (Figure 5). Twisting the specimens was carried out manually, and the torque associated with each twist angle was shown digitally on the machine. The torque-angle curve was plotted for each rod type using the measured data. In order to analyze shear performance of rods, their shear modulus was calculated (Equations (2) and (3)). For cylindrical rods subjected to torsional loads:

Figure 4. Photograph of a torsion test specimen

Figure 5. Torsion tester machine

$$G = \frac{TL}{J\theta} \quad (2)$$

$$J = \frac{\pi D^4}{32} \quad (3)$$

where G denotes shear modulus of elasticity, T torsional torque, J polar inertia moment for circular cross sectional area, θ angle of twist, L length and D diameter of the rod.

Based on Equations (2) and (3), shear modulus of elasticity was calculated for each rod type.

4.2. Tensile test

For measuring tensile modulus of produced rods, three specimens were prepared from each type for tensile test. Rods were cut into pieces of 450 mm. Two ends of all specimens were threaded using a soft file and then filament wound with glass fiber and epoxy resin. To achieve this, sufficient length of glass roving was impregnated with epoxy resin and wound around 100 mm length of each end of the specimens, until it reached the diameter of about 15 mm. After curing, the ends were ground and polished in order to reach uniform cylindrical shapes. Three specimens were prepared from each type for tensile test.

The specimens were then tested by the universal testing machine STM-150 made by Santam Engineering Design Co., using an extensometer and with cross head speed of 5 mm/min. Stress-strain data series were measured and tensile modulus was calculated for each specimen. Figure 6 shows a specimen during tensile test.

Figure 6. A specimen during tensile test

Figure 7. A specimen under bending test

4.3. Bending test

Three point bending test was also carried out by the universal testing machine STM-150 (Figure 7). The specimens were supported over a span of 120 mm. However, they were made of longer length in order to ensure they do not slip from the supports. Four specimens from each type were tested with loading rate of 5 mm/min. The bending loads versus deflections were measured until failure and then flexural rigidity values of all specimens were calculated. For components subjected to flexural load, flexural rigidity can be computed using Equation (4):

$$EI = \frac{PL^3}{48\delta} \quad (4)$$

where EI is flexural rigidity, in which E and I are modulus of elasticity and the second moment of inertia of the beam section, respectively, P is concentrated load acting on a simply supported beam, L is the beam span length and δ is deflection.

5. Results and discussion

Using the data measured in the torsion test, torque-angle curves for all rod types were plotted (Figures 8 and 9). From these figures some phenomena

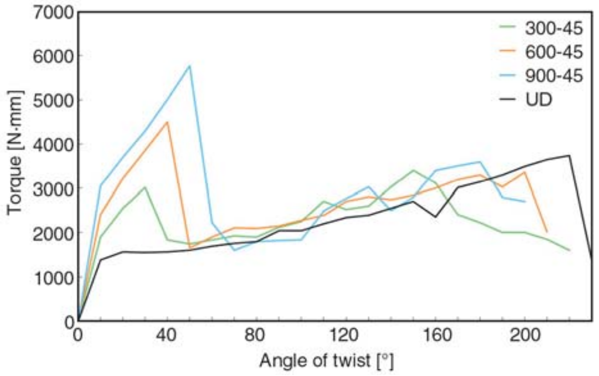

Figure 8. Torque-angle curves of the types 300-45, 600-45, 900-45 and UD

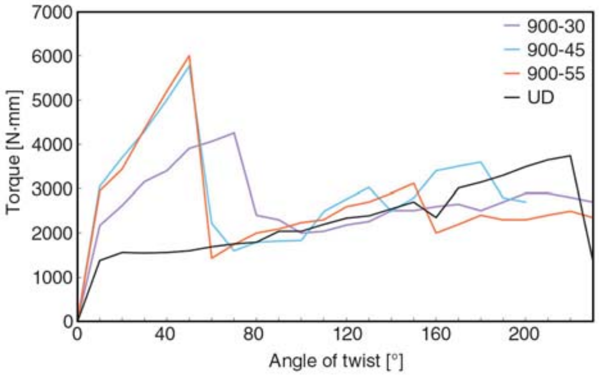

Figure 9. Torque-angle curves of the types 900-30, 900-45, 900-55 and UD

can be well identified. Regarding BP rods, it was observed that they had linear torque-angle behavior with no fiber breakage in the beginning of the test. Afterward, fibers in the braided cover started to break gradually. Torque increased with braid angle quasi-linearly, but with a lower slope, in this region until complete failure of braided cover, where torque value collapsed suddenly. At this point the interface between braided cover and UD core was debonded, causing the shear strength to diminish dramatically. This pattern can be seen for all BP rod types.

Considering torque-angle curves of the types 300-45, 600-45 and 900-45 in Figure 8, and also the average calculated shear modulus of the rods which is shown in Figure 10, one can find out that as the braid roving linear density increases, the braid cover fails at higher torques and higher angles. It can also be seen that shear modulus is higher in rods with higher braid roving linear densities.

It may also be noted from the properties of types 900-30, 900-45 and 900-55 that the rods with braid angle of 45° have the highest shear modulus and torsional stiffness, which is expected from the theory of composite structures. However, the highest braid cover failure torque was observed in 900-55. It may be because of some manufacturing faults during production or test specimens preparation in the case of 900-45. In fact, the rods with braid angle of 45° were more subjected to fiber misalignment as the impregnated structure entered the die.

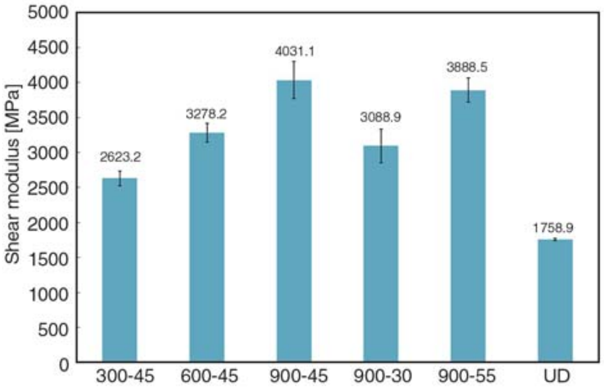

Figure 10. Average shear modulus of the rods

Comparing the torque-angle curve of UD rod to those of braid-pultruded ones (Figures 8 and 9), one can obviously see how overbraiding changes the torsional behavior of rods. The UD rods show an elastic behavior in the beginning and then a combination of such failure mechanisms as matrix cracking and fiber breakage causes the curve to continue with a little increase in applied torque according to the angle. It can be observed that shear modulus of UD rod is the lowest values among those of all BP ones. It is interesting that in type 300-45, with the lowest braid/core fiber weight ratio, i.e. 0.77, shear modulus is about 1.5 times higher than that for UD rod.

Although there are a few works investigating the properties of BP rods, comparing the experimental results to those of similar braided structures in the literature shows good agreements [22, 25, 26].

Results from tensile and bending tests showed all rods had linear behavior in tension and flexure. Figures 11 and 12 show average values of elastic modulus and flexural rigidity of the rods, respectively. It is clear that UD rods have the highest elastic modulus and flexural rigidity, which is expected, as they have the highest amount of axially oriented fibers in their structures.

Regarding BP rods, it can be seen that as the braid roving linear density increases, elastic modulus and flexural rigidity fall down. It is due to the fact that

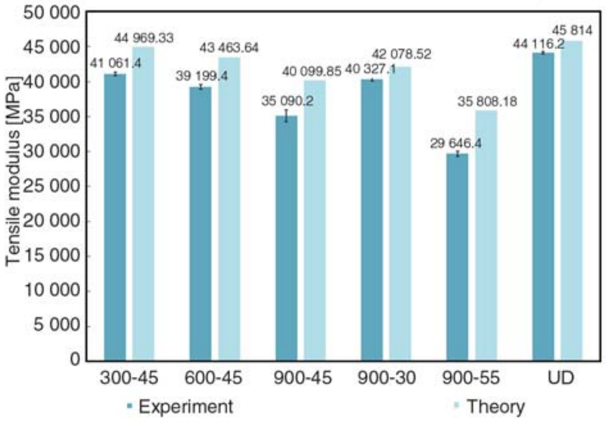

Figure 11. Average experimental tensile modulus of the rods and the theoretical model predictions

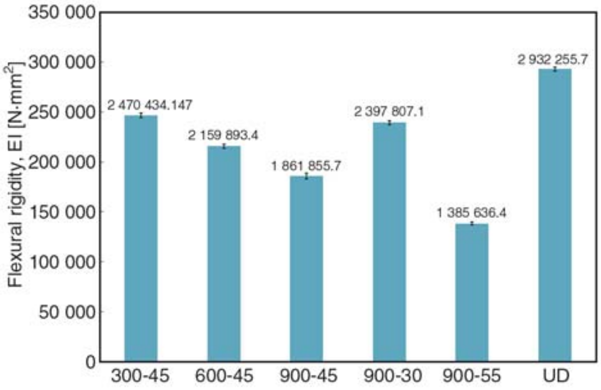

Figure 12. Average flexural rigidity of the rods

all rods were produced with the same fiber volume fraction and therefore, rods with higher braid roving linear density had more amount of radial fibers and less amount of axial core fibers in their structures.

Comparing properties of the types 900-30, 900-45 and 900-55 shows that both elastic modulus and flexural rigidity are higher in samples with lower braid angles, which is due to two reasons. First, decreasing braid angle leads to more contribution of braided cover fibers in resisting axial loads. Second, in samples with lower braid angles, the amount of axial fibers is higher when all rods are to be produced with the same fiber volume fraction.

A simple theoretical model was also utilized to predict the tensile moduli of the rods and compare them to experimental findings. In the model, the structure was assumed to be comprised of two main parts; braided cover and UD core. Tensile moduli were calculated for both parts according to basic formulas of micromechanics, and then were used to calculate the tensile modulus of the whole structure based on the averaging technique [24]. The braided cover was assumed a [±θ] laminate. Therefore, fiber undulation was neglected in this model. The comparison between experimental tensile moduli and model prediction is shown in Figure 11. Relatively good agreement between the model prediction and the test results can be observed. It can be seen that the model over-predicts the tensile moduli for all types. The main reason for this phenomenon is that fiber undulation is not taken into account in the model.

Moreover, tensile experimental results were in good agreement with those of similar braided structures in the literature [19, 27, 28]. Similar reports on the bending behavior were also observed in some research works [25, 26].

All in all, overbraiding the unidirectional core in pultruded rods, leads to a considerable improvement in their shear modulus and at the same time, a drop in their tensile and flexural properties compared to their UD pultruded counterparts with the same fiber volume fraction and diameter. Comparing the results shows a 56.4% improvement in shear modulus, a 20.4% drop in elastic modulus and a 36.5% drop in flexural rigidity in the type 900-45 compared to UD rod. However, it is a matter of design priorities to find optimum values for braid roving linear density and braid angle in order to achieve desirable torsional properties and at the same time, keep tensile and flexural properties at an acceptable level.

6. Conclusions

In this work a braiding-pultrusion production line was developed by modifying a conventional textile braiding machine and adding it to a pultrusion line for production of braid-pultruded (BP) composite rods. With this method it was possible to produce rods with a reinforcement structure comprised of a braided fabric cover and unidirectional core fibers. In order to evaluate mechanical properties of BP rods and study the effect of some braiding parameters, they were produced with different braid roving linear densities and braid angles. The results were also compared to those of unidirectional (UD) pultruded rods which were produced without braided fabric cover, but with the same fiber volume fraction and diameter.

Overbraiding was proved to have a great effect in improving shear performance of pultruded rods. BP rods had higher shear modulus compared to UD pultruded rods. Even with the lowest cover/core fiber weight ratio, shear modulus was about 1.5 times higher than that for UD rod. Nevertheless, tensile elastic modulus and flexural rigidity were lower in BP rods compared to UD ones when fiber volume fraction is kept constant.

It was also concluded that increasing the braid roving linear density leads to an improvement in shear modulus, but a reduction in tensile modulus and flexural rigidity.

Moreover, the rod with braid angle of 45° had higher shear modulus compared to those with braid angles of 30 and 55°. Tensile modulus and flexural rigidity were higher in BP rods with lower braid angles.

References

[1] Potluri P., Rawal A., Rivaldi M., Porat I.: Geometrical modelling and control of a triaxial braiding machine for producing 3D performs. Composites Part A: Applied Science and Manufacturing, **34**, 481–492 (2003).
DOI: 10.1016/S1359-835X(03)00061-7

[2] Munro M., Fahim A.: Comparison of helical filament winding and 2D braiding of fiber reinforced polymeric components. Materials and Manufacturing Processes, **10**, 37–46 (1995).
DOI: 10.1080/10426919508936925

[3] Savino V., Chou T-W.: Mechanical characterization of triaxially braided hybrid composites. Polymer Composites, **19**, 473–486 (1998).
DOI: 10.1002/pc.10122

[4] Dadkah M. S., Flintoff J. G., Cox B. N.: Simple models for triaxially braided composites. Composites, **26**, 561–577 (1995).
DOI: 10.1016/0010-4361(95)92621-I

[5] Byun J. H., Chou T-W.: Modelling and characterization of textile structural composites – A review. Journal of Strain Analysis for Engineering Design, **24**, 253–262 (1989).
DOI: 10.1243/03093247V244253

[6] Hufenbach W., Bla ejewski W., Kroll L., Böhm R., Gude M., Czulak A.: Manufacture and multiaxial test of composite tube specimens with braided glass fiber reinforcement. Journal of Materials Processing Technology, **162–163**, 65–70 (2005).
DOI: 10.1016/j.jmatprotec.2005.02.212

[7] Charlebois K. M., Boukhili R., Zebdi O., Trochu F., Gasmi A.: Evaluation of the physical and mechanical properties of braided fabrics and their composites. Journal of Reinforced Plastics and Composites, **24**, 1539–1554 (2005).
DOI: 10.1177/0731684405050391

[8] Falzon P. J., Herszberg I.: Mechanical performance of 2-D braided carbon/epoxy composites. Composites Science and Technology, **58**, 253–265 (1998).
DOI: 10.1016/S0266-3538(97)00133-4

[9] Kessels J. F. A., Akkerman R.: Prediction of the yarn trajectories on complex braided preforms. Composites Part A: Applied Science and Manufacturing, **33**, 1073–1081 (2002).
DOI: 10.1016/S1359-835X(02)00075-1

[10] Bechtold G., Kameo K., Friedrich K., Hamada H.: Pullbraiding of commingled GF/PP yarn- Influence of processing parameters. in 'The 4th International Symposium for Textile Composites. Kyoto, Japan' O28/1–O28/5 (1998).

[11] Fujita A., Nakatani T., Uozumi T., Kameo K., Nakai A., Hamada H.: Crush energy absorption of braided composite rods. in 'The Fifth Japan International SAMPE Symposium. Tokyo, Japan' 1231–1234 (1997).

[12] Hamada H., Ramakrishna S.: Impact performance of glass cloth/epoxy composite tubes with different surface treatment. Composite Interfaces, **4**, 35–44 (1996).
DOI: 10.1163/156855496X00137

[13] Lam H., Ko F. K.: Composite manufacturing by braidtrusion process. in 'The International SAMPE Technical Conference. Seattle, USA', Vol 33, 532–539 (2001).

[14] Michaeli W., Jürss D.: Thermoplastic pull-braiding: Pultrusion of profiles with braided fibre lay-up and thermoplastic matrix system. Composites Part A: Applied Science and Manufacturing, **27**, 3–7 (1996).
DOI: 10.1016/1359-835X(95)00004-L

[15] Milwich M., Linti C., Plank H.: Production of fiber reinforced plastic profiles by braid pultrusion. Band- und Flechtindustrie, **38**, 42–47 (2001).

[16] Uozomi T., Hisa Y., Fujita A., Hamada H., Nakai A., Yokoyama A.: Braiding pultrusion process (BPP). in 'The International SAMPE Technical Conference, Covina, USA', 27, 371–379 (1995).

[17] Boss J. N., Ganesh V. K.: Fabrication and properties of graded composite rods for biomedical applications. Composite Structures, **73**, 289–293 (2006).
DOI: 10.1016/j.compstruct.2005.04.030

[18] Hampton F. P., Lam H., Ko F. K., Harris H. G.: Design methodology of a ductile hybrid FRP for concrete structures by the braidtrusion process. in 'The International SAMPE Symposium and Exhibition. California, USA', Vol 46(II), 2421–2432 (2001).

[19] Harris H. G., Somboonsong W., Ko F. K.: New ductile hybrid FRP reinforcing bar for concrete structures. Journal of Composites for Construction, **2**, 28–37 (1998).
DOI: 10.1061/(ASCE)1090-0268(1998)2:1(28)

[20] Saito H., Chirwa E. C., Inai R., Hamada H.: Energy absorption of braiding pultrusion process composite rods. Composite Structures, **55**, 407–417 (2002).
DOI: 10.1016/S0263-8223(01)00160-X

[21] Hamada H., Kameo K., Sakaguchi M., Saito H., Iwamoto M.: Energy-absorption properties of braided composite rods. Composites Science and Technology, **60**, 723–729 (2000).
DOI: 10.1016/S0266-3538(99)00182-7

[22] Hiermer T., Schmitt-Thomas Kh. G., Yang Z-G.: Mechanical properties and failure behavior of cylindrical CFRP-implant-rods under torsion load. Composites Part A: Applied Science and Manufacturing, **29**, 1453–1461 (1998).
DOI: 10.1016/S1359-835X(98)00027-X

[23] Kruesi A. H., Hasko G. H.: Computer controlled resin impregnation for fiber composite braiding. in 'The International SAMPE Symposium and Exhibition. California, USA', Vol 32, 309–317 (1987).

[24] Kregers A. F., Teters G. A.: Use of averaging methods to determine the viscoelastic properties of spacially reinforced composites. Mechanics of Composite Materials, **15**, 377–383 (1979).
DOI: 10.1007/BF00605861

[25] Potluri P., Manan A.: Mechanics of non-orthogonally interlaced textile composites. Composites Part A: Applied Science and Manufacturing, **38**, 1216–1226 (2007).
DOI: 10.1016/j.compositesa.2006.04.008

[26] Potluri P., Manan A., Francke M., Day R. J.: Flexural and torsional behaviour of biaxial and triaxial braided composite structures. Composite Structures, **75**, 377–386 (2006).
DOI: 10.1016/j.compstruct.2006.04.046

[27] Huang Z-M.: Efficient approach to the structure-property relationship of woven and braided fabric-reinforced composites up to failure. Journal of Reinforced Plastics and Composites, **24**, 1289–1309 (2005).
DOI: 10.1177/0731684405049860

[28] Zywicz E., Nguyen T.: On the flexural and extensional behavior of a large-tow triaxial braided composite. Composites Science and Technology, **60**, 2989–2999 (2000).
DOI: 10.1016/S0266-3538(00)00158-5

eXPRESS Polymer Letters Vol.3, No.9 (2009) 569–578
Available online at www.expresspolymlett.com
DOI: 10.3144/expresspolymlett.2009.71

Characterization of extrusion flow using particle image velocimetry

*J. E. Fournier, M. F. Lacrampe**, *P. Krawczak*

Ecole des Mines de Douai, Department of Polymers and Composites Technology & Mechanical Engineering, 941 rue Charles Bourseul, BP 10838, 59508, Douai, France

Received 29 May 2009; accepted in revised form 24 June 2009

Abstract. The aim of this study was the characterization of polymer flows within an extrusion die using particle image velocimetry (PIV) in very constraining conditions (high temperature, pressure and velocity). Measurements were realized on semi-industrial equipments in order to have test conditions close to the industrial ones. Simple flows as well as disrupted ones were studied in order to determine the capabilities and the limits of the method. The analysis of the velocity profiles pointed out significant wall slip, which was confirmed by rheological measurements based on Mooney's method. Numerical simulations were used to connect the two sets of measurements and to simulate complex velocity profiles for comparison to the experimental ones. A good agreement was found between simulations and experiments providing wall slip is taken into account in the simulation.

Keywords: rheology, wall-slip, particle image velocimetry, extrusion, polycarbonate

1. Introduction

Due to the severe pressure and temperature conditions involved during polymer processing, the tooling is made of steel or aluminum and gives little access to the inside of the mold cavity or the die. The consequence is an incomplete knowledge of the phenomena that can appear in this 'black box' especially concerning the way the flow develops and is affected by the processing conditions and the mold or die specificities. It is therefore interesting to develop and implement techniques that can give more information about what happens during the process and also to check the validity of the numerical models.

Several methods have been investigated to characterize the flow within an injection mold or an extrusion die. The basic one is based on direct observation of the flow through a transparent window that is generally made of glass or quartz in order to withstand pressure and heat. This approach was successfully used by Yokoi *et al.* [1–5] to study phenomena such as jetting, weld lines and flow marks formation. Dowling and Bress [6] and Nabialek [7] also used this technique to compare mold filling simulations to actual behavior. Unfortunately, this method provides mainly qualitative information about the flow front and gives no quantitative measurements that would describe the flow more precisely.

In order to get a better description of the flow, optical techniques have been adapted to polymer processing. They are commonly used in other engineering sectors such as aero- or hydrodynamics but are not extensively used in polymer processing due to the difficulty of implementation in conditions close to industrial ones. One of the main difficulties is that these methods generally request one or two optical accesses to the flow, which means molds or

---

*Corresponding author, e-mail: lacrampe@ensm-douai.fr dies with transparent walls withstanding very high pressure and temperature.

Most techniques are based on laser particle velocimetry with two main physical principles to determine the local velocity. The first one uses the Doppler effect to measure the speed of seeds that are inserted into the fluid (Laser Doppler Velocimetry – LDV). It was used by several authors [8–11] to study polymer flow features such as flow instabilities in extrusion molding, wall slip and die swell. This method is very precise and convenient for detailed analyses of some phenomena. It is however time consuming due to the measurement principle, one point after the other, and is therefore not suitable for the study of transient flows such as those occurring during injection molding.

The second group of methods is based on optical particle tracking with different variants such as particle tracking velocimetry (PTV), particle streak imaging (PSV) or particle image velocimetry (PIV). They normally need two optical accesses to the flow, one for laser lighting and the other for particle movement recording. All variants use seeds to make the flow visible, at rather low concentration for PTV and PSV in order to be able to follow the particles individually, at a higher concentration for PIV due to the global analysis of the pictures. Martyn *et al*. [12] used PSV and PTV to study the recombination of polyethylene flows within a die whereas Yokoi *et al*. [13] used the same kind of techniques to study the filling of a mold with polystyrene. However, if the PIV technique is being increasingly used in the analysis of flow kinematics of non-newtonian fluids, in particular in the study of flow instabilities and wall slip, it has been rarely used to study molten polymer in industrial configurations (materials, machines and molds) due to the unfavorable and very constraining environment imposed by polymer processing (high pressure and temperature). As a consequence, little work has been published concerning measurements on real engineering thermoplastics (such as polycarbonate for example). Nigen *et al*. [14] used this method to analyze flow instabilities of model polymers (liquid at room temperature) when passing a sudden die contraction.

The measurement method chosen for this study is PIV. The aim was to check its applicability and efficiency to characterize the flow in test conditions as close as possible to real processing ones i.e. using a semi-industrial extrusion die connected to an industrial extruder and fed with an engineering polymer (polycarbonate). High temperatures and pressures were therefore involved in the experiments. Simple flows in a rectangular die were investigated as well as disrupted ones generated by a flow restriction. The direct observations of actual flows were then compared to numerical simulations. Due to significant wall slip appearing in the PIV measurements, wall slip was also taken into account in the simulation through rheological measurements based on the classical Mooney's method.

2. Experimental

The material chosen for this project was polycarbonate (PC, Lexan® from GE Plastics). For a comparison purpose, an other polymer, namely a polystyrene (PS, HH999 from BP Chemicals) has been used punctually. The processing equipment consisted of a single screw extruder (Kaufman®, screw diameter: 40 mm, $L/D = 22$) and a rectangular die specially developed for PIV measurements, connected to the extruder by an adaptation device. The die had a rectangular section (6 mm×60 mm) and a length equal to 200 mm, and contained a quartz transparent window (14 mm×80 mm) on two orthogonal faces (Figure 1) in order to meet the requirements of the PIV method. In a second step, the basic geometry was slightly modified by fixing a small obstacle (4 mm×8 mm×14 mm) on the bottom surface of the die. The maximum flow rate of the extruder was 30 kg/h, which corresponds to a maximum average velocity of 20 mm/s and a maximum apparent shear rate of 20 s^{-1}. Melt and die temperatures were set at the same level (280 to 320°C for polycarbonate and 220°C for polystyrene). The temperature control system of the die was that of the industrial extrusion machine. It is therefore necessarily less efficient than the temper-

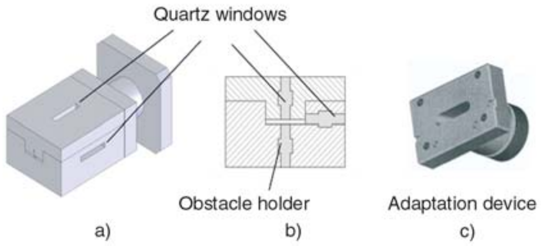

Figure 1. Extrusion die: a) overview, b) transverse section, c) adaptation device

ature control systems attached to laboratory devices such as capillary rheometers. That is why the experiments carried out on the industrial extruder have been always performed under the same conditions, after stabilization so as to reach a steady state and thus to limit this inconveniency.

PIV equipment was supplied by Dantec Dynamics. The principles of this measurement technique can be found elsewhere [15]. The lighting was generated by a Nd:YAG laser emitting at 532 nm (green). Optical lenses are used to create a 1 mm thick laser sheet. A CCD camera recorded the pictures. Aluminum powder (average diameter: 1.5 µm) was used as tracer at a weight concentration of 5 to $10\cdot10^{-4}$%. This material was chosen due to its high light reflectivity that appeared adequate after comparison with others materials (talcum, glass spheres). The time between photographs was adapted to the extrusion flow rate and varied from 5000 to 30000 µs. The size of the interrogation window (IW) was kept constant, equal to 64×64 pixels (i.e. 558×558 µm). The observation zone covered 25 IW resp. 11 IW in the flow direction resp. in the transverse direction. The choice of these parameters is the result of a compromise between the size of the gap to be observed, the image quality, the average displacement of the particles between two successive images and the mean flow rate.

Rheological measurements were carried out on a rheograph (Göttfert) using 0.5 and 1 mm capillary dies with a *L*/*D* ratio of 20. Wall slip was determined using the classical Mooney's method [17, 18]. For a capillary flow, it is based on Equation (1):

$$\dot{\gamma}_A = \dot{\gamma}_{A,S} + \frac{4V_s}{R} \tag{1}$$

where V_s is the slip velocity, $\dot{\gamma}_A$ the apparent shear rate (calculated from flow rate Q and die radius R by Equation (2)) and $\dot{\gamma}_{A,S}$ the apparent shear rate corrected for slip, which is only a function of the wall shear stress (τ_w).

$$\dot{\gamma}_A = \frac{4Q}{\pi R^3} \tag{2}$$

At constant shear stress, the slip velocity can then be calculated from a plot of $\dot{\gamma}_A$ vs. $1/R$, which is a straight line of $4V_s$ slope. To apply this method, it is therefore necessary to measure the flow curves τ_w vs. $\dot{\gamma}_A$ for capillaries of various diameters.

Numerical simulations were performed using REM 3D software package supplied by Transvalor. This finite elements software is dedicated to the three dimensional simulation of extrusion and injection molding processes and their variants (co-injection, co-extrusion, gas and water assisted injection molding). It contains a specific module based on a power law model (Equation (3)) to introduce wall slip in the computation.

$$\tau = \alpha\cdot K\cdot V_s^n \tag{3}$$

with τ the shear stress, α the slip coefficient, K the consistency, V_s the slip velocity and n the exponent of the power law.

3. Results and discussion

Two slightly different geometries were analyzed. The first corresponded to a basic flow in a rectangular die. It was used to implement and validate the method, and set the measurement parameters. It was also used to study the velocity profile through the thickness of the die. In the second case, the flow was disrupted by means of a geometrical discontinuity. This obstacle generated an abrupt step in the flow and a complex deviation of the latter. The resulting velocity profile was then compared to numerical simulations introducing wall slip in the computation on the basis of rheological measurements.

3.1. PIV measurements

3.1.1. Simple flows

A typical example of a velocity field measured in the rectangular die for polycarbonate is presented in Figure 2. Figure 3 shows the profiles through the thickness of the die for the different flow rates that can be reached with the processing equipment. Though the velocity profiles appear globally as quadratic power laws as one could expect for Newtonian flows (which is the case of polycarbonate in the range of temperature and flow rates covered by this study) between parallel plates, several peculiarities can be seen on these profiles. First, some velocity profiles are not symmetric with respect to the axis of the die. However it is worth reminding

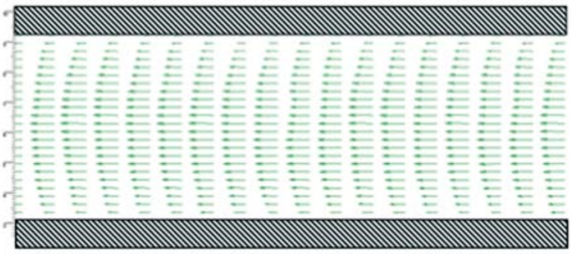

Figure 2. Typical experimental velocity field through the die (temperature: 280°C, shear rate: $8.2\ \mathrm{s}^{-1}$)

that the experiments were carried out on an industrial machine, whose temperature regulation is not perfect and may be slightly non-symmetric. Secondly, the speed is non-zero at the wall and can represent a significant part of the maximum speed for the lowest flow rates (Figure 3b). Thirdly, the profiles measured at shear rates above $13\ \mathrm{s}^{-1}$ have a bell shape instead of a pure parabolic one as it appears at lower flow rates.

The observations concerning wall slip are rather surprising if we consider the low shear rates ($< 20\ \mathrm{s}^{-1}$) involved in these experiments. Nevertheless, the measurements are relevant since the flow rate calculated from the velocity profile and the one obtained from melt weight measurements at the exit of the die show a good match (Figure 4). Wall slip has to be there to get this match. Furthermore, the measurements close to the wall fit perfectly to the global velocity profile, and the same result would have been obtained by extrapolating the wall velocity from the central part of the profile. The measurements close to the wall are therefore reliable and we can fairly conclude that there is a significant slip at the wall within the spatial precision range of the measurement technique (0.2–0.3 mm). A non-slip layer thinner than the resolution of the system is obviously possible but such layer has not been reported in the literature even when 10 time more precise methods were used [9, 10].

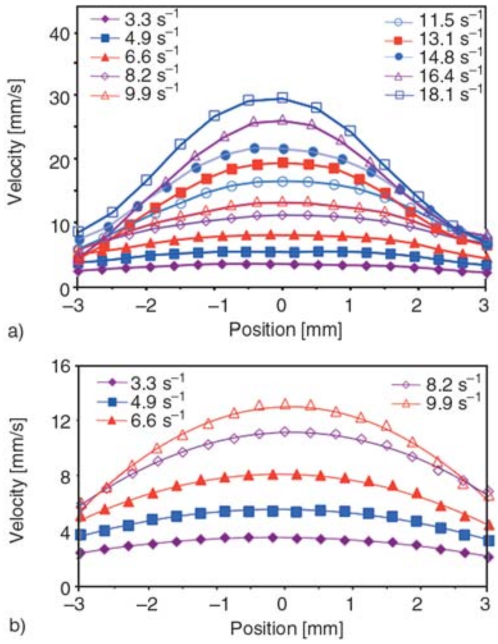

Figure 3. Flow profiles for various shear rates (temperature: 280°C): a) whole series of profiles, b) detail of the profiles at low shear rates

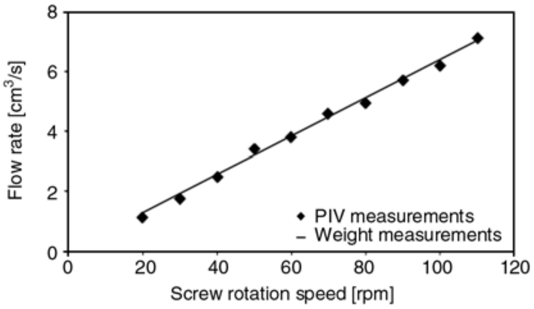

Figure 4. Comparison of the flow rates calculated from the velocity profiles and measured by melt weighing at the die outlet

Furthermore, similar tests were punctually carried out with PS. The analysis of the measured velocity fields (in the same flow rate range) does not show wall-slip phenomena, the measured velocity at wall being not significant ($<10^{-2}$ mm/s). Rheometry measurements carried out with PS also confirm the sticky nature of the flow in that case. These results tend to confirm that the peculiarities of the velocity profiles observed with PC may effectively be ascribed to its ability to slip at the die wall.

The consequence of wall slip in case of polycarbonate is that the velocity profiles are sensibly different from what can be expected when making the non-slip assumption as it can be seen on Figure 5. The velocity gradient is lower when slip is present ('flatter' profiles), the maximum speed is reduced and the flow can be quite close to plug flow with slip speed as high as 70% of the maximum speed. This also influences the other parameters of the process, for example by a reduction in the die inlet pressure, as it will be reported in section 3.2.

The evolution of the wall slip vs. shear rate is given in Figure 6. It shows a linear evolution at low flow rates and then tends to stabilize. This evolution can be explained by two phenomena acting in opposite ways on the wall slip. Since the tests are performed

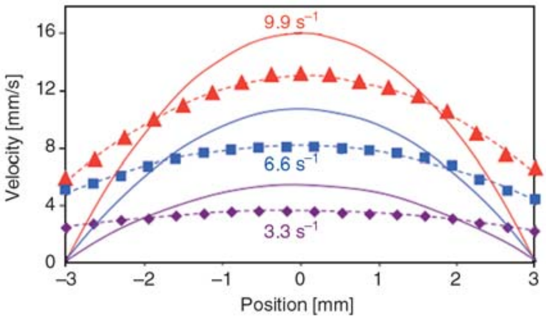

Figure 5. Experimental (symbols and dashed lines) vs. theoretical (solid line) velocity profiles through the die (Newtonian isothermal model between infinite parallel plates)

on an industrial extruder, the melt temperature is not fully controlled and depends on shear heating in the screw. Regarding the flowpath length, the viscous shear heating may become significant, contrary to what is observed on laboratory devices such as rheometers. As a consequence, the melt temperature rises when the screw rotation speed and therefore the flow rate are increased. Temperature measurements at the die exit showed a discrepancy of about 20°C between shear rates of 3 and 15 s^{-1} (Figure 6), whereas the shear heating induced temperature variations measured on the capillary rheometer remain lower than 2°C. This shear heating, which is important in industrial configurations, should generate more slip [16–18]. On the other hand, the results are presented vs. shear rate and not shear stress. The rise in temperature comes together with a decrease in viscosity and shear stress, and therefore a lower slip. In the particular case of polycarbonate considered in this study, the first phenomenon appears to be dominant, and, for a given apparent shear rate at the die wall, the reduction of the apparent shear stress (and thus the wall slip velocity) linked to the viscosity decrease is not enough to compensate the increase of the slip velocity induced by the temperature elevation.

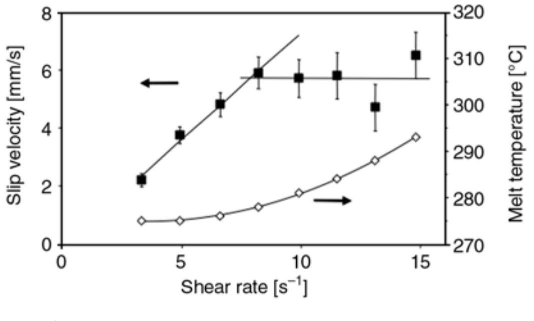

Figure 6. Wall slip velocity and melt temperature at the exit of the die vs. apparent shear rate (nominal temperature: 280°C)

The distortion of the profiles at high flow rates (Figure 3a) can also be explained by thermal effects. Because of the shear heating of the melt (Figure 6), the temperature profile through the die is no longer isothermal when the flow rate is increased. This temperature gradient comes together with other gradients of physical properties of the melt, especially its density and its refractive index. The melt acts therefore as a lens and deforms the images that have to cross 30 mm of melt to exit the die and reach the recording camera. This was clearly visible at high flow rates because an apparent image of the die surfaces was visible away from the boundaries given by the steel surfaces. The higher the speed was, the narrower the apparent image was, which shows the temperature dependence of the phenomenon. This effect was partly corrected by resetting the walls position on the basis of their apparent image but it was impossible to have a perfect correction between these boundaries since the temperature gradient was unknown. This explains the peculiar shape of the velocity profiles. This is a physical phenomenon that cannot be avoided and that has to be taken into account when analyzing the results.

3.1.2. Disrupted flows

In a second phase, the PC flow was disrupted by introducing a geometrical discontinuity. The results obtained with this configuration are presented in Figures 7 and 8. Figure 7 presents the observation from the side of the die, similar point of view to the one used in the previous section. In Figure 8, laser lighting and recording camera were swapped in order to study the flow from above at two different levels. Note that the observation window and the obstacle are much narrower than the total width of the channel (14 mm vs. 60 mm) i.e. the polymer can flow beyond the observation window and the obstacle.

These measurements give a good description of the deviation of the flow when passing the discontinuity. One can see the effect of a large step but also of a small one. The lack of adjustment of the fixation screw generates a 0.5 mm-deep depression on the surface of the obstacle. This creates waves and

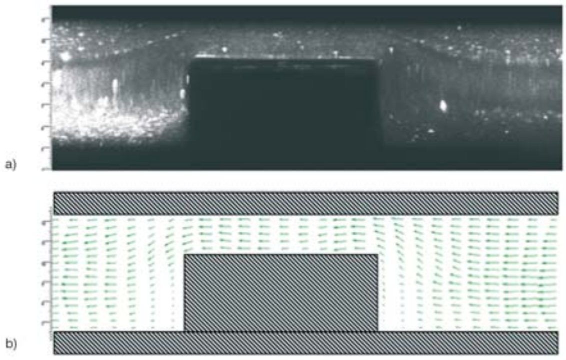

Figure 7. Velocity field in the vicinity of an obstacle (side view, flow from right to left): a) optical overview, b) velocity field

speed changes in the flow above the obstacle, which are recorded on the side view (Figure 7). The outline of this screw can also be distinguished on the top view (Figure 8c) through the distortion of the velocity field. The observation from two orthogonal points gives quantitative information about the three-dimensional flow. In the next section, these results will be compared to numerical simulations.

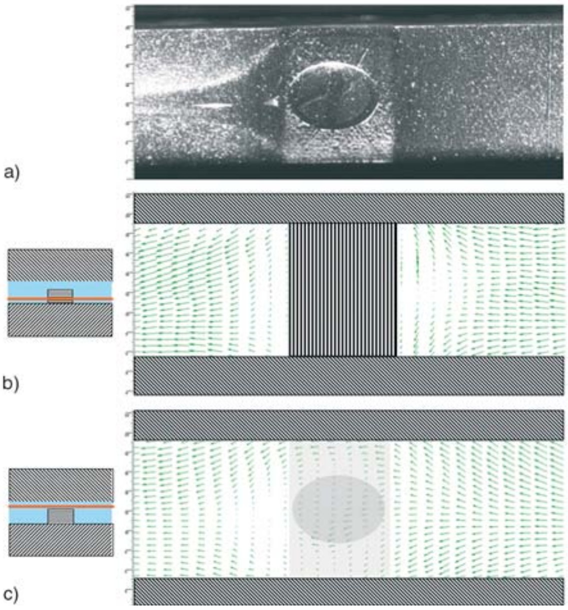

Figure 8: Velocity field in the vicinity of an obstacle (top view, flow from right to left): a) optical overview, b) velocity field below the obstacle surface, c) velocity field above the obstacle

3.2. Rheological measurements and numerical simulations

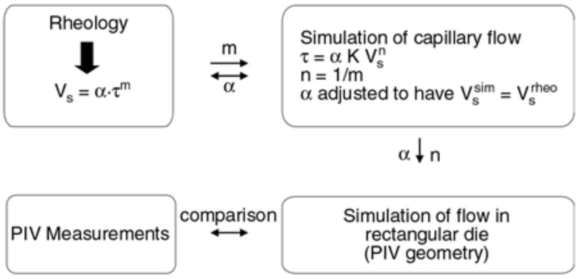

Figure 9. Combination of the different measurement and calculation results (for a given temperature)

Since wall slip was pointed out in section 3.1.1. for polycarbonate, this phenomenon was taken into account in the numerical simulations. The numerical slip parameters were determined using rheometry. Figure 9 gives an overview of the way the experimental results and numerical simulations were combined. The parameters of the numerical slip law were first determined on the basis of rheometry results, using the exponent *m* as it was measured and adjusting the slip coefficient α in order to get a good match between the numerical and the rheological slip velocity when simulating a capillary flow. Numerical simulations were then performed on geometries corresponding to the PIV die using the slip parameters determined at the previous step.

Flow curves (Figure 10) were measured for different die diameters. Based on Mooney's method, the discrepancy between these curves was used to calculate the slip velocity using the slope of the curve obtained when plotting the apparent shear rate vs. the reverse diameter at constant shear stress. Figure 11 shows the evolution of the slip velocity with the apparent shear stress. One can see that slip is present and does not show any clear critical stress corresponding to the onset of slip down to 0.04 MPa, the flow curves showing a progressive departure from each other (Figure 10). Wall slip is connected to shear stress through a power law (Equation (4)) within the range of shear stress covered by this study (0–0.18 MPa).

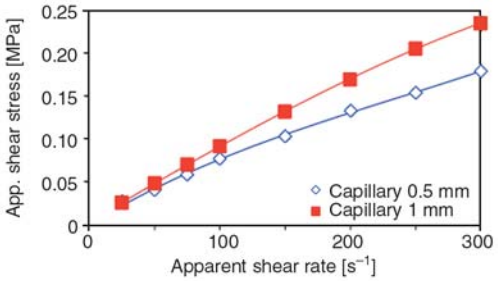

Figure 10. Flow curves for two capillaries diameters at 280°C

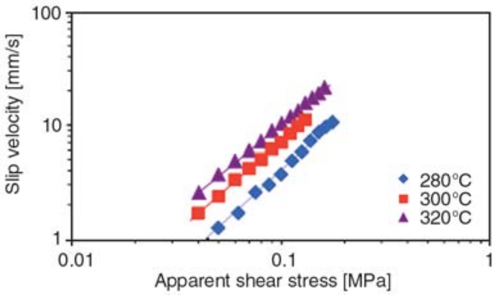

Figure 11. Slip velocity vs. apparent shear stress for different temperatures (capillary rheometry)

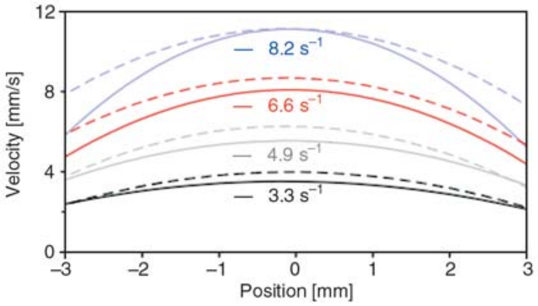

Figure 12. Experimental PIV velocity profiles through the thickness of the rectangular die (solid lines) and simulated profiles (dashed lines) for various shear rates

$$V_s = \alpha{\cdot}\tau^m \tag{4}$$

Table 1 reports the parameters of the law for different temperatures. It appears that temperature has a limited influence on the exponent *m* whereas the coefficient α is strongly sensitive to it. For a given apparent shear stress, an increase in temperature induces a high increase in wall-slip velocity. For example, at an apparent shear stress of 0.1 MPa, the wall-slip velocity increases by 90% between 280 and 300°C. The same trend was reported by Hatzikiriakos and Dealy [16, 17] in the case of high density polyethylene.

The ranges of shear rates used for capillary measurements (25–300 s^{-1}) and for PIV applied to extrusion (<15 s^{-1}) are different, but it was unfortunately not possible neither to measure accurately enough the slipping velocity at lower shear rate on the capillary rheometer (limitation due to the pressure sensor resolution), nor to extrude at higher wall-shear rates (limitation due to the extruder capacity). However, the lower limit range of the shear rates used in capillary experiments (25 s^{-1}) is not very far from the upper shear rates used in regular extrusion (15 s^{-1}). These rheological experiments thus contribute to point out the existence of wall slipping, and to explain at least in term of general trend, the PIV measurements carried out on the industrial extrusion machine.

Figure 12 compares the experimental and simulated global velocity profiles through the thickness of the die. One can see that the fit is good for the lowest shear rates (3.3 and 4.9 s^{-1}), whereas the discrepancy is more important, especially concerning the wall velocity, for the higher shear rates. This can be seen in Figure 13 that represents this velocity vs. apparent shear rate for simulation and experiment. One can see that the numerical results follow a power law as expected by the computing characteristics of the software. On the other hand, PIV measurements show a roughly linear evolution with shear rate and tend to stabilize above 8 s^{-1}. This phenomenon was explained previously by thermal effects and the higher effect of temperature-dependence of wall slip compared to that of viscosity. The divergence between numerical simulation and direct observation by PIV can be attributed to the fact that the simulation software package takes into account the only temperature-dependence of viscosity, but disregards the temperature-dependence of the parameters of the slipping law. In order to confirm this hypothesis, some calculations have been performed as described hereafter. The polymer melt temperature used in the simulation has been increased (i.e. the value of the shear heating experimentally measured at the die exit (Figure 6) has been added to the polymer melt temperature). Then, the parameters of the slipping law have been

Table 1. Parameters of the power law ($V_s = \alpha{\cdot}\tau^m$) describing the evolution of wall slip (in mm/s) vs. the apparent shear stress (in MPa) for different temperatures

Temperature [°C]	α [(mm/s)·MPa^{-m}]	m [–]
280	186	1.65
300	275	1.60
320	316	1.50

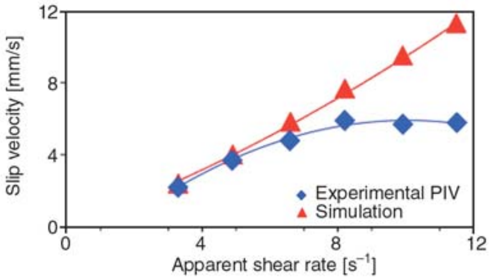

Figure 13. Experimental and numerical slip velocity vs. shear rate in the rectangular die at 280°C

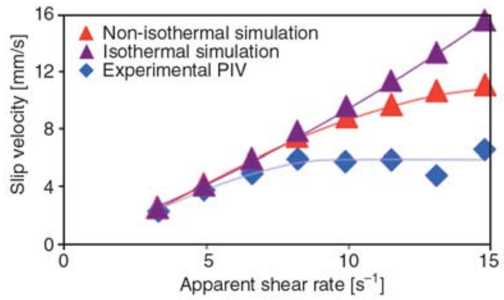

Figure 14. Slip velocity vs. apparent shear rate: influence of the increase in melt temperature on the simulated wall slip

adjusted accordingly by linear extrapolation between the rheological measurements at 280 and 300°C. The simulated results obtained that way (Figure 14) are much closer to the experimental results, and also show the same wall-slip velocity stabilisation at higher shear rates as the one observed experimentally. Even if the difference between simulation and measurements still remains significant at higher shear rates, these results demonstrate that it is interesting and of prime importance to take the above-mentioned temperature-dependence in the slipping law.

Figure 15 represents the numerical velocity profiles with and without slip. It definitely appears that the velocity profile is significantly influenced by wall slip with reduction in the velocity range through the thickness and lower velocity gradients. Not taking slip into account can therefore lead to numerical simulations that are significantly different from the reality, not only in terms of velocity profiles but also concerning other important parameters of the process. For example, the inlet pressure is divided by two when wall slip is present (Figure 16).

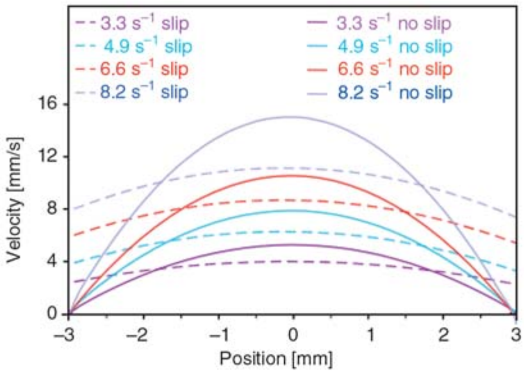

Figure 15. Numerical velocity profiles through the thickness of the die without (solid lines) and with (dashed lines) wall slip

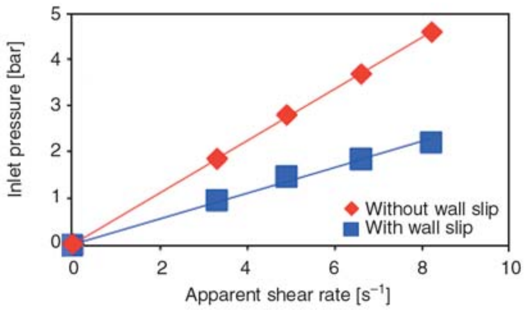

Figure 16. Simulated pressure at the entrance of the die vs. shear rate with and without wall slip

In a second step, the extrusion through the die with the geometrical discontinuity was simulated. Wall slip was introduced into the calculation using the same parameter as the one determined in the simple flow. Figure 17a shows the field of the x-component (main flow direction) of the velocity. The evolution of the speed globally as well as near the wall shows a good agreement with what can be observed in Figure 8. Wall speed changes in accordance with the local fluctuation of the stress due to passing of the complex obstacle.

Comparison with the non-slip case (Figure 17b) emphasizes the regulating effect of stick. The velocity fluctuations are much less pronounced in the absence of slip since the speed at the wall is always zero and is not sensitive to shear stress changes generated by the geometrical discontinuity. For example, the velocity in the center of the gap above the obstacle does not show more than 5% of variation along the obstacle in the stick condition whereas there is more than 30% decrease in velocity between the side and the center of the obstacle when wall slip is there. This shows that wall slip tends to destabilize the flow when passing geometrical singularities.

Figure 18 shows the flow lines around the discontinuity seen from the side and from above at two different levels. The agreement with Figures 7 and 8 is good, which proves the relevance of both experi-

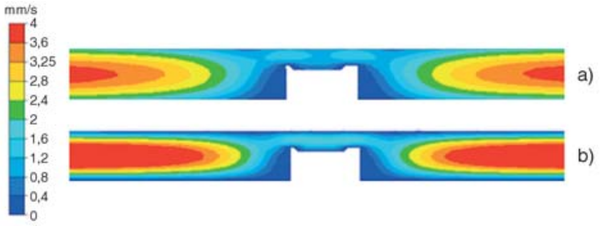

Figure 17. Simulated x-velocity field around an obstacle with (a) and without (b) wall slip (center plane, shear rate: 3.3 s^{-1})

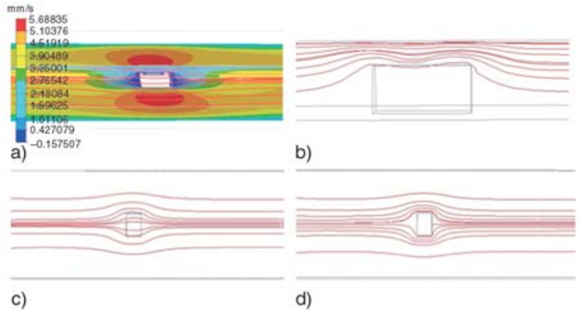

Figure 18. Simulated flow lines around an obstacle a) 3D overview (background: x-velocity map), b) side view, c) top view above the obstacle, d) top view below the obstacle surface

mental PIV measurements and numerical simulations. It is important to remember that the flow is complex with a real three dimensional behavior as shown in Figure 18a.

4. Conclusions and outlook

This study has shown the applicability of the PIV technique to characterize polymer flows in an extrusion die in very constraining conditions: real polymer (and not model fluid), industrial equipment (machine, tooling), high temperature, pressure and velocity conditions. PIV was successfully used to analyze the flow profiles globally as well as for a detailed analysis of the surface phenomena in the case of a particular reference of polycarbonate.

Furthermore, it was possible to highlight an unusual behavior of the polycarbonate investigated, characterized by a significant wall-slipping even at very low shear rate, confirmed by rheometry measurements. Numerical simulations using slip parameters determined on the basis of simple rheometrical measurements showed a good agreement with experimental direct observation at low shear rate. At higher shear rate, the necessity to introduce a temperature-dependence of the slip parameters has been shown. This requires a more extensive characterization of the temperature influence and the development of the adequate models to account for its effect more accurately in the simulation.

Nonetheless, determining the numerical slip parameters on the basis of simple rheometrical measurements appeared, at least qualitatively, to be an interesting way to introduce wall slip in the simulation of flows in more complex geometries. PIV measurements validated this approach, showing a quite good agreement of the wall velocity in industrial equipment with numerical simulations.

Acknowledgements

This work has been partly funded by the French Ministère de l'Économie des Finances et de l'Industrie, as part of 'Réseau National Matériaux et Procédés', project 'Masther'. The authors also wish to thank Transvalor for supplying the simulation software.

References

[1] Yokoi H., Hayashi T., Morikita N., Todd K.: Direct observation of jetting phenomena under a high injection pressure by using a prismatic-glass inserted mould. in 'Proceedings of the SPE Annual Technical Conference ANTEC'88, Atlanta, USA' 329–333 (1988).
[2] Yokoi H., Murata Y., Oka K., Watanabe H.: Visual analysis of weld line vanishing process by glass-inserted mould. in 'Proceedings of the SPE Annual Technical Conference ANTEC'91, Montreal, Canada' 367–371 (1991).
[3] Yokoi H., Nagami S., Kawasaki A., Murata Y.: Visual analysis of flow mark generation process using glass-inserted mould. I. Micro-grooved flow marks. in 'Proceedings of the SPE Annual Technical Conference ANTEC'94, San Francisco, USA' 368–372 (1994).
[4] Yokoi H., Deguchi Y., Sakamoto I., Murata Y.: Visual analyses of flow mark generation process using glass-inserted mould. II. Synchronous flow marks with same phases on both top and bottom surfaces of moulded samples. in 'Proceedings of the SPE Annual Technical Conference ANTEC'94, San Francisco, USA' 829–832 (1994).
[5] Yokoi H., Han X.: Visualization analysis of melt flowing behavior into micro-scale grooves during cavity filling process in injection molding. in 'Proceedings of the 21st Annual Meeting of the Polymer Processing Society, Leipzig, Germany' CD-ROM, SL 2.6, p8 (2005).
[6] Dowling D. R., Bress T. J.: Visualisation of injection moulding. in 'Proceedings of the SPE Annual Technical Conference ANTEC'97, Toronto, Canada' Vol III, 3692–3696 (1997).
[7] Nabialek J.: Monitoring and recording of the polymer flow in a mold cavity during the injection molding process. in 'Proceedings of the 21st Annual Meeting of the Polymer Processing Society (PPS-21), Leipzig, Germany' Paper P 13.7 (2005).

[8] Agassant J-F., Arda D., Combeaud C., Merten A., Münstedt H., Mackley M. R., Robert L., Vergne B.: Polymer processing extrusion instabilities and methods for their elimination or minimization. in 'Proceedings of the 21st Annual Meeting of the Polymer Processing Society (PPS-21), Leipzig, Germany' Paper KL 1.3 (2005).

[9] Münstedt H., Schmidt M., Wassner E.: Stick and slip phenomena during extrusion of polyethylene melts as investigated by laser-Doppler velocimetry. Journal of Rheology, **44**, 413–427 (2000).
DOI: 10.1122/1.551092

[10] Robert L., Demay Y., Vergnes B.: Stick-slip flow of high density polyethylene in a transparent slit die by laser Doppler velocimetry. Rheologica Acta, **43**, 89–98 (2004).
DOI: 10.1007/s00397-003-0323-x

[11] Mitsoulis E., Schwetz M., Münstedt H.: Entry flow of LDPE melts in a planar contraction. Journal of Non-Newtonian Fluid Mechanics, **111**, 41–61 (2003).
DOI: 10.1016/S0377-0257(03)00012-0

[12] Martyn M. T., Gough T., Spares S., Coates P. D., Zarloukal M.: Visualisation and analysis of LDPE melt flows in a coextrusion geometry. in 'Proceedings of the SPE Annual Technical Conference ANTEC 2002, San Francisco, USA' 937–941 (2002).

[13] Yokoi H., Inagaki Y.: Dynamic visualisation of cavity filling process along the thickness direction using a laser light sheet technique. in 'Proceedings of the SPE Annual technical Conference ANTEC'92, Detroit, USA' 457–460 (1992).

[14] Nigen S., El Kissi N., Piau J. M., Sadun S.: Velocity field for polymer melts extrusion using particle image velocimetry: Stable and unstable flow regimes. Journal of Non-Newtonian Fluid Mechanics, **112**, 177–202 (2003).
DOI: 10.1016/S0377-0257(03)00097-1

[15] Buchhave P.: Particle image velocimetry – status and trends. Experimentals Thermal and Fluid Science, **5**, 586–604 (1992).
DOI: 10.1016/0894-1777(92)90016-X

[16] Hatzikiriakos S. G., Dealy J. M.: Wall slip of molten high density polyethylene I. Sliding plate rheometer studies. Journal of Rheology, **35**, 497–523 (1991).
DOI: 10.1122/1.550178

[17] Hatzikiriakos S. G., Dealy J. M.: Wall slip of molten HDPE. II. Capillary rheometer studies. Journal of Rheology, **36**, 703–741 (1992).
DOI: 10.1122/1.550313

[18] Maciel A., Salas V., Soltero J. F. A., Guzman J., Manero O.: On the wall slip of polymer blends. Journal of Polymer Science Part B: Polymer Physics, **40**, 303–316 (2002).
DOI: 10.1002/polb.10093

eXPRESS Polymer Letters Vol.3, No.9 (2009) 579–587
Available online at www.expresspolymlett.com
DOI: 10.3144/expresspolymlett.2009.72

Actin dynamics and the elasticity of cytoskeletal networks

G. A. Buxton[1*], *N. Clarke*[2,3], *P. J. Hussey*[2,4]

[1]Department of Physics, Case Western Reserve University, Cleveland, OH 44106, USA
[2]Biophysical Sciences Institute, Durham University, Durham, DH1 3LE, UK
[3]Department of Chemistry, Durham University, Durham, DH1 3LE, UK
[4]School of Biological and Biomedical Sciences, Durham University, Durham, DH1 3LE, UK

Received 15 April 2009; accepted in revised form 26 June 2009

Abstract. The structural integrity of a cell depends on its cytoskeleton, which includes an actin network. This network is transient and depends upon the continual polymerization and depolymerization of actin. The degradation of an actin network, and a corresponding reduction in cell stiffness, can indicate the presence of disease. Numerical simulations will be invaluable for understanding the physics of these systems and the correlation between actin dynamics and elasticity. Here we develop a model that is capable of generating actin network structures. In particular, we develop a model of actin dynamics which considers the polymerization, depolymerization, nucleation, severing, and capping of actin filaments. The structures obtained are then fed directly into a mechanical model. This allows us to qualitatively assess the effects of changing various parameters associated with actin dynamics on the elasticity of the material.

Keywords: *modeling and simulation, biopolymers, actin networks, cytoskeleton*

1. Introduction

The cytoskeleton is an intricate network of biomacromolecules which pervade the cytoplasm of cells. The structural integrity of a cell depends upon its cytoskeleton, and for small deformations the elasticity of a cell depends on its actin network, a major constituent of the cytoskeleton. Actin networks are dynamic and consist of growing and shrinking filaments, and the cross-linking of these filaments in to a dynamic network. The purpose of this study is to capture the elasticity of actin networks as a function of their dynamic behavior. The correlation between actin dynamics and cellular elasticity can not only reveal interesting insights into the physics of cell mechanics, but also indicate the presence of disease [1]. For example, cancerous cells have been found to exhibit an increase in deformability commensurate with disease progression [2]. Understanding the interplay between cytoskeletal structure and stiffness, therefore, is important for both the diagnosis and treatment of this disease. In this study a computer model of actin dynamics yields network structures which can be directly fed into simulations of network elasticity. In other words, we use computer simulations to directly relate the elastic properties of an actin network to the actin dynamics responsible for the formation of this network.

Living cells have the ability to move and change shape in response to environmental stimuli; a consequence of the dynamic nature of the cytoskeleton and its actin network [3]. In particular, actin networks are formed from actin filaments which are transiently cross-linked by actin-binding proteins (proteins with an affinity for actin). These actin filaments continually polymerize and depolymerize to ensure a recycling of actin monomers, as they treadmill through the filaments, with a net polymer-

---

[*]Corresponding author, e-mail: gavin.buxton@case.edu

ization at the barbed end typically balancing a net depolymerization at the pointed end [4]. The barbed (+) and pointed (–) ends are structurally different and possess different polymerization kinetics. These dynamics are further regulated by adenosine triphosphate (ATP) hydrolysis; the ATP in free actin monomers that, once polymerized, hydrolyzes to adenosine diphosphate (ADP) and facilitates depolymerization [5]. Furthermore, cell-specific regulatory proteins not only cross-link these dynamic filaments but also cap, sever and help nucleate them [6, 7]. In order to understand the mechanical properties of actin networks we must first elucidate their structure [8]. Therefore, we develop a model which computationally captures these complex dynamics and generates network structures which serve as the input to an elastic model.

There have been many mathematical models of actin polymerization kinetics which yield average quantities [9–11], or simulations of individual filaments [12], however to directly simulate network elasticity, large-scale discrete models are required. For example, Huber *et al.* [13] have recently presented two-dimensional simulations of actin polymerization which included the diffusion and polymerization of individual actin monomers. Haviv *et al.* [14] adopted a similar kinetic Monte Carlo approach to model the self-assembly of asters and their transition into stars. Mogilner and Rubinstein [15] have also used stochastic models to simulate actin dynamics during filopedial protrusion. We adopt a similar, but more computationally efficient, approach and consider the filaments to be discretized into 100 nm segments. Other investigations of actin network elasticity, such as the studies of Huisman *et al.* [16] or DiDonna and Levine [17], have considered randomly generated network structures.

For many years the physics of elastic networks have attracted attention in relation to the deformation and fracture of heterogeneous materials and structures [18, 19]. However, recently this emphasis has shifted toward biological networks. Wilhelm and Frey [20] and Head *et al.* [21] investigated the deformation of two-dimensional networks and found that more densely packed structures deform more affinely (i.e., with a more uniform strain field) and that the individual filaments increasingly deformed more through stretching than through bending. Using a three-dimensional model of network elasticity we recently observed a similar bending-to-stretching transition as a function of network connectivity, which likewise corresponded with a transition to more affine deformations [22]. The ability to computationally capture the mechanics of network structures has led to recent computational investigations of actin networks. Didonna and Levine looked at the effects of protein unfolding in randomly generated two-dimensional networks [17]. Huisman *et al.* [16] looked at the deformation of three-dimensional random network structures as a method of elucidating the mechanics of actin networks. Recently, Broedersz *et al.* have theoretically looked at networks where the cross-links are assigned stiffnesses much lower than that of the filaments [23]. Here, we expand on these studies by considering network structures which are created directly from a simulation of the underlying actin dynamics. In other words, the output from a model of actin dynamics serves as the input to a mechanical model. The benefits of such a two-step methodology is that the mechanical properties of these networks can be directly correlated with the actin dynamics which led to network formation. We give details of this methodology in the following section, before presenting results and drawing relevant conclusions in subsequent sections.

2. Methodology

2.1. Generation of network

We employ the first reaction method to simulate actin dynamics, where actin filaments are discretized into regularly spaced nodes along the filament path [24]. Dynamic events are assigned rates at which they are likely to occur; for example, the polymerization and depolymerization at both filament ends, the nucleation of a filament, or the severing, capping and uncapping of existing filaments. Upon capping the polymerization kinetics at the barbed end are inhibited. Polymerization rates are taken to be proportional to the availability of free actin (i.e., $w_+ = k_+ \cdot C$, where C is the actin concentration). Nucleation can occur either spontaneously (through the formation of relatively stable trimers) leading to a concentration dependence of the form $w_{new} = k_{new} \cdot C^3$ [25], or nucleation can be initiated by actin binding proteins, with a rate given by

$w_{new} = k_{new}\cdot C$. The concentration of free actin is depleted as filaments are created or polymerize, and increased when filaments depolymerize. Due to the high diffusion coefficient of actin, and relatively slow growth of filaments, we assume spatial variations of actin can be neglected. The rate at which a filament is likely to be severed is proportional to its length (i.e., $w_{sever} = k_{sever}\cdot l$). Although it is worth noting that the hydrolysis of ATP-actin may effect the severing rate. For computational efficiency we do not include ATP hydrolysis as one of the kinetic events in the first reaction method, but rather assign a probability of hydrolysis occurring during the time step Δt of the form $P_{hydro} = 1 - \exp(-k_{hydro}\cdot\Delta t)$, where khydro is the rate of ATP hydrolysis on the actin filament. A filament segment with ATP-actin undergoes hydrolysis if a random number between zero and one is less than P_{hydro}. Upon polymerization a new node at the end of a filament is created with a position $r_{i+1} = r_i + r_0(r_i - r_{i-1} + \delta)/(|r_i - r_{i-1} + \delta|)$, where r_{i+1} is the position of the new node, $r_0 = 100$ nm is the spatial discretization of the filament and δ is a spherically symmetric random vector whose magnitude is chosen to coincide with the persistence length of actin filaments. In particular, the orientational correlation function $<\cos\theta> = \exp(-r_0/l_p)$, where $l_p = 17$ µm is the persistence length [26, 27]. The rate equations, therefore, do not describe the addition of actual molecular subunits but, rather, the sequential addition of several actin subunits 100 nm in length. Periodic boundary conditions are enforced on a system of size $L^3 = (20\ \mu\text{m})^3$ and filament lengths are limited to 20 µm and, therefore, do not span the length of the simulation box; we limit the size of the filaments to ensure that the elasticity of the network is due to the cross-linked network structure and not as a consequence of a single filament spanning the system. While this simulation size is comparable to the average filament length found in this study (typically less than 10 µm), it is still adequate to determine the constitutive response of these systems. In particular, Ostoja-Starzewski and Stahl [28] have found that displacement-based boundary conditions (as used here) can accurately capture the elastic properties of random networks even for relatively small system sizes.

A time is associated with each event of the form $\tau_i = -\ln(\varepsilon[0{:}1])/w_i$, where wi is the rate of the i^{th} event and $\varepsilon[0{:}1]$ is a random number between 0 and 1 [24]. The event with the lowest τ_i is executed at each iteration and this time is removed from the times associated with the remaining events. New τ_i's, for the recently performed (and any new) events, are calculated and, again, the event with the lowest τ_i is executed. The process is reiterated until steady state occurs. We start from an initial condition consisting of one hundred 1 µm long filaments, however, the final steady-state structures have evolved sufficiently that they are not sensitive to this choice. We run the simulations for $1\cdot10^8$ iterations (time steps are on the order of milliseconds). The systems considered here are observed to reach steady state before $1\cdot10^7$ iterations (defined as when the average quantities describing the system reach relatively constant values). Once the steady-state filament structures are established we determine a probability of cross-linking between neighboring segments.

From the tube model of actin filaments the fluctuations of a filament, perpendicular to its length, are believed to be limited to a distance of 400 nm [29]. Therefore, if the separation distance between two segments is greater than this distance we assume the probability of cross-linking to be zero. If distances are less than 400 nm the probability of cross-linking is taken to be of the form $P_{cross} = 1 - \exp(-k_{cross}\cdot\Delta t)$, where Δt refers to the time the segments have coexisted and k_{cross} is a rate of cross-linking. We take $k_{cross} = k_{AB}\cdot P_{AB}$, where P_{AB} is the probability of contact between two sites, defined as when two filaments (confined within tubes of 400 nm diameters) come within 40 nm of each other (the size of a cross-linking protein [30]). Therefore, the probability of contact is simply $P_{AB} = 0.01$ and we can vary k_{AB} to generate cross-linked structures with variable cross-link density.

2.2. Network elasticity

Once the network structures are obtained we can feed these structures directly into an elastic model and correlate network geometry with elastic properties. The elastic energy of a filament is given by Equation (1) [31]:

$$A = \frac{1}{2}Ea\int\left(\frac{\delta u}{\delta s}\right)^2\delta s + \frac{1}{2}EI\int\left(\frac{1}{R}\right)^2\delta s \qquad (1)$$

where the first term accounts for filament stretching and the second term filament bending. E is the

Young's modulus, a is the cross-sectional area, I is the area moment of inertia, R is the radius of curvature and u is the displacement along the filament curvature, s. Similar elastic models have proven to be highly successful at simulating the complex deformations of actin networks [16, 17, 32], and elastic networks in general [20, 21].

We take the flexural rigidity of the actin filaments to be $EI = 7.3\cdot10^{-26}$ N·m^2 [33] and the filament stiffness to be $34.5\cdot10^{-3}$ N·m^{-1} [34]. Cross-linking proteins are described by linear springs with a stiffness much lower than that of the actin filaments. In particular, the stiffness is taken to be $5\cdot10^{-5}$ [35] and the equilibrium length is taken to be 40 nm [30]. However, other more complicated elements could be considered; for example, DiDonna and Levine [17] have considered unfolding cross-links which reversibly unfold at a critical pulling force.

Maintaining periodic boundary conditions we can evolve the network to equilibrium using the following Langevin Equation (2):

$$F + \eta = \xi\frac{\mathrm{d}r}{\mathrm{d}t} \tag{2}$$

where ξ is the friction coefficient and η is a Gaussian noise term which satisfies the fluctuation dissipation theorem [36]. The filament is discretized into a series of points, or nodes, 100 nm apart. The velocity of a node is dr/dt and the elastic forces acting on this node is F. For numerical stability, $\xi/\Delta t$ is taken to be $10\cdot10^{-6}$ N·m^{-1} and $\eta = \sqrt{2k_bT\xi/\Delta t\cdot C}$ where Δt is the time step, k_b is the Boltzmann constant, $T = 300$ K is the temperature, and G is a Gaussian distributed random number with zero mean and unit standard deviation. Incorporating thermal noise into the relaxation dynamics ensures that we capture entropic effects. The shear modulus can then be obtained from the elastic energy density stored in a network as a consequence of the applied shear. This requires us to contrast the elastic energy in a given network subject to an applied shear (using Lee-Edwards boundary conditions) with the elastic energy in the same network without applied shear (but still in a non-equilibrium state due to thermal noise). In other words, the difference in elastic energy is related to shear modulus by $A_{shear} - A_{undeform} = G\cdot\gamma^2/2$, where A_{shear} and $A_{undeform}$ are the elastic energy densities in the sheared and undeformed networks, respectively [31]. Note that the elastic energy density is the total energy stored within all the elastic filaments in the simulation, divided by the volume of the simulation. G is the shear modulus and γ is the applied shear. The stretching and bending of actin filaments, or stretching of cross-link proteins, results in forces acting on the discrete nodes which characterize the filament backbone. These forces are used to evolve the Langevin equation, until the system relaxes to equilibrium. The difference in elastic energy density between equilibrated systems with and without applied shear can then be used to calculate the shear modulus. Furthermore, not only can we calculate the shear modulus but also isolate the contribution from different structural elements (stretching and bending energy of actin filaments and stretching energy of cross-linking proteins). The averages and standard deviations are presented from three independent simulation (with each simulation taking approximately 100 hours of cpu time on a standard linux processor).

3. Results and discussion

The polymerization kinetics are taken from Pollard *et al.* [7] (Table 1.). Note that due to our discretization the polymerization rates used in the simulation differ from those quoted and correspond to the polymerization of 100 nm pieces, rather than molecular subunits. The rate of hydrolysis is taken to be 0.3 s^{-1} [37] and the capping rate at the barbed end is taken to be 1 s^{-1} (although this will depend on the concentration of capping proteins). We vary the nucleation rate (for systems where the nucleation rate is either proportional to concentration, or the concentration cubed), the severing rate, the uncapping rate and the concentration of actin. The range of these parameters are given in Table 2.

Figure 1 shows a snapshot of a simulation with $k_{new} = 0.1$ μM^{-1}·s^{-1}·μm^{-3}, $k_{sever} = 1\cdot10^{-6}$ s^{-1}·μm^{-1}, $k_{uncap} = 0.1$ s^{-1} and $\theta = 1$ μM. The network is connected with a rate of cross-linking $k_{AB} = 1$ s^{-1}. The

Table 1. Polymerization kinetics [7]

Polymerization at barbed end with ATP-actin	11.6 s^{-1} μM^{-1}
Depolymerization at barbed end with ATP-actin	1.4 s^{-1}
Polymerization at pointed end with ADP-actin	0.16 s^{-1} μM^{-1}
Depolymerization at pointed end with ADP-actin	0.27 s^{-1}
Polymerization at barbed end with ADP-actin	3.8 s^{-1} μM^{-1}
Depolymerization at barbed end with ADP-actin	7.2 s^{-1}
Polymerization at pointed end with ATP-actin	1.3 s^{-1} μM^{-1}
Depolymerization at pointed end with ATP-actin	0.8 s^{-1}

Table 2. Polymerization rates

Nucleation rate	$k_{new} = 0.1 - 10\ \mu M^{-1}\cdot s^{-1}\cdot \mu m^{-3}$
Severing rate	$k_{sever} = 1\cdot 10^{-8} - 1\cdot 10^{-4}\ s^{-1}\cdot \mu m^{-1}$
Uncapping rate	$k_{uncap} = 0 - 1\ s^{-1}$
Actin concentration	$\theta = 0.5 - 1.5\ \mu M$

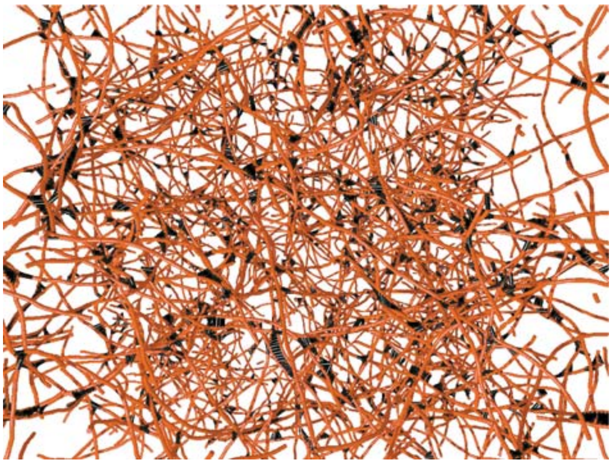

Figure 1. Snapshot of a simulation with $k_{new} = 0.1\ \mu M^{-1}\cdot s^{-1}\cdot \mu m^{-3}$, $k_{sever} = 1\cdot 10^{-6}\ s^{-1}\cdot \mu m^{-1}$, $k_{uncap} = 0.1\ s^{-1}$ and $\theta = 1\ \mu M$. The network is connected with a rate of cross-linking $k_{AB} = 1\ s^{-1}$. The filaments are shown as red cylinders and the cross-linking proteins are shown as black cylinders.

filaments are shown as red cylinders and the cross-linking proteins are shown as black cylinders. For this value of k_{AB} we find 6320 ± 8 cross-linking proteins (connecting 609 filaments with an average length of 8.2 µm). For smaller values of $k_{AB} = 0.01$ and 0.1, we find 2304 ± 39 and 5568 ± 25 proteins, respectively. In this study we maintain $k_{AB} = 1$ which corresponds to a relatively high cross-link density and note that smaller values of k_{AB} will increase the compliance of the networks.

The effects of varying the nucleation rate is shown in Figure 2. We vary the nucleation rate from 0.1 to 10 $\mu M^{-1}\cdot s^{-1}\cdot \mu m^{-3}$ (or $\mu M^{-3}\cdot s^{-1}\cdot \mu m^{-3}$ for $w_{new} = k_{new}\cdot C^3$). We contrast this difference in power and depict the average length of the filaments and the number of filaments. For power = 1 ($w_{new} = k_{new}\cdot C$) we find the average number of filaments increases from 500 to 3500 and the length decreases from 9 to 2 µm. For power = 3 ($w_{new} = k_{new}\cdot C^3$) the effects of varying k_{new} are less severe. The concentration of free actin in the systems considered here is roughly 0.6 µm and so the effects of increasing k_{new} are expected to be 3 times less for systems where power = 3.

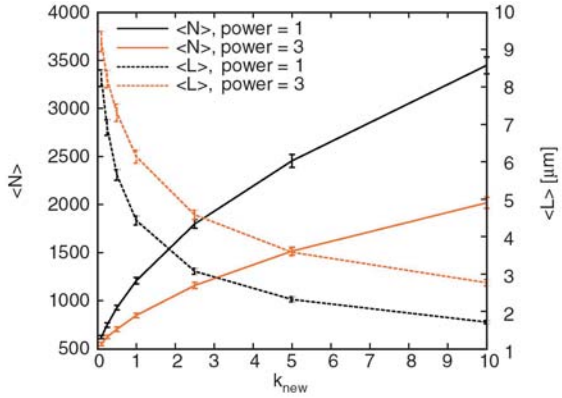

Figure 2. The effects of varying the nucleation rate from 0.1 to 10 $\mu M^{-1}\cdot s^{-1}\cdot \mu m^{-3}$ (or $\mu M^{-3}\cdot s^{-1}\cdot \mu m^{-3}$ for $w_{new} = k_{new}\cdot C^3$) on the number and average length of actin filaments. $k_{sever} = 1\cdot 10^{-6}\ s^{-1}\cdot \mu m^{-1}$, $k_{uncap} = 0.1\ s^{-1}$ and $\theta = 1\ \mu M$. Nucleation rates of the form $w_{new} = k_{new}\cdot C$ are contrasted with nucleation rates of the form $w_{new} = k_{new}\cdot C^3$ to compare spontaneous with protein mediated nucleation.

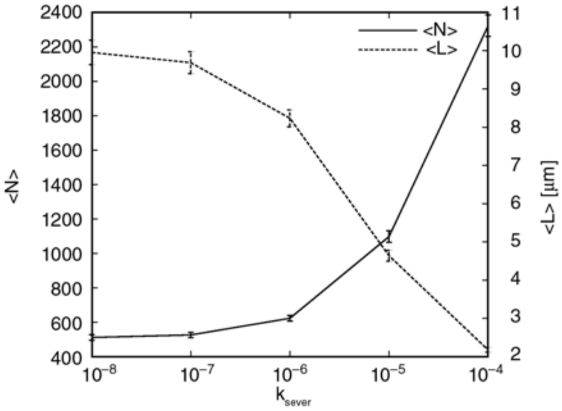

Figure 3. The effects of varying the severing rate over orders of magnitude (from $1\cdot 10^{-8}$ to $1\cdot 10^{-4}$) on the number and average length of actin filaments. $k_{new} = 0.1\ \mu M^{-1}\cdot s^{-1}\cdot \mu m^{-3}$, $k_{uncap} = 0.1\ s^{-1}$ and $\theta = 1\ \mu M$

Figure 3 shows the effects of varying k_{sever} from $1\cdot 10^{-8}$ to $1\cdot 10^{-4}$. As expected the number of filaments increases and the average length decrease. In particular, the number of filaments increases from 500 to 2200 and the average length decreases from 10 to 2 µm. This range of filament lengths is comparable to those found in experimental studies [38]. Figure 4 shows the effects of increasing the uncapping rate from 0.001 to 1 s^{-1}. The number of filaments initially decreases before increasing, while the average filament length doubles from 6 to 12 µm. The percentage of filaments that are capped as a function of uncapping rate is shown in the inset. As filaments become increasingly uncapped

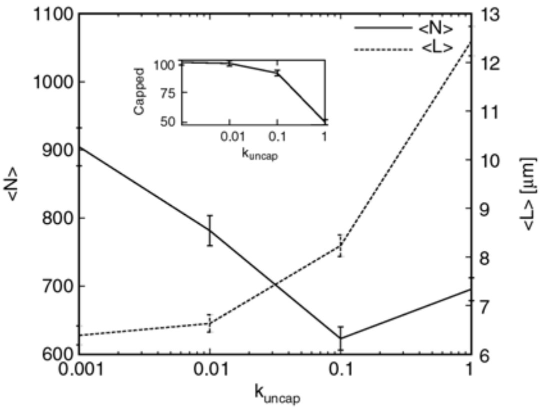

Figure 4. The effects of varying the uncapping rate (at the barbed end) from 0.001 to 1 s^{-1} on the number and average length of actin filaments. Note the capping rate is kept at 1 s^{-1}. k_{new} = 0.1 $\mu M^{-1} \cdot s^{-1} \cdot \mu m^{-3}$, $k_{sever} = 1 \cdot 10^{-6}$ $s^{-1} \cdot \mu m^{-1}$ and θ = 1 μM. The percentage of filaments which are capped is shown within the inset.

the length increases, as the polymerization kinetics are less inhibited, and the reduction in free actin reduces the nucleation rate. However, newly created filaments have a greater chance of survival as they are less likely to be capped. This reduction in filament nucleation, but increasing likelihood of filament survival, results in the number of filaments initially decreasing before increasing.

The effects of increasing actin concentration are shown in Figure 5. For an actin concentration of 0.5 μM there are relatively few filaments of very small length. As the concentration is increased to 1.5 μM the number of filaments increases linearly to 1200 and the average filament length increases to 9 μm. Newly created filaments consist of ATP-actin and the critical concentration at the pointed end with ATP-actin is 0.61. Therefore, the newly created filaments with concentrations less than this depolymerize from the pointed end and have less chance of survival, whereas for concentrations greater than 0.61 the filaments initially grow from both ends before hydrolysis ensures the preferential depolymerization of the pointed end. We, therefore, see a dramatic increase in filament length around a concentration of 0.61.

We now turn our attention to the mechanical properties of these networks. Figure 6 shows the effects of varying actin concentration on the shear modulus of the network. For the simulations shown in Figure 5 we feed the structures in to the mechanical model and calculate the shear modulus. The error bars correspond to the standard deviation of three runs. In particular, we plot the shear modulus as a function of F-actin concentration. As the total concentration of actin is increased to 1.5 μM the concentration of F-actin increases to 0.9 μM. This results in an exponential increase in the mechanical stiffness of the material. The shear modulus increases to 7 Pa as not only the density of the filaments increases, but also the number of cross-linking proteins increases. This range of shear modulus is consistent with experimental studies [39–41] although the shear modulus varies as the concentration to the power of 4.7 (rather than 2.5 as predicted theoretically and found in Gardel *et al.* [41]). This might be a consequence of the elastic energy being primarily stored within the cross-linking proteins and not the actin filaments.

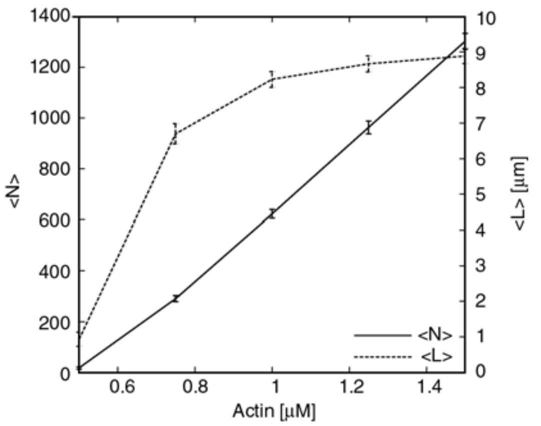

Figure 5. The effects of varying the total actin concentration from 0.5 to 1.5 μM on the number and average length of actin filaments. k_{new} = 0.1 $\mu M^{-1} \cdot s^{-1} \cdot \mu m^{-3}$, $k_{sever} = 1 \cdot 10^{-6}$ $s^{-1} \cdot \mu m^{-1}$ and k_{uncap} = 0.1 s^{-1}

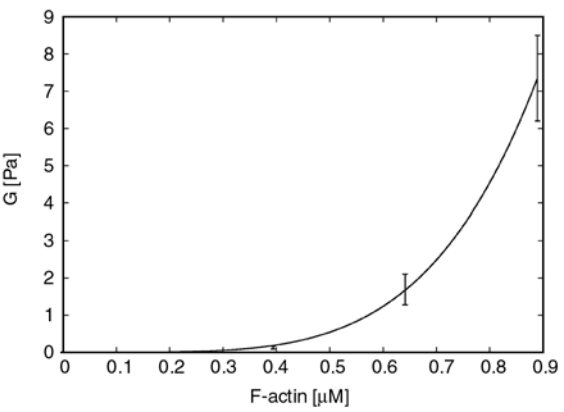

Figure 6. Plot of shear modulus, *G*, as a function of F-actin concentration. The variation in F-actin is obtained through varying the total actin concentration (see Figure 5)

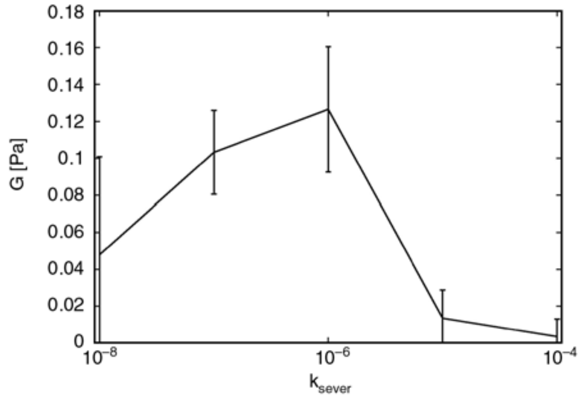

Figure 7. Plot of shear modulus as a function of severing rate. Increasing severing rates corresponds with a change in network structure from networks consisting of less larger filaments to more smaller filaments (see Figure 3)

The effects of increasing the severing rate in Figure 3 predictably resulted in an increase in the number of the filaments and a reduction in filament length. Figure 7 shows the effect of this on the mechanical properties of the actin networks. While the concentration of F-actin also shows a slight variation as a function of severing rate (not shown) the variations are on the order of a percent. The variation in mechanical stiffness is, therefore, a consequence of network geometry. In particular, neither the networks consisting of many small filaments, nor the networks consisting of just a few hundred large filaments, appear to provide the best mechanical properties. Interestingly, the optimum mechanical performance occurred in systems in between these two extremes.

4. Conclusions

To summarize, we have coupled a model of actin dynamics with a mechanical model to directly correlate network formation and elasticity. We model the network formation through a model which considers the rates at which various events occur (polymerization, depolymerization, nucleation, severing, capping, uncapping and hydrolysis). This is then fed directly into an elastic model which allows us to obtain a shear modulus for the structure. These preliminary results offer interesting physical insights into these systems, and provide a platform for developing specific biological models which could be directly compared to commensurate experimental studies.

Future work will further explore the parameter space and analyze the statistics of these heterogeneous networks. In particular, the severing rate might depend on the hydrolysis of ATP-actin and vary along the length of a filament (with ADP-actin more likely to sever [10]) or the heterogeneity of actin concentration could be important in modeling more realistic cellular environments. In terms of the mechanical simulations, the incorporation of nonlinear protein deformations as a consequence of protein unfolding could improve the dynamics of the model and future work could explore the effects of varying cross-link density.

The focus in the current study, however, was the development of a two-step methodology capable of correlating actin dynamics with actin network mechanics. Our new methodology could provide insights into how variations in actin dynamics between different systems, or in response to a disease [2], can ultimately effect the mechanical properties of the cell.

Acknowledgements

We thank Dr Junli Liu and Dr Bernard Piette (Durham University) for their critical reading of the manuscript, and the referees for their useful and insightful comments.

References

[1] Costa K. D.: Single-cell elastography: Probing for disease with the atomic force microscope. Disease Markers, **19**, 139–154 (2003).

[2] Guck J., Schinkinger S., Lincoln B., Wottawah F., Ebert S., Romeyke M., Lenz D., Erickson H. M., Ananthakrishnan R., Mitchell D., Kas J., Ulvick S., Bilby C.: Optical deformability as an inherent cell marker for testing malignant transformation and metastatic competence. Biophysical Journal, **88**, 3689–3698 (2005).
DOI: 10.1529/biophysj.104.045476

[3] Alberts B., Bray D., Johnson A., Lewis J., Raff M., Roberts K., Walter P.: Essential cell biology. An introduction to the molecular biology of the cell. Garland Publishing, New York (1998).

[4] Fujiwara I., Takahashi S., Tadakuma H., Funatsu T., Ishiwata S.: Microscopic analysis of polymerization dynamics with individual actin filaments. Nature Cell Biology, **4**, 666–673 (2002).
DOI: 10.1038/ncb841

[5] Korn E. D., Carlier M., Pantaloni D.: Actin polymerization and ATP hydrolysis. Science, **238**, 638–644 (1987).
DOI: 10.1126/science.3672117

[6] Pollard T. D., Cooper J. A.: Actin and actin-binding proteins. A critical evaluation of mechanisms and functions. Annual Review of Biochemistry, **55**, 987–1035 (1986).
DOI: 10.1146/annurev.bi.55.070186.005011

[7] Pollard T. D., Blanchoin L., Mullins R. D.: Molecular mechanisms controlling actin filament dynamics in nonmuscle cells. Annual Review of Biophysics and Biomolecular Structure, **29**, 545–576 (2000).
DOI: 10.1146/annurev.biophys.29.1.545

[8] Nossal R.: On the elasticity of cytoskeletal networks. Biophysical Journal, **53**, 349–359 (1988).
DOI: 10.1016/S0006-3495(88)83112-6

[9] Ermentrout G. B., Edelstein-Keshet L.: Models for the length distributions of actin filaments II: Polymerization and fragmentation by gelsolin acting together. Bulletin of Mathematical Biology, **60**, 477–503 (1998).
DOI: 10.1006/bulm.1997.0012

[10] Edelstein-Keshet L., Ermentrout G. B.: A model of actin filament length distribution in a lamellipod. Journal of Mathematical Biology, **43**, 325–355 (2001).
DOI: 10.1007/s002850100102

[11] Pollard T. D., Berro J.: Mathematical models and simulations of cellular processes based on actin filaments. Journal of Biological Chemistry, **284**, 5433–5437 (2009).
DOI: 10.1074/jbc.R800043200

[12] Roland J., Berro J., Michelot A., Blanchion L., Martiel J-L.: Stochastic severing of actin filaments by actin depolymerizing factor/cofilin controls the emergence of a steady dynamical regime. Biophysical Journal, **94**, 2082–2094 (2008).
DOI: 10.1529/biophysj.107.121988

[13] Huber F., Käs J., Stuhrmann B.: Growing actin networks from lamellipodium and lamellum by self-assembly. Biophysical Journal, **95**, 5508–5523 (2008).
DOI: 10.1529/biophysj.108.134817

[14] Haviv L., Brill-Karniely Y., Mahaffy R., Backouche F., Ben-Shaul A., Pollard T. D., Bernheim-Groswasser A.: Reconstitution of the transition from lamellipodium to filopodium in a membrane-free system. Proceedings of the National Academy Sciences, **103**, 4906–4911 (2006).
DOI: 10.1073/pnas.0508269103

[15] Mogilner A., Rubinstein B.: The physics of filopodial protrusion. Biophysical Journal, **89**, 782–795 (2005).
DOI: 10.1529/biophysj.104.056515

[16] Huisman E. M., van Dillen T., Onck P. R., van der Giessen E.: Three-dimensional cross-linked F-actin networks: Relation between network architecture and mechanical behavior. Physical Review Letters, **99**, 208103/1–208103/4 (2007).
DOI: 10.1103/PhysRevLett.99.208103

[17] DiDonna B. A., Levine A.: Filamin cross-linked semiflexible networks: Fragility under strain. Physical Review Letters, **97**, 068104/1–068104/4 (2006).
DOI: 10.1103/PhysRevLett.97.068104

[18] Hrennikov A.: Solution of problems of elasticity by the framework method. Journal of Applied Mechanics, **8**, 169–175 (1941).

[19] Kellomäki M., Åström J., Timonen J.: Rigidity and dynamics of random spring networks. Physical Review Letters, **77**, 2730–2733 (1996).
DOI: 10.1103/PhysRevLett.77.2730

[20] Wilhelm J., Frey E.: Elasticity of stiff polymer networks. Physical Review Letters, **91**, 108103/1–108103/4 (2003).
DOI: 10.1103/PhysRevLett.91.108103

[21] Head D. A., Levine A. J., MacKintosh F. C.: Deformation of cross-linked semiflexible polymer networks. Physical Review Letters, **91**, 108102/1–108102/4 (2003).
DOI: 10.1103/PhysRevLett.91.108102

[22] Buxton G. A., Clarke N.: 'Bending to stretching' transition in disordered networks. Physical Review Letters, **98**, 238103/1–238103/4 (2007).
DOI: 10.1103/PhysRevLett.98.238103

[23] Broedersz C. P., Storm C., MacKintosh F. C.: Nonlinear elasticity of composite networks of stiff biopolymers with flexible linkers. Physical Review Letters, **101**, 118103/1–118103/4 (2008).
DOI: 10.1103/PhysRevLett.101.118103

[24] Gibson M. A., Bruck J.: Efficient exact stochastic simulation of chemical systems with many species and many channels. Journal of Physical Chemistry A, **104**, 1876–1889 (2000).
DOI: 10.1021/jp993732q

[25] Lodish H., Berk A., Kaiser C. A., Krieger M., Scott M. P., Bretscher A., Ploegh H., Matsudaira P.: Molecular cell biology. Freeman, San Francisco (2007).

[26] Ott A., Magnasco M., Simon A., Libchaber A.: Measurement of the persistence length of polymerized actin using fluorescence microscopy. Physical Review Letters, **48**, R1642–R1645 (1993).

[27] Käs J., Strey H., Tang J. X., Finger D., Ezzell R., Sackmann E., Janmey P. A.: F-actin, a model polymer for semiflexible chains in dilute, semidilute, and liquid crystalline solutions. Biophysical Journal, **70**, 609–625 (1996).
DOI: 10.1016/S0006-3495(96)79630-3

[28] Ostoja-Starzewski M., Stahl D. C.: Random fiber networks and special elastic orthotropy of paper. Journal of Elasticity, **60**, 131–149 (2000).
DOI: 10.1023/A:1010844929730

[29] Isambert H., Maggs A. C.: Dynamics and rheology of actin solutions. Macromolecules, **29**, 1036–1040 (1996).
DOI: 10.1021/ma946418x

[30] Meyer R. K., Aebi U.: Bundling of actin filaments by A-actinin depends on its molecular length. The Journal of Cell Biology, **110**, 2013–2024 (1990).
DOI: 10.1083/jcb.110.6.2013

[31] Landau L. D., Lifshitz E. M.: Theory of elasticity. Pergamon Press, Oxford (1986).

[32] MacKintosh F. C., Kas J., Jamney P. A.: Elasticity of semiflexible biopolymer networks. Physical Review Letters, **75**, 4425–4428 (1995).
DOI: 10.1103/PhysRevLett.75.4425

[33] Gittes F., MacKintosh F. C.: Dynamic shear modulus of a semiflexible polymer network. Physical Review E, **58**, R1241–R1244 (1998).
DOI: 10.1103/PhysRevE.58.R1241

[34] Liu X., Pollack G. H.: Mechanics of F-actin characterized with microfabricated cantilevers. Biophysical Journal, **83**, 2705–2715 (2002).
DOI: 10.1016/S0006-3495(02)75280-6

[35] Ferrer J. M., Lee H., Chen J., Pelz B., Nakamura F., Kamm R. D., Lang M. J.: Measuring molecular rupture forces between single actin filaments and actin-binding proteins. Proceedings of the National Academy of Sciences, **105**, 9221–9226 (2008).
DOI: 10.1073/pnas.0706124105

[36] Coffey W. T., Kalmykov Y. P., Waldron J. T.: The Langevin equation. World Scientific, London (1996).

[37] Blanchoin L., Pollard T. D.: Hydrolysis of ATP by polymerized actin depends on the bound divalent cation but not profilin. Biochemistry, **41**, 597–602 (2002).
DOI: 10.1021/bi011214b

[38] Fujiwara I., Vavylonis D., Pollard T. D.: Polymerization kinetics of ADP- and ADP-P_i-actin determined by fluorescence microscopy. Proceedings of the National Academy of Sciences, **104**, 8827–8832 (2007).
DOI: 10.1073/pnas.0702510104

[39] Gardel M. L., Nakamura F., Hartwig J., Crocker J. C., Strossel T. P., Weitz D. A.: Stress-dependent elasticity of composite actin networks as a model for cell behavior. Physical Review Letters, **96**, 088102/1–088102/4 (2006).
DOI: 10.1103/PhysRevLett.96.088102

[40] Janmey P. A., Hvidt S., Käs J., Lerche D., Maggs A., Sackmann E., Schliwa M., Stossel T. P.: On the mechanical properties of actin gels. Journal of Biological Chemistry, **269**, 32503–32513 (1994).

[41] Gardel M. L., Shin J. H., MacKintosh F. C., Mahadevan L., Matsudaira P., Weitz D. A.: Elastic behavior of cross-linked and bundled actin networks. Science, **304**, 1301–1305 (2004).
DOI: 10.1126/science.1095087

eXPRESS Polymer Letters Vol.3, No.9 (2009) 588–594
Available online at www.expresspolymlett.com
DOI: 10.3144/expresspolymlett.2009.73

How carbon nanotubes affect the cure kinetics and glass transition temperature of their epoxy composites? – A review

*A. Allaoui, N. El Bounia**

IPREM-CANBIO, CNRS UMR 5254, Université de Pau et des Pays de l'Adour, Pau, France

Received 6 May 2009; accepted in revised form 26 June 2009

Abstract. Motivated by the widespread and contradictory results regarding the glass transition temperature of carbon nanotube (CNT)/epoxy composites, we reviewed and analyzed the literature results dealing with the effect of unmodified multiwall carbon nanotubes (MWNT) on the cure behaviour of an epoxy resin (as a possible source of this discrepancy). The aim of this work was to clarify the effective role of unmodified multiwall carbon nanotubes on the cure kinetics and glass transition temperature (T_g) of their epoxy composites. It was found that various authors reported an acceleration effect of CNT. The cure reaction was promoted in its early stage which may be due to the catalyst particles present in the CNT raw material. While SWNT may lead to a decrease of T_g due to their bundling tendency, results reported for MWNT suggested an increased or unchanged T_g of the composites. The present status of the literature does not allow to isolate the effect of MWNT on the T_g due to the lack of a study providing essential information such as CNT purity, glass transition temperature along with the corresponding cure degree.

Keywords: *nanocomposites, carbon nanotubes, cure kinetics, glass transition temperature*

1. Introduction

The use of carbon nanotubes (CNT) as nanofillers in polymer matrices is one of their most promising applications, especially regarding epoxy resin. Multiple enhanced properties at low loadings are the major advantage of CNT over other fillers. Thanks to its good mechanical properties, chemical resistance and thermal stability, epoxy resin is a widely used polymer as adhesive, coating or as matrix in structural composites. The choice of a given application for epoxy is often based on the glass transition temperature, noted as T_g. This is the temperature at which the mechanical properties of a polymer drop and corresponds to a second-order phase transition at which the polymer goes from a glassy to a rubbery behaviour as the temperature increases. The T_g is closely linked to the thermomechanical stability, it is thus the property that dictates the potential application of a given epoxy resin as a function of the service temperature range envisioned. In the case of epoxy resin, the T_g is a function of the molecular architecture and depends on different parameter such as the functionality of the epoxy and of the hardener, the conversion degree, the curing cycle, etc. Due to the close relation between cure behaviour, glass transition temperature, mechanical properties and potential application of an epoxy resin, it is primordial to study the effect of CNT on the cure behaviour of the epoxy resin matrix.

---

*Corresponding author, e-mail: noureddine.elbounia@univ-pau.fr

2. Cure kinetics

In the literature, different works were dedicated to the determination of the effect of CNT on the cure kinetics of an epoxy resin. Puglia *et al.* [1] claimed an acceleration effect of single wall carbon nanotubes (SWNT) on the cure reaction of the DGEBA/DETA epoxy system studied with dynamic and isothermal DSC. In that work, the decrease of the peak temperature (that is the temperature at the heat flow peak) in dynamic scans and the decrease of the time at heat flow peak in isothermal scans were taken as the proof of the acceleration in the early stage of the cure process. The presence of amine functional groups ($–NH_2$) on the surface of the SWNT that may react with the epoxy ring was the origin of the modification of the cure behaviour as shown in a paper from the same group presenting additional data on the same samples [2]. Xie *et al.* [3] also reported an acceleration effect in the case of multiwall carbon nanotubes (MWNT) for the TGDDM/DDS epoxy system using isothermal DSC. The higher initial reaction rate of the composites compared to the unfilled resin, the decrease of the time at maximum reaction rate and of the activation energy with increasing MWNT content were the indication of the acceleration effect. Evidence of the presence of hydroxyl groups (–OH) on the surface of the MWNT by FTIR spectroscopy which have a catalytic effect on epoxy ring opening was in that case the source of the modified cure. The last stage of the cure remained unaffected by MWNT. The same group reported [4] on the effect of carbon nanofibres (CNF) on the cure behaviour of the same epoxy system. They found a very small acceleration effect of CNF in the early stage of the reaction suggested by the decrease of the activation energy with an increase of the CNF content. On the other hand, the CNF hinders the reaction after that step. Tao *et al.* [5] studied the effect of SWNT in the DGEBF/DETD epoxy system and observed a decrease of the onset temperature in dynamic scans and a decrease of the time at maximum reaction in isothermal scans. Contrary to previous studies, they found that the peak temperature remained unaffected by the presence of SWNT. The origin of the acceleration effect cannot be clearly determined in their work due to the absence of surface characterization of the SWNT material. The high percentage of catalyst particles in the SWNT raw material may be a plausible source of the early cure initiation. In these investigations [1–5], it is believed that the modification of the cure behaviour in its early stage can be attributed to surface functional groups on CNT or catalyst particles. Wu *et al.* [6] studied the effect of three different carbon fillers (carbon fiber, carbon nanofiber and carbon black) on the cure reaction of the DGEBF/TETA epoxy system. They reported an increase of the total heat of reaction and a decrease of the temperature at the heat flow peak for all fillers. By comparing the effect of different pre-treatments of the carbon fibers, they explained the increase in the total heat of reaction as a result of the presence of surface functional groups on the fillers. The authors found that the acceleration effect, that is the decrease of the peak temperature, was closely related to the specific surface area (SSA) of the filler, in view of the proportionality between the SSA and the peak temperature drop (the higher the SSA, the higher the temperature drop). It should be noted that in that work, the fillers were manually dispersed in the resin and the filler content was high (around 20 wt%). The authors did not give indication on the dispersion state of the fillers. Their samples may not have been homogeneous at the micro-scale and should have mainly contained aggregates of the filler, especially in the case of CNF which are highly entangled and stick to each other by van der Waals interactions. Bae *et al.* [7] investigated the effect of CNT and carbon black (CB) on the cure reaction of liquid crystalline epoxy (DGE-DHAMS/sulfanilamide). In contradiction with all other studies, these authors reported a retardation effect of CNT, indicated by the slight increase of the temperature at maximum reaction. In their study, the presence of CNT did not have a significant effect on the total heat of reaction (except the expected decrease due to the lower weight fraction of epoxy in the composite) nor on the activation energy compared to unfilled epoxy. The authors noted that ΔH_0 was higher with CNT than with CB. The oxidation treatment decreased the activation energy in both cases.

3. Glass transition temperature

Regarding the T_g, the data of Puglia *et al.* [1] revealed higher curing degree of the composites compared to unfilled resin which may correspond to a higher T_g. The T_g was not measured in their work. Similarly, Xie *et al.* [3] did not measure the T_g of their samples but their data revealed a higher curing degree of the composites for curing temperatures below 200°C. For higher curing temperatures, the curing degree of the epoxy was higher. The same group [4] found that CNF did not have any effect on the final curing degree. Tao *et al.* [5] measured the T_g of their samples after 2, 5 and 24 hours of isothermal curing and found that the T_g of the composites was always lower than the unfilled epoxy. They attributed this to the lower curing degree of the composites as indicated by their lower isothermal heat of reaction but the curing degree was not explicitly calculated.

The literature dedicated to CNT/epoxy composites is extremely prolific. Given the importance of the glass transition temperature in view of its link with mechanical properties, it is amazing to see that even the last publications on the subject still do not always provide this information. In the case of mechanical properties, for comparison purpose, it is primordial to have the T_g provided along with the curing degree of the samples. Most of the studies only claimed complete cure of the samples without further investigation. An analysis of the results from the literature dedicated to unmodified CNT in epoxy should lead to valuable conclusions. Any variations in the T_g may be explained by some size effect or physical interactions with polymer chains close to CNT surface, the unmodified nature of the filler should eliminate the need of explanations involving chemical effects. We thus compiled and analyzed data values of glass transition temperature of CNT/epoxy composites from different articles. The CNT used in these works were unmodified MWNT [8–16] or unmodified SWNT [5, 17–22]. The data relative to preparation method of the composites, glass transition temperature and its measurement method are summarized in Table 1. The relative difference of T_g between CNT filled epoxy and the unfilled epoxy as a function of the T_g of the unfilled resin or the weight fraction of CNT is plotted respectively in Figure 1a and 1b. In the graphs, the case of SWNT as filler was differentiated from that of MWNT due to the tendency of SWNT to form close-packed bundles with triangular arrangement in the section. It can be noticed that most of the data for SWNT showed a decrease of T_g compared to the unfilled resin which may be a consequence of this bundling tendency. Moniruzzaman *et al.* [21] developed a dispersion method allowing to debundle SWNT and found that T_g was unaffected by the presence of SWNT. The data for MWNT was more scattered and no clear trend appeared. The difficulty in analyzing these data resided primarily in the fact that the final cure degree was not provided. Liao *et al.* [22] showed that the use of solvent of surfactant in the fabrication process can lead to a large decrease of the T_g. Even after a relatively long process of evaporation (one hour heating + 4 hours degassing), Lau *et al.* [23] reported that remaining residual traces of the solvent (acetone, ethanol and DMF) used in the dispersion process of SWNT in the epoxy resin led to a decrease of the mechanical properties of the SWNT/epoxy composites. They noticed that these detrimental effects increased with the boiling point of the solvent. We plotted again the data for MWNT and made the distinction between experiments in which solvent was used or not in the dispersion process of MWNT in the resin (Figure 2a

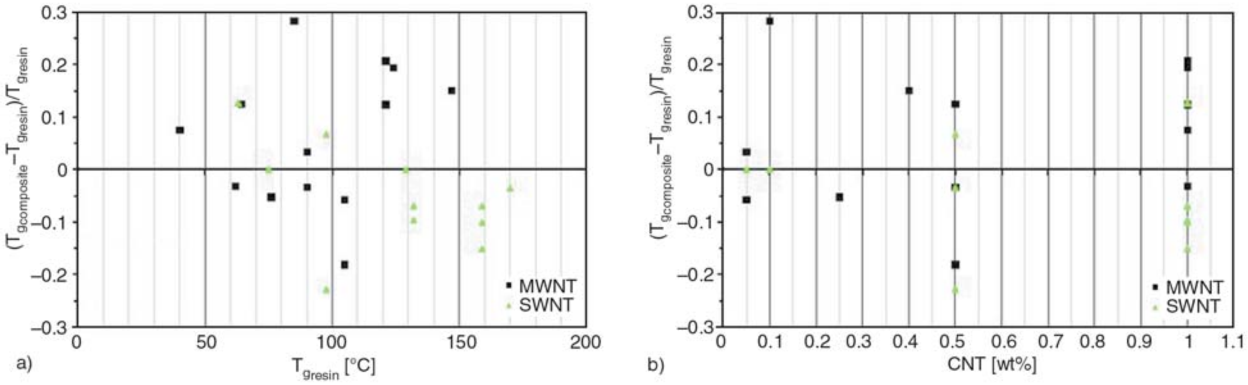

Figure 1. Relative difference of T_g of CNT composites compared to unfilled resin as a function of a) T_g of the unfilled resin b) CNT weight percentage (data taken from the literature)

Table 1. Compilation of data from the literature on CNT/epoxy composites (preparation method and glass transition temperature and measurement method, CNT type and aspect ratio when available)

Reference	CNT dispersion process	T_g Measure method	wt% CNT	CNT type	CNT aspect ratio (length/ diameter)	T_{gresin} [°C]	ΔT = $T_{gcomposite} - T_{gresin}$ [°C]
Tao *et al.* [5]	Grinding/acetone	DSC	1.0	Short SWNT	417	159.0	–24.0
				HiPCO SWNT	–		–11.0
				SWNT/DWNT	–		–16.0
Zhou *et al.* [8]	USP	DMA	0.4	MWNT	150	147.0	22.0
Ganguli *et al.* [9]	Shear mixing/USP	DMA	1.0	MWNT	625	124.0	24.0
Ganguli *et al.* [10]	High speed mixing	DMA	0.1	MWNT	125	85.0	24.0
Shen *et al.* [11]	High speed stirring/USP	DSC	1.0	MWNT	1750	62.0	–2.0
				MWNT-CONH	–		–19.0
Tseng *et al.* [12]	Shear mixing/USP	DSC	1.0	MWNT	–	40.0	3.0
				Plasma maleic anhydride-grafted MWNT	–		10.0
Gojny *et al.* [13]	USP	DMA	0.5	MWNT	3333	64.5	8.0
				MWNT-NH_2	3333		14.0
Shen *et al.* [14]	High speed stirring/USP	DSC	0.25	MWNT	1750	76.0	–4.0
				Diaminodiphenyl methane-MWNT	–		–8.0
				Diaminodicyclohexyl methane-MWNT	–		7.0
Hernandez-Perez *et al.* [15]	USP/ethanol/stirring	DMA	1.0	MWNT	50	121.0	15.0
				MWNT	857		25.0
Fidelus *et al.* [16]	Tip/Bath USP/THF	DMA	0.5	MWNT	85	90.0	1.0
	Tip/Bath USP/surfactant	DMA	0.5	SWNT	1000		2.0
	Tip/Bath USP/THF	DMA	0.5	MWNT	85	105.0	–15.0
	Tip/Bath USP/surfactant	DMA	0.5	SWNT	1000		–2.0
Gong *et al.* [17]	Stirring	DMA	1.0	MWNT	–	63.0	9.0
	Stirring/acetone/surfactant						25.0
Wang *et al.* [18]	USP/acetone	DMA	0.5	SWNT	–	170.0	–6.0
				SWNT-NH_2	–		–11.0
Wang *et al.* [19]	USP/acetone	TMA	1.0	SWNT	500	132.0	–12.7
				Chopped SWNT	–		–9.1
				Oxidized SWNT	–		–2.4
				Gum Arabic wrapped SWNT	–		–21.4
Valentini *et al.* [20]	USP	DMA	0.1	SWNT	357	75.0	0.0
				Butylamine-SWNT	–		10.0
Moniruzzaman *et al.* [21]	USP/DMF/high shear mixer	DSC	0.05	SWNT	–	129.0	0.0
Liao *et al.* [22]	Surfactant/acetone/manual stirring	DMA	0.5	SWNT	–	97.6	–23.6
	Bath/tip USP						6.6
	Tip USP/acetone						–22.2
	Bath USP/surfactant						–22.2
	Tip USP/surfactant						–13.4
	Bath/tip USP/surfactant/ acetone						–7.5

(USP: Ultra Sonic Processing)

and 2b). These plots led us to the conjecture that the use of unmodified MWNT as fillers in epoxy may increase or not change the glass transition temperature.

The curing agent type and concentration plays an important role on the final T_g of the resin. Curing agent with high functionality provide high T_g. The T_g can also be modified by the curing agent/resin ratio, using a ratio in little excess of the stochiometry gives higher T_g. The cure behaviour of an epoxy resin can be divided into two stages, a first one in which the reaction is chemically controlled and a

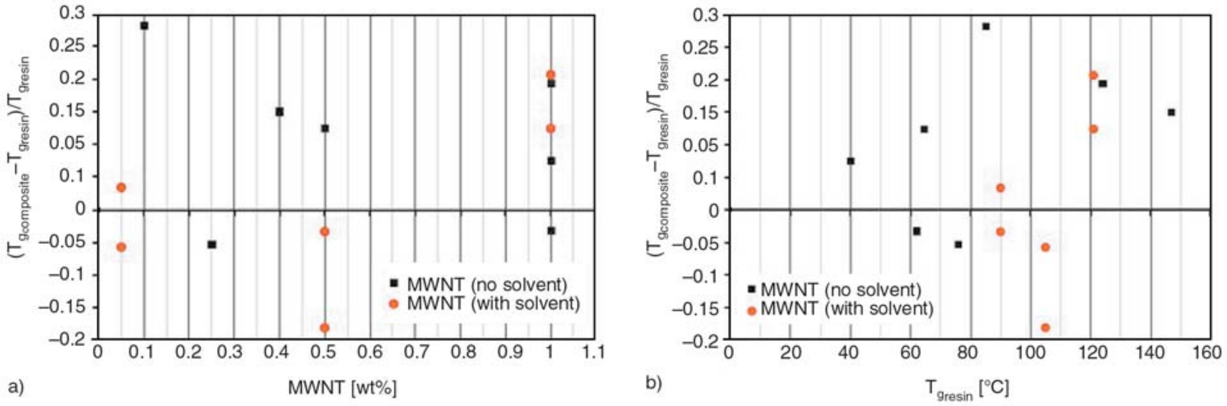

Figure 2. Relative difference of T_g of unmodified MWNT composites compared to unfilled resin as a function of a) CNT weight percentage, b) T_g of the unfilled resin (data taken from the literature)

second one in which diffusion dominates due to the phenomena of gelation and vitrification. In the early stage, the reaction is initiated by any hydrogen-bond donor molecules which can be moisture, impurities… The reaction is then accelerated by these molecules and the hydroxyl groups formed during the reaction. In the last stage, the viscosity of the mixture increase significantly and the reaction is diffusion-controlled. In the case of epoxy with MWNT, the presence of catalyst particles can initiate the reaction earlier compared to the unfilled resin. The introduction of MWNT in epoxy was found to increase significantly the viscosity of the mixture, up to one of order of magnitude with 1 wt% MWNT [24]. The improvement of the CNT dispersion state using a mechanical method led to an additional viscosity increase with factor 2. It is thus expected that the diffusion-controlled stage may be reached earlier in the case of the composites due to the higher viscosity level. The 'advanced' cure degree obtained in the early stage could be counterbalanced by the rapid decrease of the cure in the diffusion-controlled stage. Lower or comparable cure degrees of the composites compared to the resin are expected. Lower cure degree should lead to lower T_g. In view of their dimensions comparable to polymer chains, CNT could limit their mobility and provide higher T_g level. The lower cure degree could be counterbalanced by the restricted mobility of the polymer chains in the vicinity of the CNT. High aspect ratio and good dispersion state of CNT in the epoxy may promote the mobility reduction effect. The presence of CNT could also modify the structure of the final epoxy network which may present a gradient of cross-linking points around CNT. The use of an over-aged hardener [25] gave a rubbery epoxy and remarkable improvement of mechanical and electrical properties with 1 wt% MWNT. These improvements could be attributed to the loose nature of the rubbery epoxy network which was modified by MWNT. MWNT may have a perturbation effect during the formation of the epoxy network (with more cross-linking points around CNT) allowing them to act as an effective reinforcement. A thermal treatment of epoxy close to its T_g allows to study the effect of physical aging which allows some rearrangement of the polymer chains. It was found that physical aging limits the strain range over which CNT effectively reinforce the epoxy matrix [26] suggesting possible formation of voids between polymer chains with reduced mobility at the vicinity of CNT and 'free' chains allowed to rearrange through physical aging and sufficiently far from CNT.

The case of functionalized CNT is more complex due to the presence of surface groups that can react with the resin or the hardener, variations of T_g are thus expected due to the modified chemical reaction. Miyagawa *et al.* [27] dispersed fluorinated SWNT in a DGBEF epoxy and observed a decrease of T_g that they explained by the non-stoichiometric balance of epoxy to hardener due to fluorine on the surface of SWNT. Even after adjusting the amount of the anhydride hardener, the T_g of the composites was always lower than that of the resin. They also observed a slight decrease of the T_g when vapour grown carbon fibers (VGCF) were used as fillers in epoxy. They attributed this effect to hydroxyl groups present on the surface of VGCF that can react with hardener. Valentini *et at.* [20] used butylamine-grafted SWNT in a DGEBA epoxy resin with butylamine as the hardener. They reported an increase of the total heat of reaction, a higher final cure degree and a higher glass transition temperature of the functionalized SWNT-based composites compared to the unfilled epoxy. The surface groups reacted with the epoxy resin allowing these improvements.

4. Conclusions

In this study, the effect of unmodified MWNT on the cure kinetics and glass transition temperature of an epoxy resin was analyzed on the basis of the literature results. It was found that various authors reported an acceleration effect of CNT. The cure reaction was promoted in its early stage which may be due to the catalyst particles present in the CNT raw material. The effect of CNT on the T_g remains unclear. SWNT may lead to a decrease of T_g due to their bundling tendency. On the other hand, results reported for MWNT showed an increased or unchanged T_g of the composites. The use of solvent can lead to a decrease of T_g even after careful evaporation due to residual traces. The present status of the literature does not allow a clarification due to the lack of a study providing essential information such as purity (catalyst particles can affect cure reaction), glass transition temperature along with the corresponding cure degree (to isolate the true potential effect of CNT from curing variations).

Acknowledgements

Financial support from ARKEMA is appreciated.

References

[1] Puglia D., Valentini L., Armentano I., Kenny J. M.: Effects of single-walled carbon nanotube incorporation on the cure reaction of epoxy resin and its detection by Raman spectroscopy. Diamond and Related Materials, **12**, 827–832 (2003).
DOI: 10.1016/S0925-9635(02)00358-8

[2] Valentini L., Armentano I., Puglia D., Kenny J. M.: Dynamics of amine functionalized nanotubes/epoxy composites by dielectric relaxation spectroscopy. Carbon, **42**, 323–329 (2003).
DOI: 10.1016/j.carbon.2003.10.039

[3] Xie H., Liu B., Yuan Z., Shen J., Cheng R.: Cure kinetics of carbon nanotube/tetrafunctional epoxy nanocomposites by isothermal differential scanning calorimetry. Journal of Polymer Science Part B: Polymer Physics, **42**, 3701–3712 (2004).
DOI: 10.1002/polb.20220

[4] Xie H., Liu B., Sun Q., Yuan Z., Shen J., Cheng R.: Cure kinetic study of carbon nanofibers/epoxy composites by isothermal DSC. Journal of Applied Polymer Science, **96**, 329–335 (2005).
DOI: 10.1002/app.21415

[5] Tao K., Yang S., Grunlan J. C., Kim Y-S., Dang B., Deng Y., Thomas R. L., Wilson B. L., Wei X.: Effects of carbon nanotube fillers on the processes of epoxy resin-based composites. Journal of Applied Polymer Science, **102**, 5248–5254 (2006).
DOI: 10.1002/app.24773

[6] Wu J., Chung D. D. L.: Calorimetric study of the effect of carbon fillers on the curing of epoxy. Carbon, **42**, 3039–3042 (2004).
DOI: 10.1016/j.carbon.2004.07.010

[7] Bae J., Jang J., Yoon S-H.: Cure behavior of the liquid-crystalline epoxy/carbon nanotube system and the effect of surface treatment of carbon fillers on cure reaction. Macromolecular Chemistry and Physics, **203**, 2196–2204 (2002).

[8] Zhou Y., Pervin F., Lewis L., Jeelani S.: Experimental study on the thermal and mechanical properties of multi-walled carbon nanotube-reinforced epoxy. Materials Science and Engineering: A, **452–453**, 657–664 (2007).
DOI: 10.1016/j.msea.2006.11.066

[9] Ganguli S., Aglan H., Dean D.: Microstructural origin of strength and toughness of epoxy nanocomposites. Journal of Elastomers and Plastics, **37**, 19–35 (2005).
DOI: 10.1177/0095244305045927

[10] Ganguli S., Aglan H., Dennig P., Irvin G.: Effect of loading and surface modification of MWCNTs on the fracture behaviour of epoxy nanocomposites. Journal of Reinforced Plastics and Composites, **25**, 175–188 (2006).
DOI: 10.1177/0731684405056425

[11] Shen J., Huang W., Wu L., Hu L., Ye M.: Thermo-physical properties of epoxy nanocomposites reinforced with amino-functionalized multi-walled carbon nanotubes. Composites Part A: Applied Science and Manufacturing, **38**, 1331–1336 (2007).
DOI: 10.1016/j.compositesa.2006.10.012

[12] Tseng C-H., Wang C-C., Chen C-Y.: Functionalizing carbon nanotubes by plasma modification for the preparation of covalent-integrated epoxy composites. Chemistry of Materials, **19**, 308–315 (2007).
DOI: 10.1021/cm062277p

[13] Gojny F. H., Schulte K.: Functionalisation effect on the thermo-mechanical behaviour of multi-wall carbon nanotube/epoxy-composites. Composites Science and Technology, **64**, 2303–2308 (2004).
DOI: 10.1016/j.compscitech.2004.01.024

[14] Shen J., Huang W., Wu L., Hu Y., Ye M.: The reinforcement role of different amino-functionalized multi-walled carbon nanotubes in epoxy nanocomposites. Composites Science and Technology, **67**, 3041–3050 (2007).
DOI: 10.1016/j.compscitech.2007.04.025

[15] Hernández-Pérez A., Avilés F., May-Pat A., Valadez-González A., Herrera-Franco P. J., Bartolo-Pérez P.: Effective properties of multiwalled carbon nanotube/epoxy composites using two different tubes. Composites Science and Technology, **68**, 1422–1431 (2008).
DOI: 10.1016/j.compscitech.2007.11.001

[16] Fidelus J. D., Wiesel E., Gojny F. H., Schulte K., Wagner H.: Thermo-mechanical properties of randomly oriented carbon/epoxy nanocomposites. Composites Part A: Applied Science and Manufacturing, **36**, 1555–1561 (2005).
DOI: 10.1016/j.compositesa.2005.02.006

[17] Gong X., Liu J., Baskaran S., Voise R. D., Young J. S.: Surfactant-assisted processing of carbon nanotube/polymer composites. Chemistry of Materials, **12**, 1049–1052 (2000).
DOI: 10.1021/cm9906396

[18] Wang S., Liang Z., Liu T., Wang B., Zhang C.: Effective amino-functionalization of carbon nanotubes for reinforcing epoxy polymer composites. Nanotechnology, **17**, 1551–1557 (2006).
DOI: 10.1088/0957-4484/17/6/003

[19] Wang S., Liang Z., Gonnet P., Liao Y-H., Wang B., Zhang C.: Effect of nanotube functionalization on the coefficient of thermal expansion of nanocomposites. Advanced Functional Materials, **17**, 87–92 (2007).
DOI: 10.1002/adfm.200600760

[20] Valentini L., Puglia D., Carniato F., Boccaleri E., Marchese L., Kenny J. M.: Use of plasma fluorinated single-walled carbon nanotubes for the preparation of nanocomposites with epoxy matrix. Composites Science and Technology, **68**, 1008–1014 (2008).
DOI: 10.1016/j.compscitech.2007.07.011

[21] Moniruzzaman M., Du F., Romero N., Winey K. I.: Increased flexural modulus and strength in SWNT/epoxy composites by a new fabrication method. Polymer, **47**, 293–298 (2006).
DOI: 10.1016/j.polymer.2005.11.011

[22] Liao Y. H., Marietta-Tondin O., Liang Z., Zhang C., Wang B.: Investigation of the dispersion process of SWNTs/SC-15 epoxy resin nanocomposites. Materials Science and Engineering A, **385**, 175–181 (2004).
DOI: 10.1016/j.msea.2004.06.031

[23] Lau K-t., Lu M., Lam C-k., Cheung H-y., Sheng F-L., Li H-L.: Thermal and mechanical properties of single-walled carbon nanotube bundle-reinforced epoxy nanocomposites: The role of solvent for nanotube dispersion. Composites Science and Technology, **65**, 719–725 (2005).
DOI: 10.1016/j.compscitech.2004.10.005

[24] Allaoui A., El Bounia N., Courbaron A. C., Derail C.: Enhancement and characterization of carbon nanotubes dispersion in epoxy matrix for structural applications. in ‘Proceedings of International Symposium on Aircraft Materials ACMA 2008, Agadir, Morocco’ in press (2008).

[25] Allaoui A., Bai S., Cheng H. M., Bai J. B.: Mechanical and electrical properties of a MWNT/epoxy composite. Composites Science and Technology, **62**, 1993–1998 (2002).
DOI: 10.1016/S0266-3538(02)00129-X

[26] Allaoui A., Evesque P., Bai J. B.: Effect of aging on the reinforcement efficiency of carbon nanotubes in epoxy matrix. Journal of Materials Science, **43**, 5020–5022 (2008).
DOI: 10.1007/s10853-008-2728-5

[27] Miyagawa H., Rich M. J., Drzal L. T.: Thermo-physical properties of epoxy nanocomposites reinforced by carbon nanotubes and vapour grown carbon fibers. Thermochimica Acta, **442**, 67–73 (2006).
DOI: 10.1016/j.tca.2006.01.016

eXPRESS Polymer Letters Vol.3, No.9 (2009) 595–604
Available online at www.expresspolymlett.com
DOI: 10.3144/expresspolymlett.2009.74

A new route to prepare nanocomposites based on polyvinyl chloride and MgAl layered double hydroxide intercalated with laurylether phosphate

N. H. Huang[1,2*], *J. Q. Wang*[3]

[1]Key Laboratory of Green Processing and Functional Textiles of New Textile Materials, Ministry of Education, Wuhan University of Science and Engineering, Wuhan, 430073, P.R. China
[2]Department of Polymer Science and Engineering, Wuhan University of Science and Engineering, Wuhan, 430073, P.R. China
[3]National Laboratory of Flame Retardant Materials, Beijing Institute of Technology, Beijing, 100081, P.R. China

Received 10 May 2009; accepted in revised form 26 June 2009

Abstract. The MgAl layered double hydroxide (LDH) with laurylether phosphate was prepared using reconstruction method. Delamilation of the LDH with laurylether phosphate (LDH-PK) in tetrahydrofuran was characterized by AFM (atomic force microscopy), indicating that a large part of the LDH was delaminated into single, double and multi layers. The delaminated LDH-PK suspension was then used with polyvinyl chloride (PVC) to prepare a series of high-LDH-loading nanocomposites. Both the XRD (X-ray diffraction) patterns and TEM (transmission electron microscopy) photographs of the as-prepared PVC/LDH nanocomposites indicated that the LDH nanolayers dispersed uniformly in the PVC matrix. With differential scanning calorimetry (DSC) the glass transition temperatures of PVC phases in the PVC/LDH nanocomposites were measured and a slightly lower value than that of pristine PVC has been observed. Thermogravimetric analysis results show that the presence of LDH enhanced the dehydrochlorination temperature (T_{max1}), reduced the maximum degradation rate (R_{max1}) and the 5% weight loss temperature, and promoted the char formation of PVC. However, the thermal degradation temperature (T_{max2}) and thermal degradation rate (R_{max2}) of the dehydrochlorinated PVC were slightly affected by the presence of LDH. The apparent activation energies were calculated by the method of Flynn-Wall-Ozawa in nitrogen at four different heating rates, showing that the nanofiller increased the apparent activation energies by 10–26 kJ/mol when compared with pristine PVC, probably implying that the LDH nanolayers improve the stability of chlorine atom on the PVC chains.

Keywords: *nanocomposites, polyvinyl chloride, layered double hydroxide, thermal properties, exfoliation-restacking*

---

1. Introduction

In recent years polymer nanocomposites based on layered double hydroxides (LDHs) have attracted considerable attention because they can be considered to be reinforced by the nanofiller and follow the various unique properties such as enhanced mechanical properties, thermal stability, and reduced flammability [1–7]. LDHs are lamellar structured hydrotalcite-like compounds with anionic exchange properties. Their general chemical formula is $[M_x^{II}M_{1-x}^{III}(OH)_2]^{x+}[A_{x/m}^{m-}\cdot nH_2O]$, where M^{II}, M^{III}, and A^{m-} represent divalent metal cation (like Mg^{2+}, Zn^{2+}, Ni^{2+}, etc.), trivalent metal cation (like Al^{3+},Cr^{3+}, etc.), and the interlayer anion (like CO_3^{2-}, Cl^-, SO_4^{2-}, and various organic carboxylates, sulfates, sulfonates), respectively, where *n* is the number of associated water molecules [8]. The ability to exchange the interlayer anions intro-

---

[*]Corresponding author, e-mail: nhhuang1223@yahoo.com.cn

duces provides a opportunity via which known flame retardant anions, such as PO_4^{3-}, can be incorporated into the lamellar structure before adding the LDH to a polymer.

In general, polymer/LDH nanocomposites can be prepared via four major methods [9], i.e. *in situ* polymerization, direct intercalation, exfoliation restacking and coprecipitation. Amongst the methods, the exfoliation restacking method is especially suitable for the preparation of nanocomposites based on thermosensitive polymers such as poly(vinyl chloride). Wherein, the LDH was stepwise exfoliated into single, double and mutilayers in the proper solvents and afterwards transformed into a colloidal system and finally, the colloidal system was precipitated in the presence of the polymer. However, pristine LDHs is generally not liable to be exfoliated in solvent because of the high charge density on the layers. Recently, to modify the LDHs with organic anions has been found to be a successful strategy for exfoliation in solvent [10–12]. As reported by Adachi-Pagano *et al.* [11], the ZnAl-LDH modified with dodecyl sulfate may be a way efficiently delaminated in formamide. Later, Hibino and Jones [12] also reported that glycinate-containing MgAl-LDH was delaminated in formamide at room temperature. The laurylether phosphate (PK) was taken in the laboratory as a modifier to realize the preparation of laurylether phosphate intercalated LDH (LDH-PK), which was successfully exfoliated under the reflux in tetrahydrofuran solvent.

Poly(vinyl chloride) (PVC) is known as one of the widely used and low cost thermoplastics. Recently, Bao *et al.* [13] reported that partially intercalated and partially exfoliated PVC/MgAl-LDH nanocomposites were prepared by *in situ* suspension polymerization of vinyl chloride monomer in the presence of LDHs modified with dodecyl sulfate anions (LDH-DS). The fully exfoliated PVC/MgAl-LDH nanocomposites were prepared via a melt-compounding process by Chen [14], later, via solution intercalation [15, 16]. It is noted that special vessels are usually required and the toxic monomer is indispensable during these processing. The solution process may provide the most desirable conditions to prevent thermal and oxidative degradation during preparation [17]. Very few studies on the PVC/MgAl-LDH nanocomposites have been documented in literatures through novel exfoliation restacking route using laurylether phosphate intercalated LDH. In this regard we report the subject at low temperature. A preliminary study is on the exfoliation behavior of LDH-PK in tetrahydrofuran solvent using atomic force microscopy (AFM). Structure, thermal properties and thermal degradation kinetics of the PVC/LDH nanocomposites were followed in the next part by XRD, TEM, TG (thermogravimetry) and DSC.

2. Experimentals

2.1. Materials

PVC (density 1.36 g/cm^3, the number average molecular weight $7.8\cdot10^4$) was purchased from Hubei Yihua Chemical Industry Co. Ltd, China. $Mg(NO_3)_2\cdot6H_2O$, $Al(NO_3)_3\cdot9H_2O$, and urea was analytical grade purchased from Sinopharm Group Chemical Reagent Co. Ltd, China, and used without further purification. Aqueous solution of potassium laurylether phosphate (PK) (30 wt% in water) was purchased from Dandong Ankang Chemical Industry Co. Ltd, China.

2.2. Preparation of MgAl-LDH-CO_3

LDH-CO_3 was synthesized by urea hydrolysis method described by Costantino *et al.* [18]. An aqueous solution containing $Al(NO_3)_3$ and $Mg(NO_3)_2$ with the molar fraction $Al(NO_3)_3/(Al(NO_3)_3 + Mg(NO_3)_2)$ equal to 0.33 was prepared by dissolving $Al(NO_3)_3$ and $Mg(NO_3)_2$ in distilled water. To this solution solid urea was added until the molar fraction urea/$(Mg(NO_3)_2 + Al(NO_3)_3)$ reached 3.3. The clear solution was refluxed for 36 h. The white precipitate was then filtered, washed five times by doubly distilled water and dried in vacuum at 60°C till constant weight.

2.3. Preparation of the layered double hydroxide- laurylether phosphate (LDH-PK)

LDH-CO_3 was calcined in a muffle furnace at 450°C for about 6 h to convert it into metal oxide. The calcined product (CLDH) was dispersed in a 120 ml of aqueous solution containing 6 g of potassium laurylether phosphate (PK) and the dispersion was stirred by magnetic stirrer for 24 h at 25°C under flowing Ar. The regenerated PK intercalated

LDH (LDH-PK) was filtered out followed by drying in vacuum at 60°C.

2.4. Preparation of PVC/LDH nanocomposites

A schematic representation of the preparation of the PVC/LDH nanocomposite is shown in Figure 1. LDH-PK was firstly refluxed in 100 ml tetrahydrofuran for 24 h under flowing Ar with mechanical stirring. After treatment, the exfoliated LDH material was achieved by dispersing LDH-PK in tetrahydrofuran. A desired amount of PVC was dissolved in tetrahydrofuran solvent, and then the PVC/tetrahydrofuran solution was added to the LDH-PK suspension. After stirring for 3 h at 60°C under flowing Ar, the mixture was poured into 50 ml absolute ethanol for rapid precipitation in order to avoid aggregation of the LDH platelets. The precipitate was filtered and dried at 60°C under flowing Ar for 12 hours.

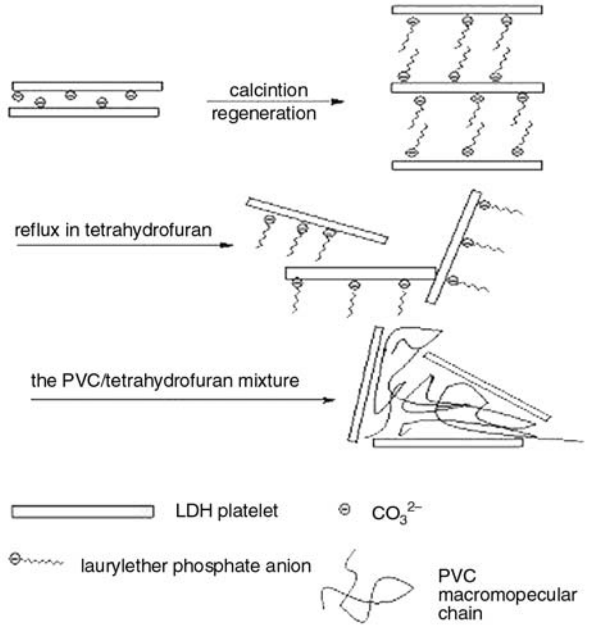

Figure1. Schematic representation of the preparation of the PVC/LDH nanocomposites

2.5. Characterization

2.5.1. Atomic Force Microscopy (AFM)

Atomic Force Microscopy (AFM) can be used to investigate the delamination behaviour of LDH in solvent and the thickness of the exfoliated nanosheets in the colloid dispersion [10]. AFM was performed using a Nanoscope E multimode AFM from digital instruments. The instrument was operated in tapping mode in air at room temperature. A Si tip with a diameter smaller than 10 nm (Mikronmasch) was used to achieve high resolution. Height and amplitude-mode images were recorded simultaneously with 512×512 pixel resolution and 1–2 Hz scan rate. Processing and analyses of the images were carried out using the off-line software Nanoscope. A concentration (0.1 g/l) of exfoliated LDH in tetrahydrofuran was used for AFM. One drop of the clear dispersion was dripped onto a freshly cleaved mica surface (1×2 cm^2). The sample was then conditioned at room temperature for 24 h and kept at 60°C for 48 h. Freshly cleaved mica has locally a very smooth surface with a an average roughness of *ca*. 0.1 nm.

2.5.2. X-ray diffraction analysis (XRD)

X-ray diffraction analysis (XRD) over $2\theta = 1.2$–65°, in steps of 0.02° was carried out using a Rigaku 2600 X-ray diffractometer with Cu-K_α radiation ($\lambda = 0.15418$ nm, monochromatization by primary graphite crystal) generated at 30 mA and 40 kV.

2.5.3. Fourier Transform Infrared (FTIR) spectroscopy

Fourier transform infrared (FTIR) spectra for samples were recorded over the wave number range 400–4000 cm^{-1} using Bruker Tensor 27 FTIR spectrometer.

2.5.4. Thermal analysis

Thermogravimetric analysis (TG) was performed on the NETZSCH thermal analyzer (TG 209 F1). Samples weighting about 5.0 mg were heated from room temperature to 700°C in a dynamic nitrogen atmosphere (50 ml/min). For kinetic analysis of the thermal degradation, TGA experiments of some samples were performed at four different heating rates, such as 5, 10, 20, 40°C/min. DSC data was measured by a NETZSCH DSC-204F1 at heating rate of 10°C/min with N_2 purging (50 ml/min).

2.5.5. Transmission electron microscopy (TEM)

The state of aggregation of the LDH particles in PVC matrix was investigated by TEM, which was carried out using transmission electron microscope with JEOL 2010 (HT) microscope. The conditions used during analysis were room temperature, 200 kV acceleration voltage and bright field illumination. The ultra thin sections of samples, which were embedded in an epoxy oligomer polymerized at 50°C for 48 h, were prepared by ultramicrotomy at –130°C using Reichert Ultracut S (Leica, Austria). The thickness of the section cut was in the range of 70–80 nm.

3. Results and discussion

3.1. Characterization of LDHs

The FTIR spectra of the LDH-CO_3, its calcined form (CLDH) and its regenerated form (LDH-PK) are shown in Figure 2. Figure 2a reveals the presence of interlayer carbonate ions (1361 cm^{-1}) and the associated water molecules appeared within the broad range of 3150–3600 cm^{-1} in LDH-CO_3, where the hydrogen bonding in the interlayer region between water molecules and the hydroxide sheet is evident from shoulder at 3050–3100 cm^{-1}. In Figure 2b, the loss of interlayer carbonate anions and water molecules results in the weakening of the corresponding peaks. The weakened broad peak around 3400 cm^{-1} is possibly attributed to some adsorbed water molecules on the surface of CLDH [5]. In Figure 2c the reapprearance of the O–H peak (stretching vibration peak) takes place with the disappearance of the shoulder existed in the original LDH. Other peaks can be easily assigned as follows: 2928 and 2853 cm^{-1} (aliphatic C–H stretch); 1225 cm^{-1} (the P=O bond); 1125, 1094 cm^{-1} (the P–O–C bond).

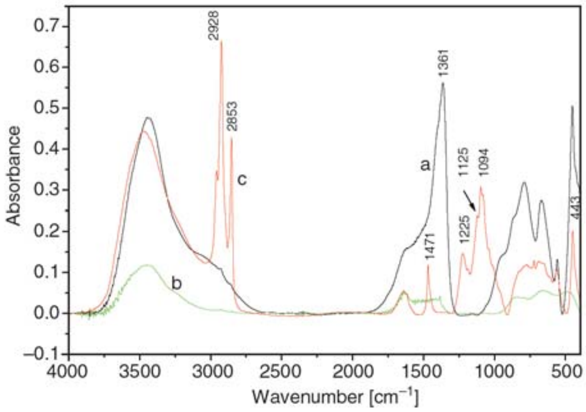

Figure 2. FTIR spectra of LDH-CO_3 (a), its calcined product (CLDH) (b) and LDH-PK (c)

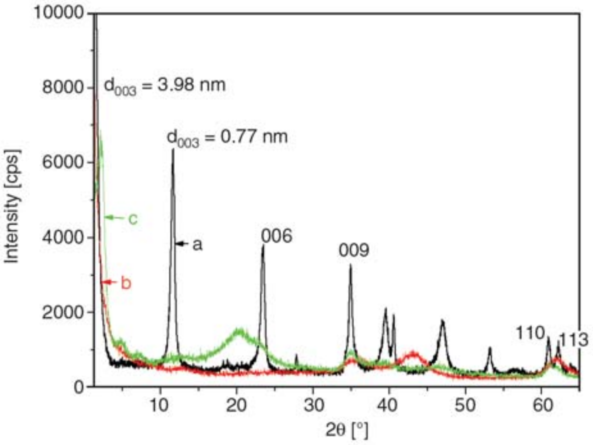

Figure 3. XRD spectra of LDH-CO_3 (a), its calcined product (CLDH) (b) and LDH-PK (c)

The sharp and distinct peaks appeared in the XRD pattern (Figure 3a) give an indication of the highly crystalline nature in the synthesized LDH-CO_3 and layered geometry. Close to the assignment and the value of 0.78 nm reported by Chibwe and Jones [19] a value of 0.77 nm ($2\theta = 11.4°$) of the basal peak (003) was measured. After calcination, CLDH loses all the peaks characteristic of layered structure as well as MgAl layer crystal structure, just as indicated in the Figure 3b. Again, Figure 3c also supported the subsequent recovery of the original structure by dispersing CLHD into an aqueous solution of laurylether phosphate. The XRD pattern of regenerated material (LDH-PK) (Figure 3c) shows a basal spacing of 3.98 nm ($2\theta = 2.14°$). The space between the Mg/Al nanolayers of the LDH-PK larger than that of pure LDH-CO_3 confirms an enlargement of interlayer distance from 0.77 to 3.98 nm. Based on FTIR and XRD results one could believe the intercalation of the laurylether phosphate into the LDHs. The increase of interlayer distance (Δd_L) in the LDH-PK, calculated from the d_{003} spacing and thickness of the inorganic layer (estimated to 0.48 nm), is approximately 3.5 nm. However, according to the individual dodecyl sulphate chain length (ca. 2 nm) [2], the individual laurylether phosphate chain length is close to 2 nm. This leads to the conclusion that the orientations of PK in the gallery of LDHs may be essentially inclined bilayer (see Figure 1).

3.2. AFM images of delaminated LDH-PK in tetrahydrofuran

A representative AFM images of delaminated LDH-PK deposited on a mica substrate can be shown in Figure 4. A thin layer of well dispersed nanoparticles lying parallel to the substrate surface is observed in Figure 4a, and the size and shape of individual particles are better visible. Figure 4b shows a cross section of individual particles along the marked green line. The particles are disk-like with diameters of typically 30–60 nm. Particles with different thicknesses of 0.7~5 nm are observed, which may correspond to single, double and multi hydrotalcite layers. Very small amount of particles with heights of up to 10 nm may tend to cause the aggregation of delaminated single or double nanosheets during volatilization of tetrahydrofuran solvent.

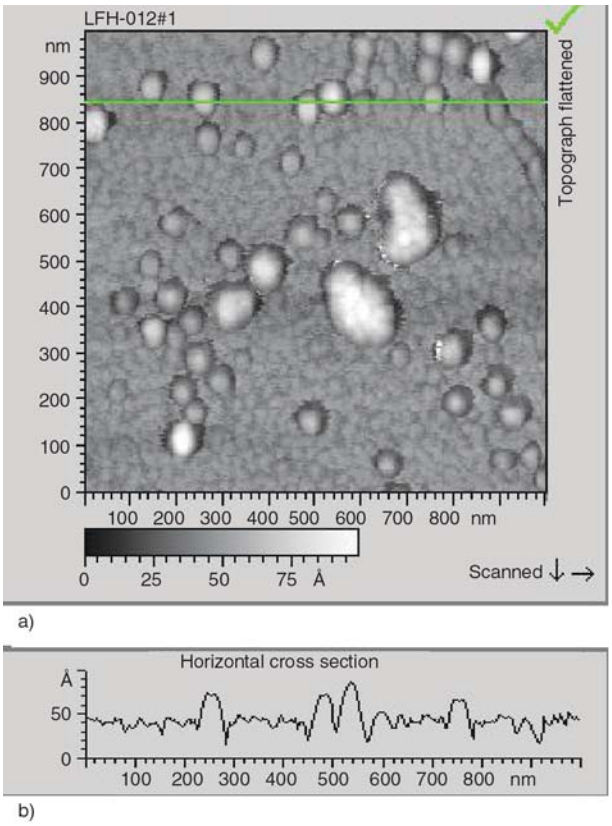

Figure 4. AFM images (tapping mode) of exfoliated LDH-PK in tetrahydrofuran (0.1 g/l) deposited on a mica substrate. Height image over a scanning area of 1000×1000 nm^2 (a); section profile along the marked green line, showing single, double and multi layers of exfoliated LDH (b).

3.3. XRD and TEM analysis of PVC/LDH nanocomposites

The X-ray diffraction (XRD) patterns of the LDH-PK and PVC/LDH composites are shown in Figure 5 within the range of $2\theta = 1.2–10°$. The changes in structure spread out before us through the study on the diffraction patterns with different loadings of LDH-PK. The basal spacing of the LDH-PK sample presented itself at 3.98 nm ($2\theta = 2.14°$). While at a loading of 50%, the diffraction peaks below $2\theta = 3°$ retained rather weaker (Figure 5f) and almost nothing left below 30% in Figures 5a to 5e, implying that the PVC/LDH nanocomposite with high loading of LDH can be obtained by exfoliated-restacking method.

Figure 6 shows the TEM images of PVC/LDH nanocomposite with 20 wt% LDH. The low magnification TEM image showed the LDHs to be well dispersed throughout the polymer. Higher magnification showed that the LDH are exfoliated to LDH nanolayers in the PVC matrix, but intercalated tactoids were also present.

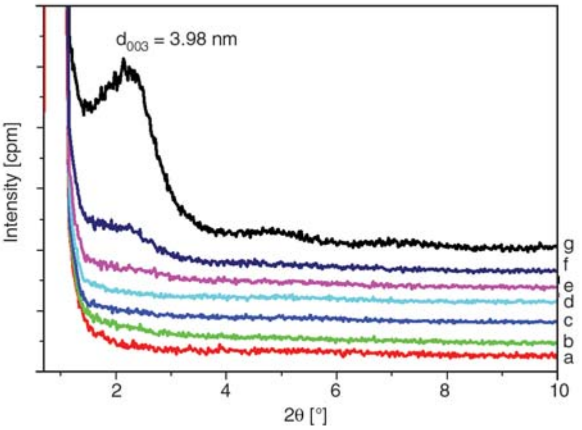

Figure 5. Variation of XRD patterns with the different loadings of LDH in the PVC/LDH nanocomposite samples in the range of 1.2 to 10° 2θ: (a) 5 wt%, (b) 10 wt%, (c)15 wt%, (d) 20 wt%, (e) 30 wt%, (f) 50 wt% , (g) 100 wt%

3.4. DSC analysis

Figure 7 shows DSC curves of pristine PVC and the PVC/LDH nanocomposites. The glass transition temperature (T_g) of the nanocomposites with 2 and 5% LDH are 84.9 and 84.6°C, respectively, slightly lower than that of pristine PVC (85.4°C) in agreement with the value in PVC/MMT nanocomposites [20] and PP/MMT nanocomposites [21].

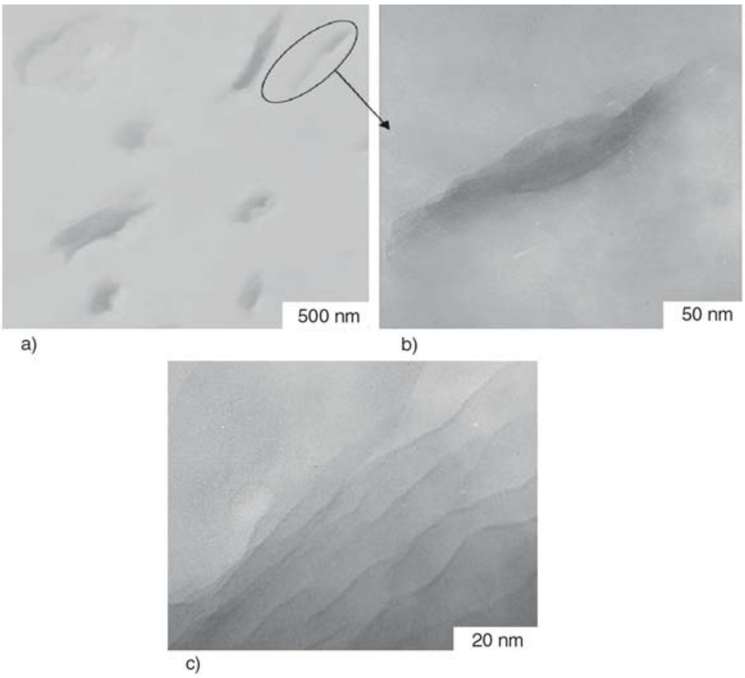

Figure 6. TEM micrographs of PVC/LDH nanocomposites with 20% loading of LDH

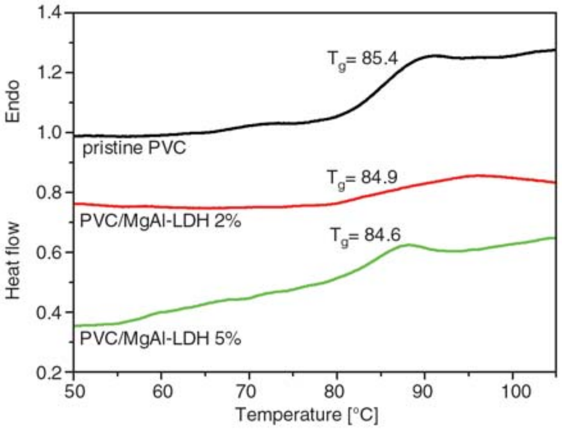

Figure 7. DSC curves of PVC and PVC/LDH nanocomposites with different loading of LDH

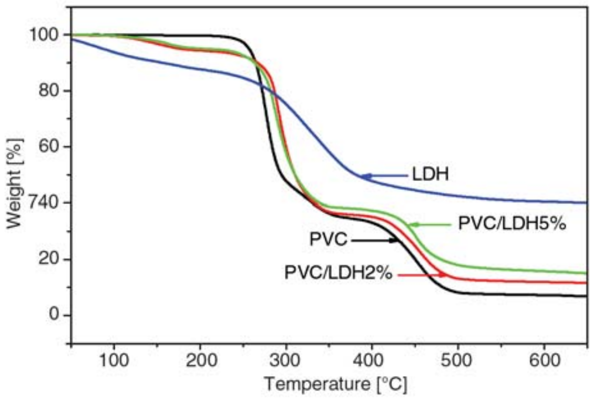

Figure 8. TGA curves of LDH, pristine PVC and its nanocomosites with 2 and 5% LDH in N_2 at heating rate of 10°C/min

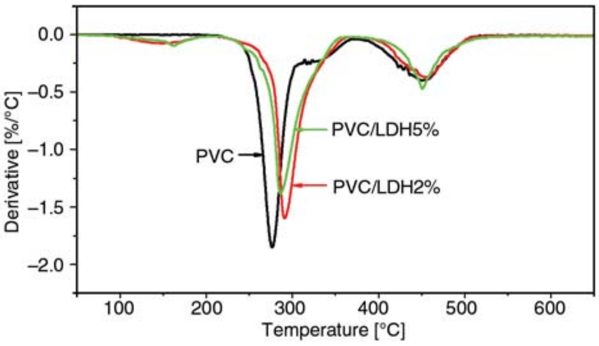

Figure 9. DTG curves of pristine PVC and its nanocomosites with 2 and 5% LDH in N_2 at heating rate of 10°C/min

Similarly, the LDH layers nano-dispersed in PVC matrix taking PVC macromolecules apart, rendering the interaction between macromolecular chains in nanocomposites weakened [20] and resulting in the decrease of the glass transition temperature of PVC phases in the PVC/LDH composite. In addition, it is possible that the PVC matrix was slightly plasticized by some of laurylether phosphate, and this resulted in the decrease of the T_g of PVC phases.

3.5. TG study

To exemplify the thermal behaviour the TG and DTG curves of pristine PVC and its nanocomposites were given in Figures 8 and 9. On heating the pristine PVC decomposes in the temperature range

Table 1. TGA data of pure PVC and PVC/LDH nanocomosites in N_2 at heating rate of 10°C/min

Sample	$T_{5\%}$ [°C]	T_{max1}/T_{max2} [°C]	R_{max1}/R_{max2} [°C]	Char or residue yield at 650°C [wt%]
LDH-PK				40.01
PVC	257.0	276.7/450.1	1.85/0.40	6.84
PVC/LDH 2%	204.4	290.0/452.0	1.60/0.38	11.61 (7.50*)
PVC/LDH 5%	206.0	286.2/450.7	1.38/ 0.42	15.05 (8.50*)

$T_{5\%}$ is the temperature for 5% weight loss; T_{max} is the temperature at which the rate of weight loss reaches a maxium.
*: theoretical values.

of 250–500°C [22]: the first stage is attributed to the elimination of hydrogen chloride molecules followed by the formation of the conjugated polyene sequences, while the second stage to the thermal cracking of the carbonaceous conjugated polyene sequences. As reported, the first step of weight loss for PVC/LDH (2 and 5%) nanocomposites occurs in the range of 120–250°C due to the evaporation of physically absorbed water in the intercalated layers and the loss of hydroxide on the LDH, similar to the case of polystyrene/ZnAl-LDH nanocomposites [3, 7], poly(vinyl alcohol)/MgAl-LDH nanocomposites [23] and poly(propylene carbonate)/MgAl-LDH nanocomposites [24]. The second step of weight loss occurs in the temperature range of 250–385°C due to the elimination of hydrogen chloride molecules in PVC chains. The thermal stability of both nanocomposites was obviously enhanced during this stage. The last stage is apparently relevant to the thermal cracking of the carbonaceous conjugated polyene sequences.

The 5% mass loss temperature ($T_{5\%}$), maximum mass loss temperature (T_{max1} and T_{max2}) and char (or residue) yield values at 650°C are summarized in Table 1. It can be seen that $T_{5\%}$ for two kinds of nanocomposites are decreased by about 52°C due to the evaporation of physically absorbed water in the intercalated layers and the loss of hydroxide on the LDH, whilst T_{max1} of PVC/LDH nanocomposites with 2 and 5% LDH are increased by 14 and 10°C, respectively. When LDH loading is 2%, the PVC nanocomposite shows the highest T_{max1} as 290°C. The maximum mass loss rate (R_{max1}) for PVC nanocomposites with 2 and 5% LDH are decreased from 1.85 to 1.60, 1.38%/°C, respectively. Judging from T_{max1} and R_{max1}, the PVC nanocomposites are more thermally stable than pristine PVC. It is probably because the LDH layers can improve the stability of chlorine atom on the PVC chains, and then retard the thermal degradation rate. But, both T_{max2} and R_{max2} of nanocomposites are close to that of pristine PVC, implying that LDH has little effect on the second thermal degradation stage of PVC. That is to say, LDH layers have little effect on the thermal cracking of the carbonaceous conjugated polyene.

It is noteworthy that char yield of PVC/LDH nanocomposites with 2 and 5% LDH at 650°C are significantly increased from 6.84 to 11.61, 15.05%, respectively. In Table 1, the values with * denote theoretical values obtained by calculation, i.e., char yield of PVC at 650°C×weight of PVC in PVC/LDH nanocomosites + residue yield of LDH-PK at 650°C×weight of LDH-PK in PVC/LDH nanocomposite. For example, for PVC/LDH nanocomposite with 2% LDH, 6.84%×98% + 40.01%×2% = 7.50%. As can be seen, these experimental values of char yield for nanocomposites are higher than the theoretical values, revealing that the LDH layers in PVC matrix enhance the formation of the char, i.e., the carbonization of the PVC, and stabilize the carbonanceous.

3.6. Thermal degradation activation energies of PVC and PVC/LDH nanocomposite

According to the Ozawa method [25], the apparent activation energies (E) were calculated from a linear fitting of $\ln\beta$ versus $1/T$ plot at different conversion degree (α) and at various heating rates (β), where the degree of decomposition $\alpha = (W_0–W)/(W_0–W_{550°C})$ (where W_0 is the initial weight, W is the actual weight and $W_{550°C}$ is the residual weight at 550°C). In Figure 10, for the PVC, the fitting lines are almost kept parallel to each other in the range of $\alpha < 0.6$, indicating the unique degradation mechanism, i.e. the chain stripping mechanism of PVC. But, the fitting lines for PVC are not kept parallel to each other in the range of $\alpha = 0.7$~0.9. This reveals that the degradation mechanism for PVC is complex, corresponding to the second thermal degradation stage of PVC. For the PVC/LDH nano-

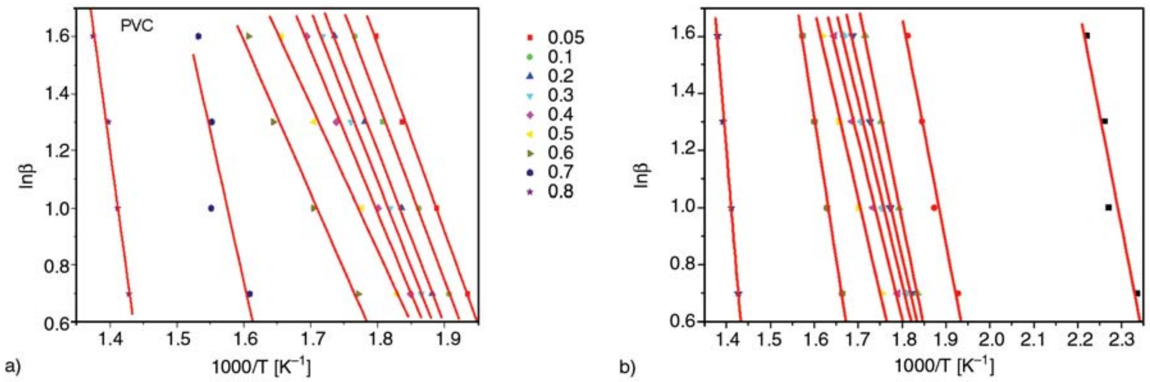

Figure 10. Plots of lnβ versus 1/*T* for PVC (a) and PVC/LDH (2%) nanocomposite (b) at various conversion degrees according to the Ozawa method

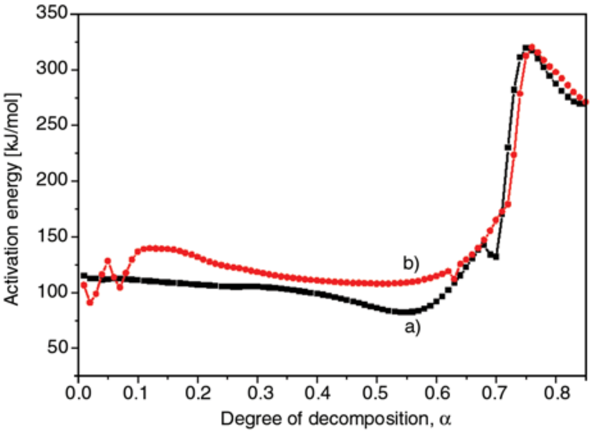

Figure 11. Plot of *E* versus α for the dynamic degradation of PVC (a) and PVC nanocomposite with 2% LDH (b)

composite, the fitting lines are also almost kept parallel to each other in the range of $0.1 < \alpha < 0.65$, not kept parallel to each other in the range of $\alpha = 0.7\sim0.9$ and $\alpha < 0.1$.

It can be seen in Figure 11 that the *E* versus α for PVC can be separated into two stages(namely $\alpha < 0.55$, and $\alpha > 0.75$) and is in agreement with DTG result (Figure 9). The *E* versus α for PVC is almost a constant in the range of $\alpha < 0.6$, being 90~110 kJ/mol, close to the value of 90~ 100 kJ/mol reported by Ma *et al.* [26] and Marcilla and Beltrain [27]. However, the *E* versus α for PVC/LDH nanocomposite with 2% LDH exhibits three stages (namely $\alpha < 0.1$, $0.1 < \alpha < 0.6$, and $\alpha > 0.75$). The *E* of the nanocomposite is complex in the range of $\alpha < 0.1$, which is attributed to the evaporation of physically absorbed water in the intercalated layers and maybe the loss of hydroxide on the LDH. The *E* versus α for the nanocomposite is almost a constant in the range of $\alpha = 0.1\sim0.6$, which corresponds to the dehydrochlorination of PVC, implying that the presence of LDH layers could not change the dehydrochlorination mechanism of PVC. In the range of $\alpha = 0.1\sim0.6$, the nanocomposite increases the activation energy by 10~26 kJ/mol, relative to pristine PVC. It may reveal that the presence of LDH layers improves the stability of chlorine atom on the PVC chains and represses the dehydrochlorination of PVC. However, the mechanism of thermal stability of LDH layers in the PVC matrix must further be studied in future.

Interestingly, in the range of $\alpha > 0.75$, the apparent activation energies of pristine PVC are close to that of the nanocomposite, indicating that the LDH layers have little influence on the thermal degradation stage of PVC at high temperature, i.e. the thermal cracking of PVC. This is in agreement with DTG results.

4. Conclusions

The PVC/MgAl-LDH nanocomposites were synthesized by novel exfoliation restacking method using laurylether phosphate modified LDH. Despite the ardent discussion of the nano-dispersion is put forward an argument in recent literatures. The conventional methods of characterizing dispersion, such as XRD and TEM were primarily invoked in the paper. Within the experimental error the nanodispersion of LDH layers in the PVC matrix has been verified by the observation of d_{003} XRD diffraction peak of LDH and the observation of TEM image. The glass transition temperature of PVC phases in the PVC/LDH nanocomposites are slightly lower than that of pristine PVC because of the weakened interaction between macromolecular chains in nanocomposites due to the interposition of LDH. The 5% weight loss temperature of the nanocomposites was also decreased owing to the evaporation of physically absorbed water in the intercalated layers and the loss of hydroxide on the LDH. Moreover, the dehydrochlorination temperature ($T_{\max1}$) and the char residue at 650°C of the nanocomposites were significantly increased in the presence of LDH. However, the thermal degradation temperature of the dehydrochlorinated PVC turned out to be little affected by the presence of LDH. The apparent activation energies calculated by the method of Flynn-Wall-Ozawa in nitrogen at four different heating rates show that the nanocomposite increased the apparent activation energies by 10–26 kJ/mol when compared with pristine PVC. Seemingly, the presence of LDH layers seems to improve the stability of the PVC chains through retarding the dehydrochlorination of PVC.

References

[1] Nyambo C., Wilkie C. A.: Layered double hydroxides intercalated with borate anions: Fire and thermal properties in ethylene vinyl acetate copolymer. Polymer Degradation and Stability, **94**, 506–512 (2009).
DOI: 10.1016/j.polymdegradstab.2009.02.001

[2] Lonkar S. P., Morlat-Therias S., Caperaa N., Leroux F., Gardette J. L., Singh R. P.: Preparation and nonisothermal crystallization behavior of polypropylene/layered double hydroxide nanocomposites. Polymer, **50**, 1505–1515 (2009).
DOI: 10.1016/j.polymer.2009.01.031

[3] Qiu L., Chen W., Qu B.: Exfoliation of layered double hydroxide in polystyrene by in-situ atom transfer radical polymerization using initiator-modified precursor. Colloid and Polymer Science, **283**, 1241–1245 (2005).
DOI: 10.1007/s00396-005-1305-6

[4] Hsueh H., Chen C-Y.: Preparation and properties of LDHs/polyimide nanocomposites. Polymer, **44**, 1151–1161 (2003).
DOI: 10.1016/S0032-3861(02)00887-X

[5] Costa F. R., Abdel-Goad M., Wagenknecht U., Heinrich G.: Nanocomposites based on polyethylene and Mg-Al layered double hydroxide. I. Synthesis and characterization. Polymer, **46**, 4447–4453 (2005).
DOI: 10.1016/j.polymer.2005.02.027

[6] Zammarano M., Franceschi M., Bellayer S., Gilman J. W., Meriani S.: Preparation and flame resistance properties of revolutionary self-extinguishing epoxy nanocomposites based on layered double hydroxides. Polymer, **46**, 9314–9328 (2005).
DOI: 10.1016/j.polymer.2005.07.050

[7] Qiu L., Chen W., Qu B.: Structural characterization and thermal properties of exfoliated polystyrene/ZnAl layered double hydroxide nanocomposites prepared via solution intercalation. Polymer Degradation and Stability, **87**, 433–440 (2005).
DOI: 10.1016/j.polymdegradstab.2004.09.009

[8] Ulibarri M. A., Pavlovic I., Barriga C., Hermosín M. C., Cornejo J.: Adsorption of anionic species on hydrotalcite-like compounds: Effect of interlayer anion and crystallinity. Applied Clay Science, **18**, 17–27 (2001).
DOI: 10.1016/S0169-1317(00)00026-0

[9] Leroux F., Besse J-P.: Polymer interleaved layered double hydroxide: A new emerging class of nanocomposites. Chemistry of Materials, **13**, 3507–3515 (2001).
DOI: 10.1021/cm0110268

[10] Wu Q., Sjastad A. O., Vistad Ø. B., Knudsen K. D., Roots J., Pedersen J. S., Norby P.: Characterization of exfoliated layered double hydroxide (LDH, Mg/Al=3) nanosheets at high concentrations in formamide. Journal of Materials Chemistry, **17**, 965–971 (2007).
DOI: 10.1039/b612389a

[11] Adachi-Pagano M., Forano C., Besse J-P.: Delamination of layered double hydroxides by use of surfactants. Chemical Communications, **1**, 91–92 (2000).
DOI: 10.1039/a908251d

[12] Hibino T., Jones W.: New approach to the delamination of layered double hydroxides. Journal of Materials Chemistry, **11**, 1321–1323 (2001).
DOI: 10.1039/b101135i

[13] Bao Y-Z., Huang Z-M., Weng Z-X.: Preparation and characterization of poly(vinyl chloride)/layered double hydroxides nanocomposite via *in situ* suspension polymerization. Journal of Applied Polymer Science, **102**, 1471–1477 (2006).
DOI: 10.1002/app.24317

[14] Chen G.: Preparation of a poly(vinyl chloride)/layered double hydroxide nanocomposite with a reduced heavy-metal thermal stabilizer. Journal of Applied Polymer Science, **106**, 817–820 (2007).
DOI: 10.1002/app.26514

[15] Liu J., Chen G., Yang J., Ma Y.: New facile preparation of a poly(vinyl chloride)/layered double hydroxide nanocomposite via solution intercalation. Chemistry Letters, **36**, 1454–1455 (2007).
DOI: 10.1246/cl.2007.1454

[16] Liu J., Chen G., Yang J.: Preparation and characterization of poly(vinyl chloride)/layered double hydroxide nanocomposites with enhanced thermal stability. Polymer, **49**, 3923–3927 (2008).
DOI: 10.1016/j.polymer.2008.07.014

[17] Wang D., Wilkie C. A.: Preparation of PVC-clay nanocomposites by solution blending. Journal of Vinyl and Additive Technology, **8**, 238–245 (2002).
DOI: 10.1002/vnl.10369

[18] Costantino U., Marmottini F., Rocchetti M., Vivani R.: New synthetic routes to hydrotalcite-like compounds-characterization and properties of the obtained materials. European Journal of Inorganic Chemistry, **1998**, 1439–1446 (1998).
DOI: 10.1002/(SICI)1099-0682(199810)1998:10<1439::AID-EJIC1439>3.0.CO;2-1

[19] Chibwe K., Jones W.: Intercalation of organic and inorganic anions into layered double hydroxides. Journal of the Chemical Society, Chemical Communications, **14**, 926–927 (1989).
DOI: 10.1039/C39890000926

[20] Yang D-Y., Liu Q-X., Xie X-L., Zeng F-D.: Structure and thermal properties of exfoliated PVC/layered silicate nanocomposites via in situ polymerization. Journal of Thermal Analysis and Calorimetry, **84**, 355–359 (2006).
DOI: 10.1007/s10973-005-6936-9

[21] Liu X., Wu Q.: PP/clay nanocomposites prepared by grafting-melt intercalation. Polymer, **42**, 10013–10019 (2001).
DOI: 10.1016/S0032-3861(01)00561-4

[22] Gong F., Feng M., Zhao C., Zhang S., Yang M.: Thermal properties of poly(vinyl chloride)/montmorillonite nanocomposites. Polymer Degradation and Stability, **84**, 289–294 (2004).
DOI: 10.1016/j.polymdegradstab.2003.11.003

[23] Li B., Hu Y., Zhang R., Chen Z., Fan W.: Preparation of the poly(vinyl alcohol)/layered double hydroxide nanocomposite. Materials Research Bulletin, **38**, 1567–1572 (2003).
DOI: 10.1016/S0025-5408(03)00203-4

[24] Du L., Qu B., Meng Y., Zhu Q.: Structural characterization and thermal and mechanical properties of poly(propylene carbonate)/MgAl-LDH exfoliation nanocomposite via solution intercalation. Composites Science and Technology, **66**, 913–918 (2006).
DOI: 10.1016/j.compscitech.2005.08.012

[25] Ozawa T.: A new method of analyzing thermogravimetric data. Bulletin of the Chemical Society of Japan, **38**, 1881–1886 (1965).
DOI: 10.1246/bcsj.38.1881

[26] Ma S., Lu J., Gao J.: Study of the low temperature pyrolysis of PVC. Energy and Fuels, **16**, 338–342 (2002).
DOI: 10.1021/ef0101053

[27] Marcilla A., Beltrain M.: Thermpgravimetric kinetic study of poly(vinyl chloride) pyrolysis. Polymer Degradation and Stability, **48**, 219–229 (1995).
DOI: 10.1016/0141-3910(95)00050-V